P 202
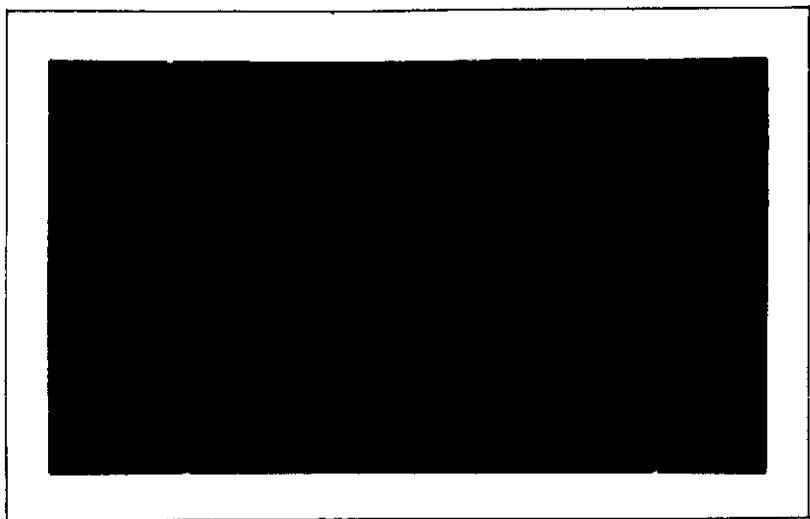
**METALS RESEARCH LABORATORY**

**CARNEGIE INSTITUTE OF TECHNOLOGY**

# Carnegie -Mellon University

**PITTSBURGH, PENNSYLVANIA**

An Investigation of the Plastic Fracture
of High Strength Steels

by

T. B. Cox and J. R. Low, Jr.

Department of Metallurgy and Materials Science
Carnegie-Mellon University
Pittsburgh, Pennsylvania 15213

NASA Technical Report No. 5

May 1973

(This report was submitted as a dissertation by T. B. Cox in partial ful-
fillment of the requirements for the degree of Doctor of Philosophy at the
Carnegie-Mellon University. )

Distribution of this document is unlimited

/

# TABLE OF CONTENTS

Table of Contents (Cont'd)

*iii*

# CHAPTER I

## INTRODUCTION

While man has utilized metals for many thousands of years and has refined and shaped them in quantity for several hundred,[1] the scientific study of the fracture process in metals has been going on for only about thirty years. Prompted by the large number of catastrophic failures of merchant ships made from welded steel plates which occurred during the winter of 1942-43, the U. S. Navy initiated a large scale investigation into the causes of these failures.[2] These studies were contined after the war under the aegis of the Ship Structure Committee and the National Academy of Sciences--National Research Council. It soon became apparent that the problem of brittle fracture in steels was not restricted to ships and had, in fact, existed for many years although there had been little attention paid to it, probably because each manufacturer or user merely wrote off a failure as an isolated case of bad luck.[3] Some of the more spectacular and costly failures of this early period in addition to the Liberty ships included the Duplessis Bridge in Quebec,[4] a cylindrical gas pressure vessel in Cleveland,[5] and numerous natural gas transmission pipelines.[6]

The low-strength ferritic steels involved in the above failure cases

1

exhibit a so-called ductile-to-brittle transition with decreasing tempera-
ture. Above the transition temperature range, these steels fail by plastic
fracture (dimpled rupture) in a ductile manner; while below the transition,
failure occurs in a very brittle manner by cleavage.[7] The transition
temperature range may be altered by changes in the chemical composition
or microstructure of a particular steel, or by varying the stress state or
by changes in the strain rate.[8] The failures outlined above were generally
attributed to the utilization of the various steels at temperatures below their
ductile-to-brittle transitions.

Recently, increased use has been made of high-strength alloy steels
for critical structural applications in naval vessels, aircraft, and aero-
space vehicles. Unlike the low-strength ferritic steels in which unstable,
brittle fracture occurs by cleavage, these high-strength alloys may frac-
ture catastrophically by highly localized, severe plastic deformation. In
most instances, the high-strength alloy steels do not exhibit distinct
ductile-to-brittle transitions (at least not within the temperature ranges of
normal application) and generally fail by plastic fracture, often referred
to as dimpled rupture, fibrous fracture, or ductile fracture. Under load-
ing conditions which impose high degrees of constraint on the high-strength
alloy, such as in thick sections or at the tips of crack-like flaws, fracture
may occur at drastically reduced levels of macroscopic plastic strain with
very little energy absorption, i.e., brittle fracture occurs.[8]

While cleavage fracture has been extensively studied and many of
the microstructural features which affect it have been determined,[8,10,11]

very little research has been done on the plastic fracture process in high-strength steels. It is the purpose of this investigation to study in detail the three generally recognized stages of plastic fracture in high-strength steels, namely, void initiation, void growth, and void coalescence. By understanding the various microstructural aspects of the plastic fracture process, it should be possible to suggest means of improving the resistance of the high-strength steels to fracture.

CHAPTER II

BRIEF REVIEW OF THE EXISTING LITERATURE ON
PLASTIC FRACTURE

A. Void Initiation

It is generally agreed that the initiation of voids at second-phase

particles within the metal matrix is the first step in the plastic fracture

process.[11] Although there have been some reports of microvoid initia-

tion in the absence of inclusions in very high-purity materials and single

crystals,[12,13,14] these observations are probably the result of failing

to magnify the structure enough, since Palmer, Smith, and Warda[15]

have demonstrated that voids may be formed at particles as small as 50Å

in internally oxidized copper-silicon alloys strained at low temperatures.

The controversy is undoubtedly of purely academic interest since any com-

mercially produced structural alloy (even a high-purity melt) contains a

large population of extraneous particles (inclusions) suitable for nucleat-

ing voids.

Tipper[16] was probably the first to suggest that the cup and cone

fracture in single-phase ductile metals originates at voids formed by the

drawing away of the matrix from non-metallic inclusions. The early work

of Puttick[17] demonstrated that in the case of both copper and iron,

4

microvoids were, in fact, initiated at non-metallic inclusions. An extensive study using copper alloys with various second-phase particles including metals, non-metals, and voids by Edelson and Baldwin[18] showed that the ductility of the aggregates increased as the volume fraction of any of the second-phase particles was reduced. The improvement in ductility was extremely rapid with reductions in second-phase volume fraction at and below about 0.01, a level approximately that found in commercial alloys.

The plastic fracture process in pearlitic steels containing 0.20 percent carbon has been shown by Clausing[19] to originate at several second-phase microfeatures including the boundaries between pearlite colonies and pro-eutectoid ferrite, cementite lamellae within the pearlite colonies and at the interfaces between non-metallic inclusions and the matrix. Apparently these nucleation sites are general for all pro-eutectoid pearlitic steels, as the same observations have been made by several investigators for carbon contents ranging from 0.10 to 0.40 percent.[20-22] The work of Burns and Pickering[21] and Rinebolt and Harris[23] indicates that increasing the amount of pearlite in these low alloy pearlitic steels results in an elevation of the ductile-to-brittle transition temperature and a lowering of the energy absorbed on the upper Charpy shelf. Other work has shown that for a given amount of pearlite, changing the sulfur content from 0.025 percent to 0.005 percent can cause a rise in the upper shelf energy by as much as 50 foot pounds while the ductile-to-brittle transition temperature remains unchanged.[24] Thus, by reducing the number of void nucleation sites in the mild steels, it is possible to improve their resistance to plastic

fracture.

When carbon steels are heat treated to produce a spheroidized carbide aggregate with a ferrite matrix, Liu and Gurland[25] have found that voids are formed during straining by either the separation of the carbide-matrix interface or, in the case of large carbides, by cracking of the particle itself. In very low carbon ferritic steels, McMahon and Cohen[26] have shown that cleavage fractures are initiated by the cracking of cementite particles lying in the ferrite boundaries. Olsen and Ansell[27] have recently shown that voids are formed by interface decohesion at thoria particles during room temperature straining of TD-nickel and Ruedl[28] found the same initiation sites in aluminum containing a dispersion of $Al_2O_3$.

Second-phase particles have also been demonstrated to be the nucleation sites for microvoids in the high-strength structural alloys. Tanaka, Pampillo, and Low[29] have shown that voids are formed by the cracking of large impurity particles in a high-strength aluminum alloy and direct evidence for void formation at smaller inclusions by interface decohesion in a large number of structural aluminum alloys has been provided by Broek.[30] Recently, Greenfield and Margolin[31] have demonstrated that voids are initiated at the $\alpha$ particle interfaces in high-strength, $\alpha$-$\beta$ titanium alloys.

Bucher, Powell, and Spretnak[32] investigated the tensile fracture of several high-strength steels and concluded that void initiation occurred by interface separation at non-metallic inclusions and at large carbide particles. A series of quenched and tempered alloy steels containing various

amounts of sulfur were investigated by Birkle, Wei, and Pellessier[33] who found voids to be initiated at sulfides and carbides. A dramatic correlation was found between sulfur content and the fracture toughness of the alloy steel studied. At any given strength level decreasing the sulfur content from 0.049 to 0.008 percent by weight increased the fracture toughness, $K_{Ic}$, by approximately 50 percent. Several other studies on a wide variety of quenched and tempered steels containing alloy carbides report that void nucleation can occur by separation of the interface between inclusions and the tempered martensite matrix and between alloy carbides and the matrix; these include both chromium carbide[34] and molybdenum carbide[35] interfaces. A fractographic study by Birkle et al.,[36] using several different grades of maraging steel has shown that voids are nucleated at non-metallic inclusions, including various nitrides, carbides, and sulfides, depending upon the exact alloy. In the overaged condition, the maraging steels may exhibit void initiation at the strengthening precipitates ($Ni_3Mo$), as recently shown by Roesch and Henry.[37]

As has been indicated above, void initiation occurs at second-phase particles either by decohesion of the particle-matrix interface or by fracture of the particle itself. That the voids are formed at second-phase particles undoubtedly stems from the stress concentrations set up within and around the inclusions during tensile straining. Analytical expressions for the elastic stress concentrations at the boundaries of and within inclusions of specific shapes have been determined by Goodier[38] and Edwards[39] with other solutions cataloged by Sternberg.[40] These treatments are all

restricted to the model of a single particle embedded in an infinite matrix with both materials assumed to be isotropic and elastic. The stress concentration within a particle is greatest for a perfectly rigid inclusion and reaches the highest values for elongated particles with their longest dimension lying parallel to the applied stress. The magnitude of stresses across the inclusion-matrix interface depends upon the shape of the inclusion, its orientation, and the difference between the elastic moduli of the matrix and the inclusion. During tensile loading, the elastic strain energy stored at an inclusion may be reduced by localized plastic flow or by fracture. Unfortunately, the more interesting and practical problem of either elastic or plastic inclusions in a plastic matrix has not been solved as yet.

According to Gurland and Plateau[41] and others,[42, 43] the initiation of voids is generally preceded by plastic flow of the matrix in the regions of high stress concentration at the inclusions. The exact location of the void formation depends upon the relative values of the specific surface energies of the inclusions and the matrix and the stress concentration factor within the inclusion or at the interface. It has been suggested by Backofen[44] that pre-existing voids may exist at inclusions even in the absence of applied stress. This situation may arise if the bond between the particle and matrix is weak and the coefficients of thermal expansion of the matrix and the inclusion are vastly different. Under these circumstances, it could be possible for the particle and matrix to separate during heating or cooling. Ashby[45, 46] has developed a dislocation model of plastic deformation around inclusions which demonstrates that tensile

stresses will be set up at the poles of inclusions contained within shear bands which can account for void formation by particle-matrix decohesion. While Ashby's model requires that dislocations must bypass the second-phase particles and leave dislocation loops around the particles, the calculations of Stroh[47-49] require only that the dislocations be blocked by some obstacle in order to set up normal stresses of a great enough magnitude to cause void formation.

## B.  Void Growth

Although several metallographic investigations have been made of void growth,[12,15,17,31,50] few systematic or quantitative observations have been carried out, making it impossible to satisfactorily check the various proposed models of void growth.  It was first suggested by Pines[51] and later by Cottrell[52] that the process of void growth would occur by a form of internal necking between nucleation sites by which the matrix material recedes away from the microvoid surfaces, much like the growing neck in a smooth, round tensile specimen.  Thomason[53] attempted to treat this possibility analytically for the two-dimensional case, resulting in reasonable agreement with the data of Edelson and Baldwin.[18] A qualitative model for hole growth by the motion of dislocations has been proposed by McLean[54] and simply involves the passing of dislocations out of the free surfaces of the voids with  the resultant void enlargement.

Several attempts have been made to empirically fit expressions for void growth to observed experimental results,[41,55] but little insight to actual processes involved in void growth has resulted from these efforts.

Similarly, attempts have been made to describe the void growth process by continuum mechanics. The analyses of McClintock[56-58] and Rice and Tracey[59] for the stress states existing around inclusions, holes, and at the tips of cracks indicate that the rate of void growth increases with increasing strain for both strain-hardening and non-strain-hardening materials, and that the existence of a state of triaxial tension (higher hydrostatic tension) should accelerate the rate of void growth. The data of Floreen and Hayden[50] of void sizes as a function of strain in a 300-grade maraging steel agree reasonably well with those predicted by McClintock, while the data collected by Greenfield and Margolin[31] in a titanium alloy do not appear to agree with the continuum models.

C. Void Coalescence

In a recent review of plastic fracture by Rosenfield,[60] it was asserted that the most critical and yet least understood aspect of the plastic fracture process is void coalescence. That little experimental work has been carried out on void coalescence is not surprising, for as shown by Bluhm and Morrissey,[61] using a very hard tensile machine, the initiation and growth of voids in various materials are gradual processes while void coalescence occurs very rapidly and catastrophically. Several mechanisms of void coalescence have been suggested in the literature including:

a) Necking down of the matrix between voids until the final ligament has no cross-sectional area,[52]

b) some combination of secondary void formation along regions of intense shear between primary voids,[12, 62]

c) the initiation and propagation of cracks in the regions of stress concentration around voids, [17]

d) the catastrophic normal rupture of the material between voids once the voids have reached some critical size analogous to the critical crack size of fracture mechanics treatments. [63]

As yet, no satisfactory quantitative treatment has appeared to describe the void coalescence process. Probably the best and most practicable method of studying void coalescence is after the fracture has occurred, as demonstrated by the careful fractographic studies of Crussard, et al. [64-67] Beachem[68] has demonstrated that for many metals there are three general modes of void coalescence. Depending upon the local stress state in the material between neighboring voids, they will coalesce by normal rupture, shear rupture, or tearing.

D. Maraging Steels vs Quenched and Tempered Steels

It is generally observed and repeatedly reported[69-71] that the maraging steels exhibit much higher fracture toughness values, i.e., are much more resistant to plastic fracture, than quenched and tempered steels when compared at a given strength level. The reasons for the superior toughness of the maraging steels are not clear, although much conjecture has been advanced on this subject. The suggestion has been offered that the extremely low carbon contents in the maraging steels avoid the deleterious effects of carbide precipitation at the martensite lath boundaries, [72] a precipitation which is next to impossible to prevent by normal quenching procedures even in quenched and tempered steels of very low carbon

content.[73, 74] Another reason advanced for the superior toughness of the maraging steels is that the fine, uniform distribution of intermetallic compounds in their structure is not as detrimental to toughness at high-strength levels as the fine carbide particles in alloy steels,[75, 76] although it is not made clear exactly why this is so. It has also been argued that the nickel-molybdenum compound which is the strengthening precipitate in many of the maraging grades is actually metastable and during the aging process is partially redissolved in the matrix to give a structure more effective in preventing void formation.[70] Unfortunately, while there have been many suggestions as to why the maraging steels are indeed tougher than quenched and tempered grades, there have been no definitive studies reported.

Floreen and Speich[77] were among the first to address themselves to the question of the high toughness of the maraging steels by studying a series of high purity quaternary iron -- 18 per cent nickel -- 8 percent cobalt alloys with the addition of various fourth elements to form strengthening precipitates. They found that the precipitation of $Ni_3Mo$ yielded far greater toughness than any of the other nickel compounds taken singly (those with Al, Be, Nb, Mn, Si, and Ti). It was observed that the nickel-molybdenum intermetallic precipitated in a fine, general dispersion throughout the martensitic structure, while the other compounds tended to prefer sites at the prior austenite grain boundaries. It was demonstrated that the presence of the cobalt produced a finer dispersion of precipitates in the molybdenum containing alloys, but that changing the level of cobalt in the

other alloys did not affect the precipitate dispersion. They found that the addition of molybdenum to a quaternary alloy containing titanium resulted in improved toughness and elimination of nickel-titanium compound precipitation at the prior austenite grain boundaries. The fracture path changed from intergranular to transgranular with the molybdenum addition. It has since been demonstrated that cobalt reduces the solubility of molybdenum at the aging temperature, causing widespread precipitation in the matrix.[78, 79] Unfortunately, Floreen and Speich[77] did not define the void nucleating particles for the plastic fracture process in their alloys.

Commercially prepared maraging steels contain inclusions generally identified as blocky particles of titanium carbo-nitride.[80, 81] In addition, some thin platelets and small particles of titanium carbide, nitride, and sulfide and zirconium and aluminum nitride have been observed at prior austenite grain boundaries and found on extraction fractographs of some maraging alloys.[36, 81, 82] In the tough condition where fractures are by dimpled rupture, the dimples have been associated with the titanium carbo-nitride particles while decreased thoughness and intergranular embrittlement and fracture have been observed in alloys containing the various grain boundary precipitates.

Apparently, the only investigation to date of the relationship between the strengthening precipitates and fracture surfaces in commercial maraging steels is that due to Roesch and Henry.[37] By changing the composition of an 18 percent nickel alloy and varying the heat treatments, they were able to change the distribution of particles in the martensitic matrix and correlate

the structures with the fracture surfaces. For an alloy of 18% nickel, 9% cobalt, 5% molybdenum, and 0.5% titanium in the as-quenched condition, the dimples on the fracture surface were large and were associated with relatively large inclusions (titanium carbo-nitrides). On aging (up to the point of maximum hardening), the fracture surface appearance remained the same, although in the microstructure a very fine, acicular precipitate ($Ni_3Mo$) was observed which seemed to have a definite crystallographic orientation with respect to the matrix and was generally associated with dislocations. During overaging, a gradual refinement occurred in the size of dimples observed on the fracture surfaces as the precipitates began to grow and coalesce. These observations led the authors to postulate that dimples can be initiated only by particles of some critical size or larger (in the range of 200Å for this alloy). They argued that during aging the small precipitates formed and grew. As long as their size remained below the critical value, no voids could be initiated by the strengthening particles, and the fracture surface would have the same appearance as after quenching. This critical size did not correspond to that at which coherency between precipitate and matrix was lost, but rather the critical size was much larger than that at the loss of coherency. For progressively longer aging times, some particles would have grown large enough to begin nucleating voids, until eventually at long aging times, all precipitates would be large enough to initiate voids and substantial refinement of the dimples on the fracture surface would occur. They reported that for the overaged condition, a high density of very small dimples was observed

on the fracture surface and that their average dimension corresponded roughly to a cell structure based on the number of precipitates and the interparticle spacing.

The only study of quenched and tempered steels comparable to that of Roesch and Henry,[37] although not as comprehensive, was reported by Baker, Lauta, and Wei[83] and carried out using AISI 4340. These authors followed the precipitation process and reported fracture paths and toughness values as the alloy was tempered at various temperatures. In the as-quenched condition, the martensite in the 4340 steel contained many micro-twins, the boundaries of which were populated with needles of epsilon carbide. Tempering the structure at low temperatures (below 600°F) resulted in further precipitation of epsilon carbide at twin boundaries and also in the development of a continuous network of epsilon carbide at the martensite platelet boundaries. These microstructural conditions resulted in a constant low level of toughness for all low tempering temperatures with the fracture paths tending to follow a succession of almost straight paths along suitably oriented boundary carbides. Unfortunately, no fractographic observations were made and all information on the fracture process was obtained from fracture surface profiles. By tempering above 600°F, cementite precipitated along the martensite boundaries. While the martensite retained its platelike morphology, the randomly tangled and high density of dislocations in the as-quenched and lower temperature tempered structures showed signs of recovery at these higher tempering temperatures. At tempering temperatures above 800°F, the cementite began to spheroidize and the

dislocation structure recovered more noticeably. Concurrently, the tough-
ness increased and the fracture path showed little tendency to follow any
distinct microstructural feature.

Due to the limited nature of the studies to date, it is not possible
to deduce the reasons for the advantage in toughness the maraging steels
exhibit over the quenched and tempered steels.

E. Hydrostatic Stress (Stress Triaxiality)

In his review of plastic fracture, Rosenfield[60] asserted that the
effects of second-phase particles and hydrostatic pressure were paramount
in determining plastic fracture behavior beside which all other metallurgical
variables (including temperature) are second order. It is common know-
ledge that the ductile-to-brittle transition temperature in mild steels is
raised when a material contains a notch or flaw, thus producing a state of
triaxial tension in the root region, and that the transition temperature con-
tinues to rise with increasing notch acuity.[84] Generally, the energy level
of the upper Charpy shelf also drops as notches are made more severe.
The classic experiments of Bridgman[85] demonstrated that increased duc-
tility can be achieved in metals by reducing the level of hydrostatic tension
on a specimen. By the application of large compressive hydrostatic pres-
sures, Bridgman was able to increase fracture stresses by as much as two
and one-half times while at the same time improving the reduction in area
by 70 percent. Coffin and Rogers,[86] using density measurements, showed
that by subjecting metals undergoing a sheet drawing operation to high
applied compressive hydrostatic pressures, it was possible to retard damage

due to internal void formation and realize greater section reductions while avoiding fracture. Another demonstration of the effect of stress triaxiality was reported by Marshall and Shaw.[87] They interrupted tensile tests of cylindrical specimens once a neck had formed and machined the specimen so that the neck was removed and the shape returned to a cylinder. Using this technique, they were able to remove the triaxial stress state and realize substantial improvements in reduction of area to fracture. Mukherjee, et al.[88] showed that by increasing the acuity of notches in round tensile specimens of structural aluminum alloys and steels, the reduction in area to fracture was reduced dramatically.

Although these studies have all demonstrated that increased ductility can be achieved by reducing the triaxial nature of tensile stress systems, it is not known exactly in which stages of the plastic fracture process the fracture resistance is degraded as the hydrostatic tension increases. The continuum mechanics treatments of McClintock[56-58] and Rice and Tracy[59] predict that increased hydrostatic tension will result in increased rates of void growth. Greenfield and Margolin offer conflicting reports as to the effect of hydrostatic tension on plastic fracture in high-strength titanium alloys. In their early work,[89] they report that void initiation is independent of hydrostatic stress and that void growth is enhanced by it. Later published work indicates void nucleation aided by tensile triaxiality and void growth unaffected.[31] Based on very limited observations in iron-cobalt alloys, Chin[90] concludes that stress triaxiality has no effect on void initiation. The situation with regard to the role of triaxiality in plastic

fracture mechanisms is obviously rather unsettled.

# CHAPTER III

## OUTLINE OF EXPERIMENTAL APPROACH

The objectives of this investigation are to describe the mechanisms by which several common high-strength steels fracture plastically. It is hoped that through a better understanding of the fracture process, it will be possible to suggest means of improving the resistance of these alloys to fracture. Specifically, the investigation will define the relative importance of each of the three stages of plastic fracture, namely, void initiation, void growth, and void coalescence. The exact details of the experimental procedures will be included at the appropriate places in the following text; but to make clear the direction of the study, an outline of the experimental approach is presented here.

The study involves the investigation of the plastic fracture of two families of high-strength steels, a quenched and tempered grade and a maraging grade, to provide comparison between the two most widely used types. In order that the study of the two grades be carried out at comparable strength levels, the particular alloys chosen for the investigation were AISI 4340 and 18 Ni, 200 grade maraging steel, both heat-treated to a yield strength of approximately 200 ksi. Since most high-strength steel

structural applications are for plate materials, the steels were processed as plate. To permit determination of the reasons for the improved toughness generally observed in plates produced with low levels of residual elements, both types of steel used in the investigation were studied using material from a commercial purity and a high-purity melt.

Initially, the tensile properties, toughness levels, and microstructures of the alloys were determined. The fracture surface characteristics of the alloys were studied extensively using electron transmission microscopy of replicas taken from the fractures produced in tensile and fracture toughness tests. In order to study the progression of the fracture process, a series of smooth, round tensile bars of each alloy was uniaxially deformed to various levels of strain short of fracture. At each level of strain, the tensile specimens were sectioned longitudinally and examined to determine the extent of void nucleation, sizes of voids present, and the degree of void association (coalescence). These metallographic observations were made using optical light microscopy supplemented by replica and transmission electron microscopy as dictated by the experimental findings. Furthermore, this procedure permitted determination of the exact mechanism of void nucleation--particle cracking or interface decohesion--as well as defining exactly which second-phase particles nucleate voids in these particular alloys.

Certain elementary techniques of quantitative metallography were applied to the tensile neck sections for the study of the void nucleation and growth stages of the fracture process. Comparison of the behavior of the

quenched and tempered AISI 4340 alloys and the 18 Ni, 200 grade maraging alloys disclosed the reason for the observed enhanced toughness of the maraging grades. To study the effects of triaxial tension on the plastic fracture process in these alloys, a series of mildly notched or pre-necked round tensile specimens of each alloy was subjected to the same procedure of straining and sectioning applied to the smooth tensile bars. This procedure permitted determination of the manner in which higher triaxial stress states degrade the fracture resistance of these alloys.

CHAPTER IV

MATERIALS

**A.** Chemical Composition and Processing History

The commercial purity alloys were both made in regular mill

production heats while both high-purity alloys were made in specially

melted laboratory heats. The commercial grade AISI 4340 was produced

using an electric furnace process and was provided as one-inch-thick

plate, straight-away rolled. The commercial 18 Ni, 200 grade maraging

steel was provided as four-inch-thick plate, hot-pressed and straight-

away rolled from a consumable electrode, vacuum remelted ingot. Both

the high-purity 18 Ni maraging steel and the high-purity AISI 4340 steel

were made from 300 pound vacuum induction melted heats of specially

selected charges. The ingots were subsequently cross-rolled (approxi-

mately one-to-one ratio) to one-inch-thick plates.

The chemical analyses of the four alloys used in the investigation

are presented in Table 1. The major differences to be noted are the sub-

stantial reductions in impurity levels when going from the commercial

melts to the high-purity melts, specifically P, S, $N_2$, and $O_2$ in the AISI

4340 and these same impurities in the 18 Ni, 200 grade maraging steel

together with C which is considered an impurity in the maraging steels.

22

TABLE I

Composition of High Strength Steels

(Weight Percent)

| | Commercial AISI 4340 | High Purity AISI 4340 | Commercial 18 Ni | High Purity 18 Ni |
|---|---|---|---|---|
| C | 0.43 ± 0.01 | 0.38 ± 0.01 | 0.021 ± 0.004 | 0.002 ± 0.002 |
| Mn | 0.78 ± 0.02 | 0.71 ± 0.02 | 0.04 ± 0.001 | <0.02 ± 0.01 |
| P | 0.010 ± 0.001 | 0.001 ± 0.001 | 0.003 ± 0.001 | 0.002 ± 0.001 |
| S | 0.013 ± 0.001 | 0.004 ± 0.001 | 0.008 ± 0.001 | 0.004 ± 0.001 |
| Si | 0.27 ± 0.02 | 0.29 ± 0.02 | 0.04 ± 0.01 | <0.03 ± 0.02 |
| Ni | 1.73 ± 0.02 | 1.81 ± 0.02 | 18.3 ± 0.1 | 18.1 ± 0.1 |
| Cr | 0.76 ± 0.02 | 0.80 ± 0.02 | <0.04 ± 0.02 | 0.05 ± 0.02 |
| Mo | 0.25 ± 0.01 | 0.25 ± 0.01 | 4.23 ± 0.05 | 4.16 ± 0.05 |
| Al(total) | 0.049 ± 0.003 | 0.023 ± 0.002 | 0.080 ± 0.002 | 0.062 ± 0.002 |
| Co | --- | 0.010 ± 0.01 | 7.85 ± 0.1 | 8.03 ± 0.1 |
| Ti | --- | < 0.005 ± 0.002 | 0.19 ± 0.01 | 0.23 ± 0.01 |
| $N_2$ | 0.008 ± 0.001 | 0.003 ± 0.001 | 0.005 ± 0.001 | 0.004 ± 0.001 |
| $O_2$ | 50 ± 10 ppm | 23 ± 3 ppm | 30 ± 10 ppm | 23 ± 3 ppm |
| Fe | Balance | Balance | Balance | Balance |

The carbon levels of the two AISI 4340 alloys differ by 0.05 weight percent. In addition, the amount of Al is lower in both high-purity melts as compared with the commercial melts and in the 18 Ni, 200 grade maraging alloy, high-purity melting results in reduction of Mn and Si levels.

## B. Heat Treatment and Mechanical Properties

Since it was desired to investigate the fracture behavior of these alloys at approximately the same strength level, they were given heat treatments designed to produce yield strengths close to 200 ksi. Both AISI 4340 alloys were austenitized at 843°C (1550°F) for one hour and oil quenched. Due to the differences in carbon contents, the tempering treatments were different with the commercial AISI 4340 being tempered at 435°C (815°F) for one hour and air cooled while the high-purity alloy was tempered at 427°C (800°F) for one hour and air cooled. The specially produced high purity 18 Ni, 200 grade maraging steel was solution annealed at 843°C (1550°F) for one hour and water quenched, then aged for three hours at 454°C (850°F) and air cooled. The commercial grade 18 Ni steel was solution annealed at 899°C (1650°F) for two and one-half hours and air cooled, followed by aging at 446°C (835°F) for six hours and air cooled. The differences in heat treatments for the maraging steels were necessitated by the large difference in plate thicknesses, i.e., one versus four inches.

The mechanical properties resulting from these heat treatments are given in Table II. The tensile data were determined using standard geometry, smooth, round tensile specimens and a testing procedure in

TABLE II

Room Temperature Mechanical Properties of High Strength Steels

(all values represent means of duplicate tests)

| | Commercial AISI 4340 | High Purity AISI 4340 | Commercial 18 Ni | High Purity 18 Ni |
|---|---|---|---|---|
| Yield Strength 0.2% Offset (ksi) | 204.8 | 204.6 | 193.5 | 189.9 |
| Ultimate Tensile Strength (ksi) | 221.6 | 218.0 | 197.7 | 198.5 |
| True Strain to Fracture | 0.287 | 0.515 | 0.747 | 1.005 |
| Fracture Toughness $K_{Ic}$ (ksi$\sqrt{\text{in}}$) | 67.9 | 97.2 | 113.0 | 149.1* |

* $K_Q$, invalid test due to undersized specimens. $K_{Ic}$ believed to be substantially higher, ~ 180 ksi$\sqrt{\text{in}}$.

accordance with ASTM Standard E8-61 T[91] on tension testing of metallic

materials. The fracture toughness testing was all performed at NASA

Lewis Research Center, Cleveland, Ohio. The value of $K_{Ic}$ for the com-

mercial purity 18 Ni, 200 grade maraging steel was obtained by interpola-

tion of the data of Fisher and Repko[92] who used material from the same

plate as used in this investigation for 3.9 inch thick bend specimens. The

other $K_{Ic}$ values were determined by Dr. W. F. Brown and Mr. M. H.

Jones using compact tension specimens. All fracture toughness tests were

performed in accordance with ASTM Standard E399-70T.[93] The fracture

toughness specimens were tested in the W R orientation (notched through

the plate thickness with the direction of crack propagation in the primary

rolling direction). The tensile bars were taken in the same orientation

of the maximum normal stress, i.e., lying in the plane of the plate and

perpendicular to the primary rolling direction.

Reference to Table II reveals that the yield strengths of the alloys

are in the general range of 200 ksi. Care was taken to match yield

strengths within a given alloy system, although the general level of yield

strength is about 15 ksi higher in the AISI 4340 alloys than in the maraging

steels. This difference was the result of several factors. The yield

strength of approximately 190 ksi realized for the high-purity 18 Ni 200

grade maraging steel represents the maximum strength attainable in this

particular heat. It was decided not to temper the AISI 4340 to this same

strength level since past experience indicated that it would be impossible

to get a valid $K_{Ic}$ measurement in the one-inch-thick high-purity plate of

AISI 4340 at this low strength. The values of true strain-to-fracture in Table II indicate that the ductility of these alloys is substantially improved by high-purity melting and that the general level of ductility is higher for the maraging steels than for the quenched and tempered AISI 4340 alloys. The same observations may be made for the fracture toughness values. The level of fracture toughness is greater in the maraging steels than in the AISI 4340 steels even when considering the difference in yield strength. Within a given alloy system, reduction of the impurity levels improves the fracture toughness.

## C. Tensile Flow Characteristics

The procedure outlined in the previous chapter for studying the progression of plastic fracture by straining and sectioning tensile specimens was implemented using 1/4-inch-diameter smooth round tensile specimens and 3/10-inch-diameter mildly notched round tensile specimens with 50 percent of the cross sectional area removed at the notch. The dimensions and geometries of these two specimen types are given in Figure 1 together with their orientation in the plate materials. The particular geometry of pre-necked specimen was chosen based on the previous work of Sachs, et al.[94-98] in order to assure fracture initiation in the center of the specimen as observed in smooth, round tensile specimens. This condition was desirable in order to facilitate comparison of the results from the smooth and notched specimen sectioning experiments.

Using one smooth and one notched tensile specimen of each alloy, the true stress-true strain curve for each alloy and specimen shape was
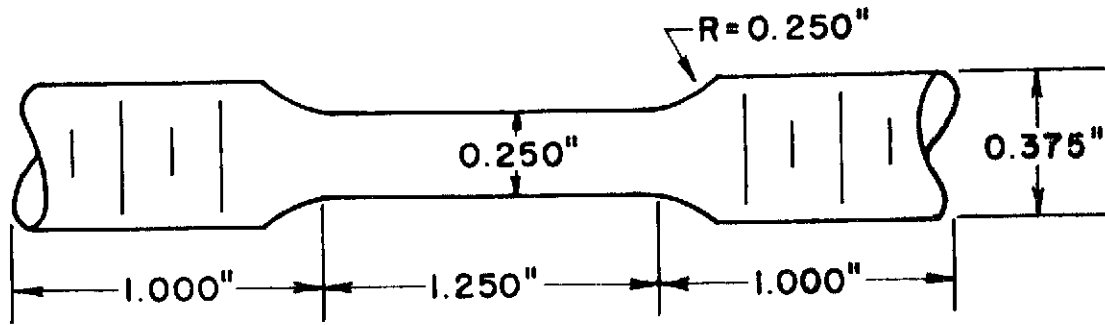
a) SMOOTH ROUND TENSILE SPECIMEN

b) NOTCHED ROUND TENSILE SPECIMEN
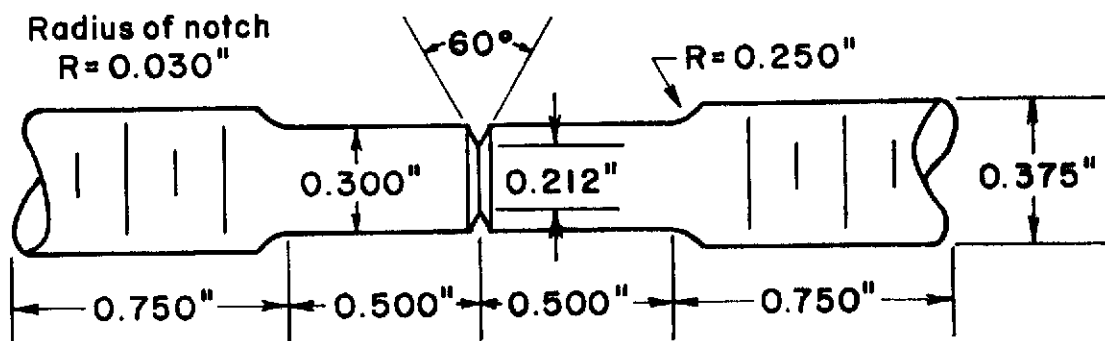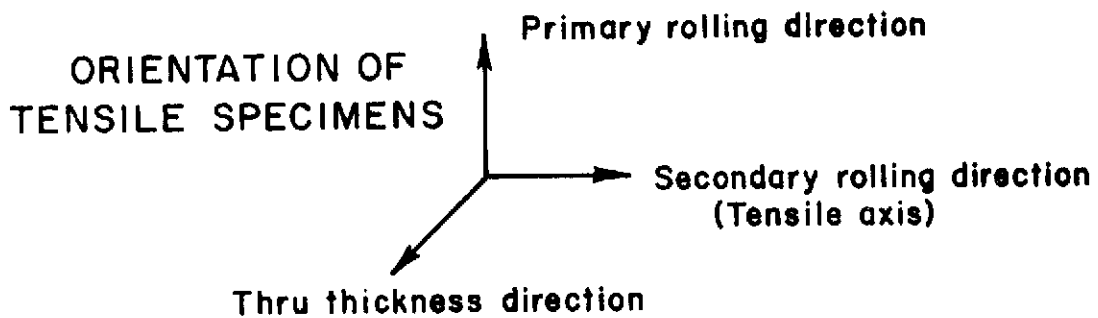
ORIENTATION OF
TENSILE SPECIMENS

Figure 1   Geometries and Orientation of Tensile Specimens.

determined. The strain was monitored periodically by measuring the specimen diameter using a point micrometer while the tensile load was still applied. By recording the diameter and applied load on the specimen periodically during a test, it was possible to generate the stress-strain curves for each alloy. To assure that the specimens of each alloy and geometry used in the sectioning study were from the same population, the applied stress and strain for each interrupted test specimen was compared with the true stress-true strain curves generated using only single test specimens. The true stress-true strain curves for the four alloys (both smooth specimens and notched specimens) are presented in Figures 2-5. The solid curves represent the stress-strain relationship determined using single specimens loaded to fracture (the solid data points), while the open data points represent the stress and strain conditions of interrupted tests which were subsequently sectioned for metallographic examination. As can be seen in the figures, the data from the interrupted test specimens fall on the same stress-strain curve for a given alloy and specimen geometry, thus assuring that the void initiation and growth data collected later are for alloys with the same flow properties.

Also included in Figures 2-5 are the uniaxial flow curves for the four materials as determined using the Bridgman correction for necking. [99] Bridgman's analysis of the stresses in the neck of a tensile specimen show that the axial stress on the plane of minumum diameter varies from a maximum at the center to a minimum at the specimen surface and is given by:
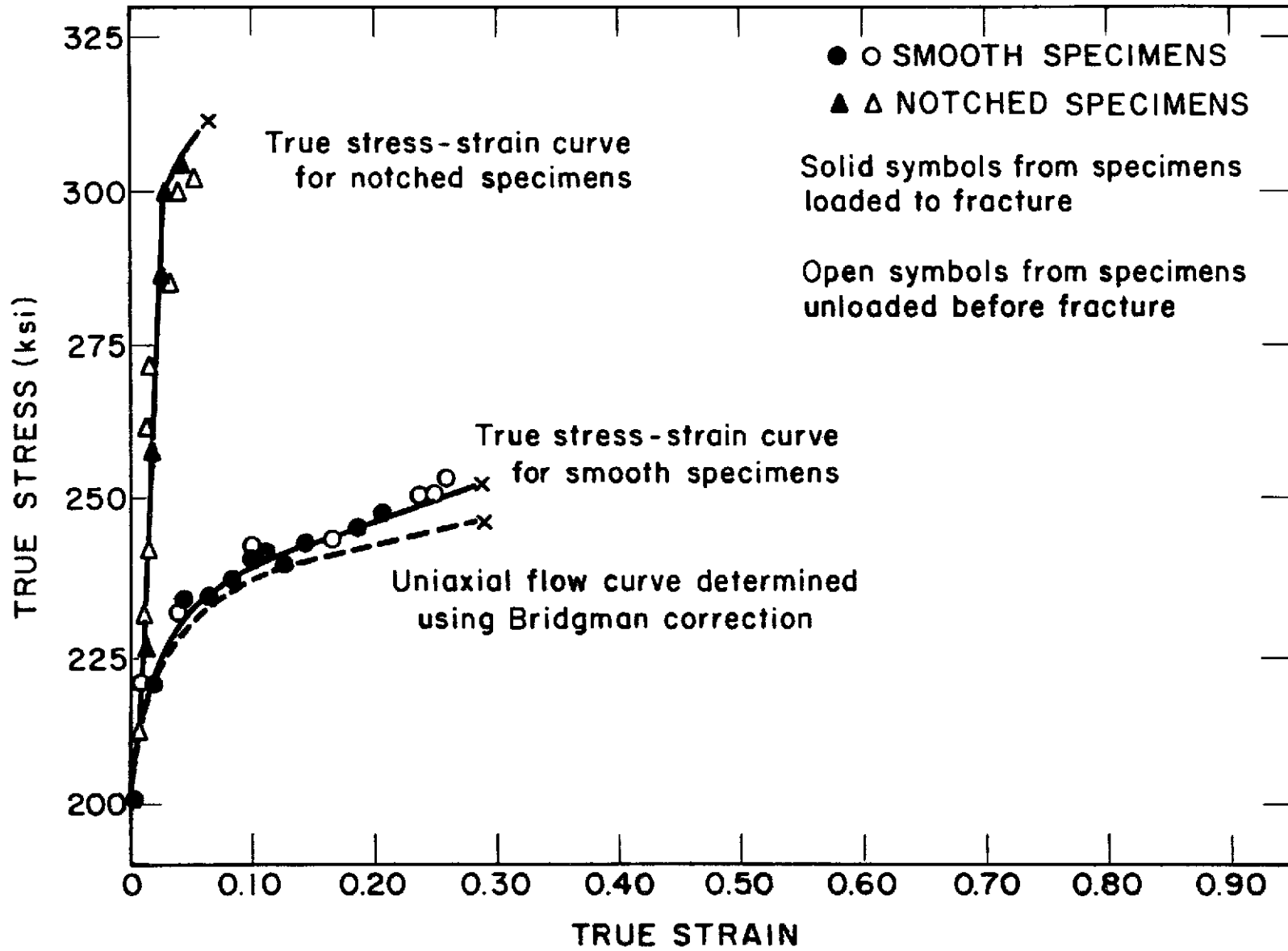
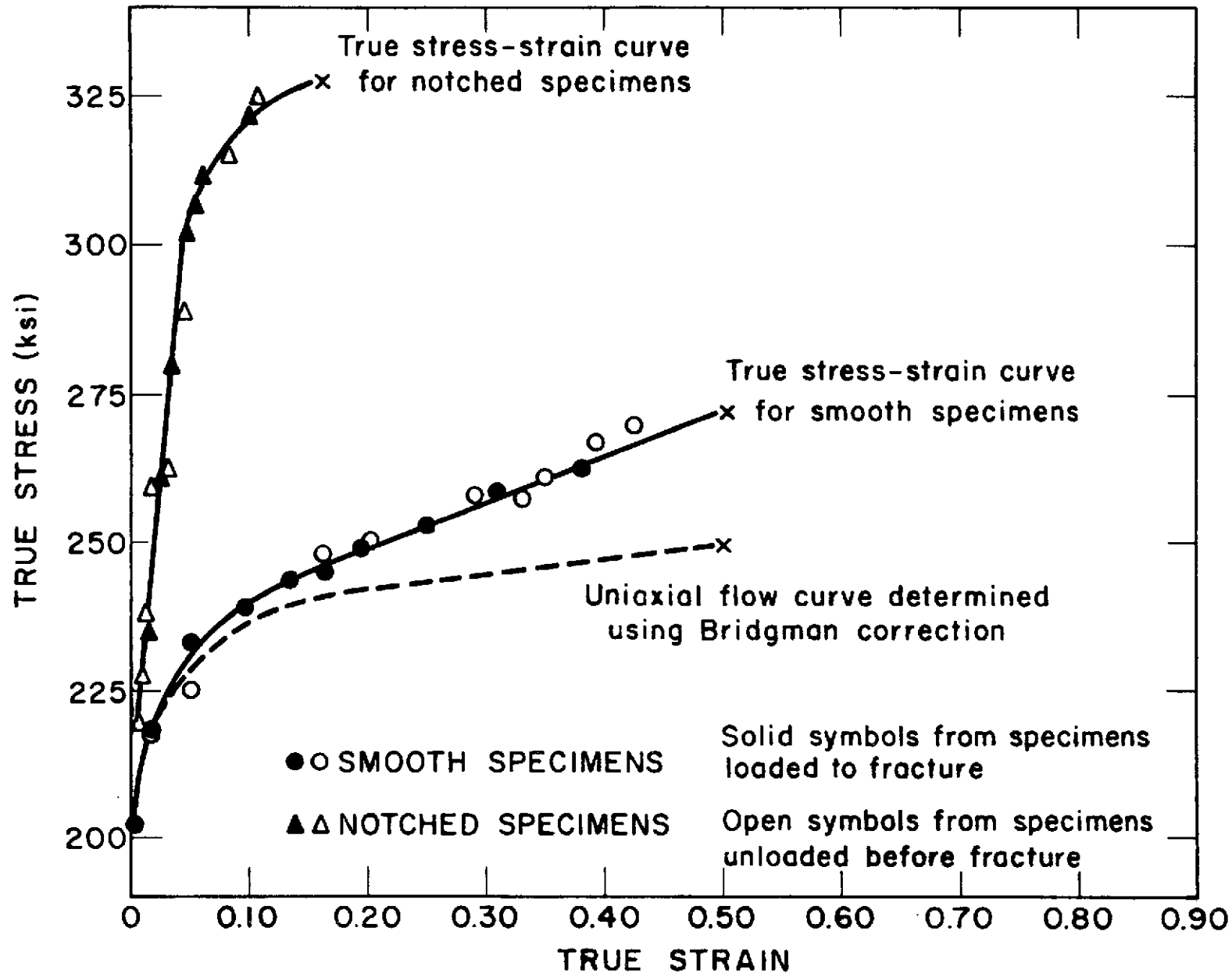Figure 2  Tensile Curves for Commercial Purity AISI 4340 Steel.

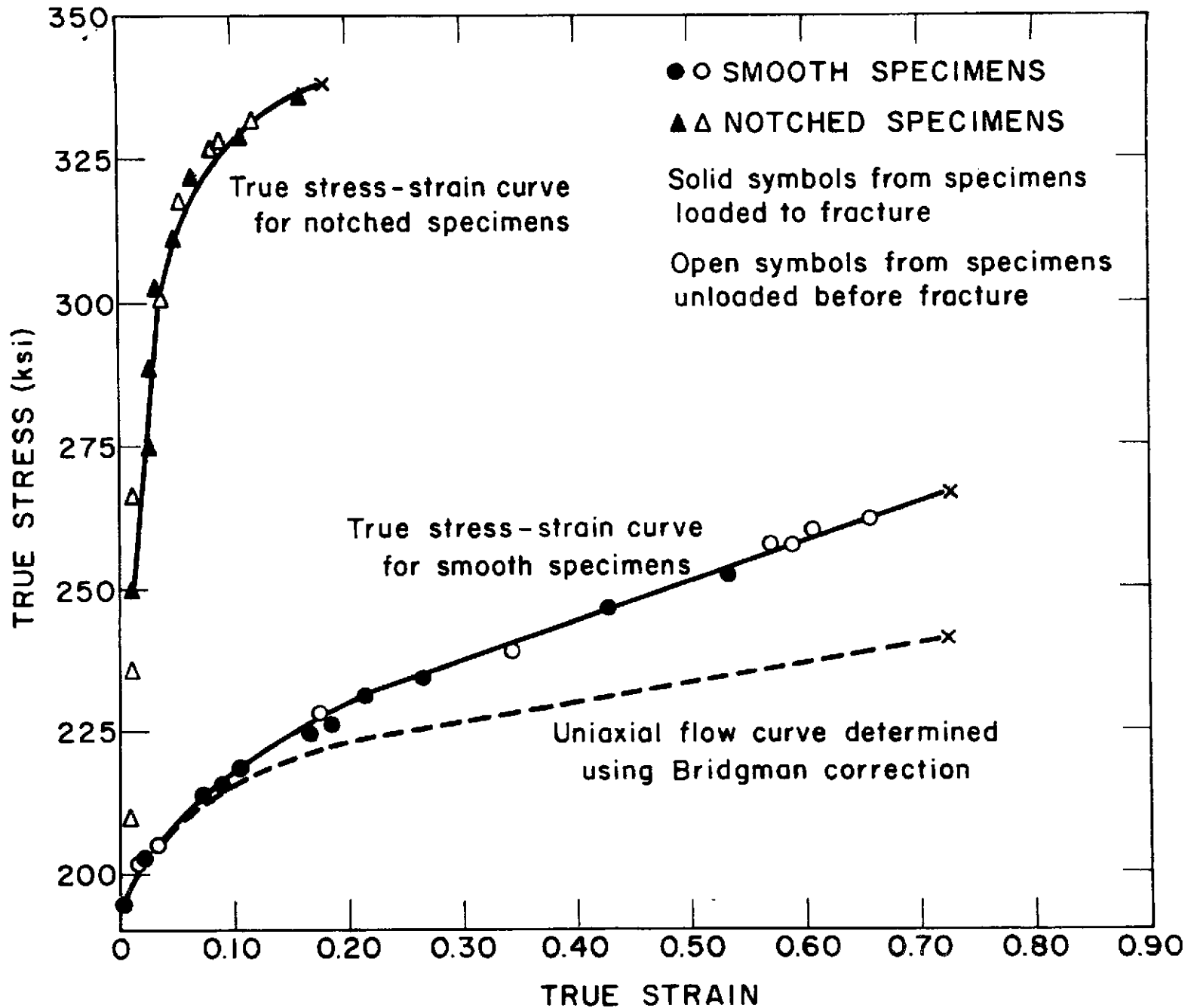Figure 3  Tensile Curves for High-Purity AISI 4340 Steel.

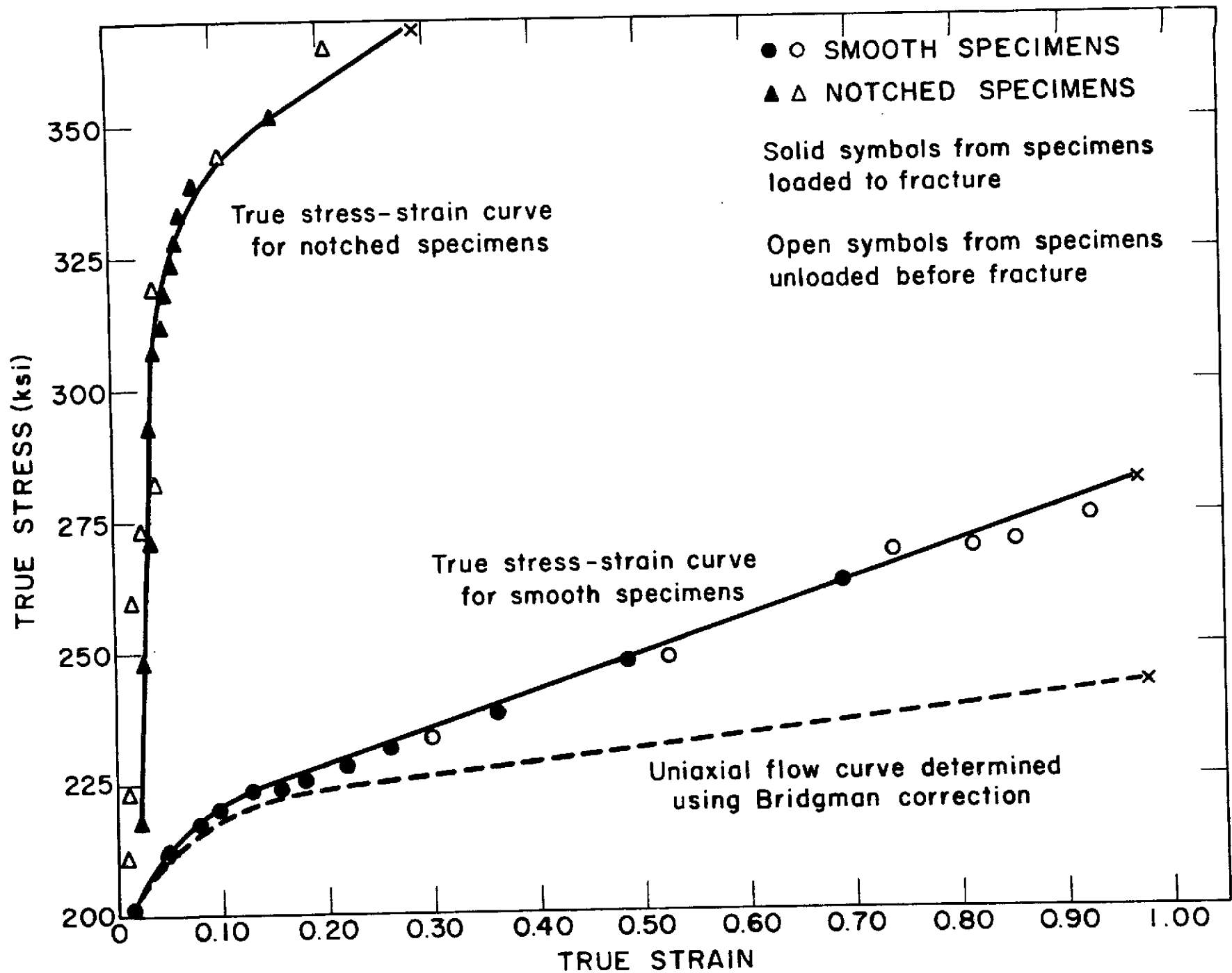Figure 4  Tensile Curves for Commercial Purity 18 Ni Maraging Steel.

Figure 5  Tensile Curves for High-Purity 18 Ni Maraging Steel.

$$\sigma_z = F + F \ln \frac{a^2 + 2aR - r^2}{2aR} \qquad [IV-1]$$

where   $F \equiv$ uniaxial flow stress
 $a \equiv$ specimen radius at neck
 $R \equiv$ radius of curvature of the neck profile

the two non-axial principal stresses are equal in magnitude and also vary

across the minimum section as follows:

$$\sigma_r = \sigma_\theta = F \ln \frac{a^2 + 2aR - r^2}{2aR} \, . \qquad [IV-2]$$

This treatment results in the following relationship between the flow stress

and the average applied tensile stress:

$$\text{Average Tension} = \frac{\text{Load}}{\pi a^2} = F \left(1 + 2 \frac{R}{a}\right) \ln \left(1 + \frac{1}{2} \frac{a}{R}\right) . \qquad [IV-3]$$

It should be noted that the uniaxial flow stress (F) from the Bridgman

analysis is equal to the difference between the maximum and minimum

principal stresses and thus is twice the maximum resolved shear stress.

All references to flow stress which follow below should be interpreted as

the uniaxial flow stress, F, i. e., twice the maximum resolved shear stress.

Furthermore, since the stress state in the tensile specimens can be de-

fined by the applied uniaxial flow stress plus a superimposed hydrostatic

tension equal to the lateral principal stress, these lateral stresses repre-

sent the level of the triaxial stress state within the neck. Thus the value

of the lateral stresses ($\sigma_r$ and $\sigma_\theta$) will be used below to define the level

of triaxiality of the stress system in the tensile specimens.

The flow curves in Figures 2-5 were determined using the data from the

smooth, round tensile specimens. The loads and cross-sectional radii, (a),

in the necks were recorded as described above, while the radii of curvature of the neck profiles, (R), were determined by geometric construction using enlargements of photographs of the neck regions. While there have been a few studies purporting to demonstrate that the Bridgman analysis is not correct,[87, 100] it is felt to be quite adquate for the accuracy involved in normal measurements of stress and strain using commercial testing equipment[101] as in the current study.

As mentioned above, the geometry of the notched tensile specimens was chosen so as to assure fracture initiation in the centers of the specimens. Another factor which would facilitate more meaningful comparison of the metallographic data from sections of the smooth and notched specimens would be for the stress states in the two specimen geometries to be similar. Sachs, et al.[94-98] and Luhahn[102] suggest that for mildly notched specimens (as used here), the Bridgman analysis should be applicable. The later work of Clausing[103] claims to show that the Bridgman treatment does not hold for notched tensile specimens and presents some evidence that the strain is not constant across the neck as required in the Bridgman analysis. The experimental method to determine the strain at various positions in the neck used by Clausing is quite questionable. (He used banding in steel specimens as fiducial markings to measure radial displacements. The maximum deviation of his readings from those required for uniform strain were of the order of the band widths. There were also problems with alignment and linearity of the bands.) Thus, we would conclude that there is little evidence to refute the validity of the

Bridgman analysis for midly notched specimens (those specimens for which fracture begins in the center of the specimen). In an attempt to clarify this point, the Bridgman correction for necking was applied to the data from the notched tensile specimens. Using the sectioned specimens from the interrupted series of notched straining experiments, the radii of curvature of the neck profiles (notch profiles) were determined geometrically on enlargements of photographs. These data, together with the radii of the strained cross-sectional areas in the notched necks were then combined with the flow stress curves determined from the smooth specimens using the Bridgman relationship [IV-3] to produce points on the true average stress-true strain curve. Representative results are presented in Figure 6 for the two high purity alloys. The solid curves are those which were determined experimentally (as in Figures 3 and 5) and the solid data points are those determined from the neck radii and the Bridgman analysis. As is seen in Figure 6, the Bridgman analysis predicts the average stress-strain curves quite well, which indicates that the stress state in the neck of a tensile specimen as determined by Bridgman and set down in equations [IV-1] and [IV-2] applies reasonably well to the mildly notched specimens used in this investigation.

## D.  Microstructures

Typical microstructures of the four alloys in the heat-treated condition are presented in Figure 7 as micrographs of polished and etched sections. The general metallographic features for each of the alloy types are the same for both high purity and commercial grades so that the
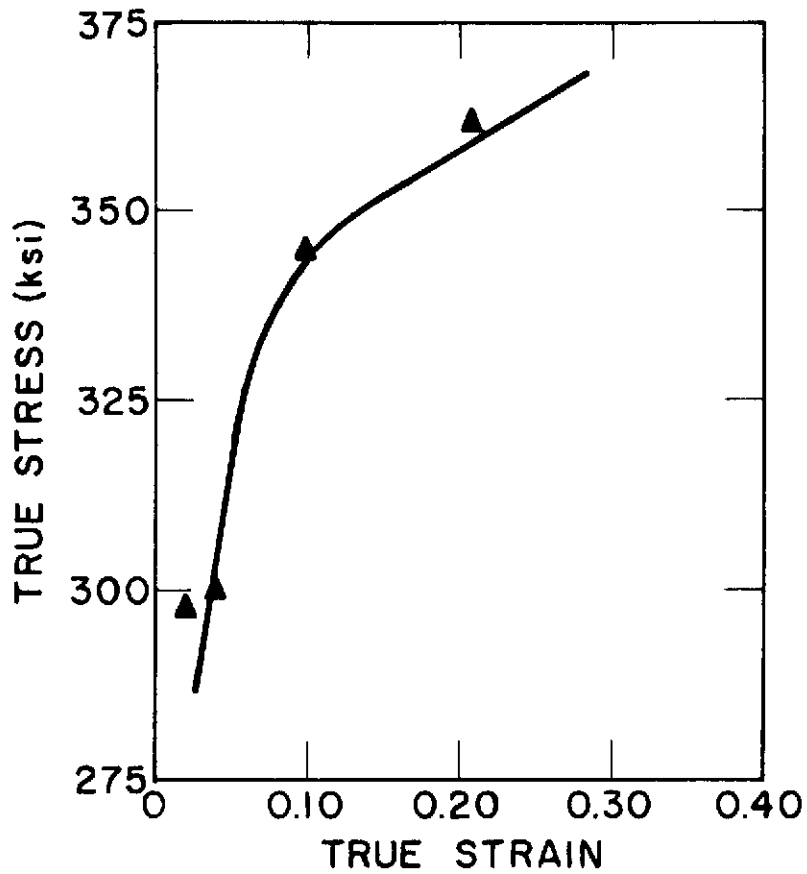
a) HIGH PURITY 18 Ni MARAGING

Note: Solid curves developed experimentally
Data points calculated using Bridgman analysis
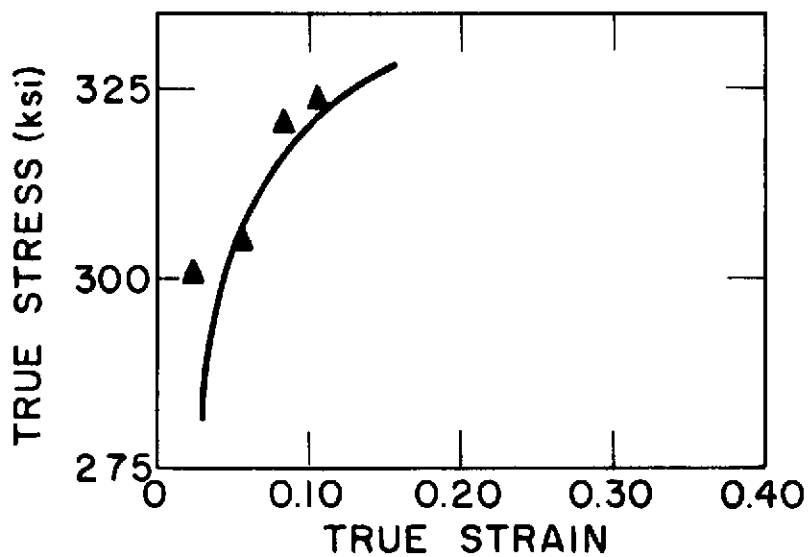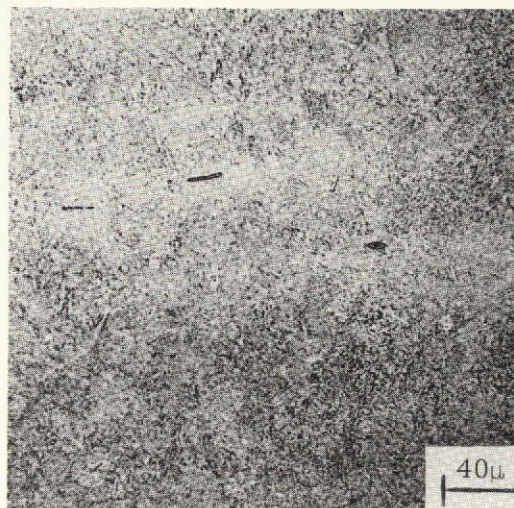
b) HIGH PURITY AISI 4340

Figure 6   Comparison of Predicted and Experimental Tensile
Curves for Notched Specimens.

illustrations presented in Figure 7 are typical. The AISI 4340 alloys are etched in a saturated solution of picric acid in ethyl alcohol and the maraging steels are etched in a concentrated aqueous solution of ferric chloride with 5% by volume hydrochloric acid added. The AISI 4340 alloys both exhibit a very fine acicular grain structure characteristic of quenched and tempered martensitic alloys as is demonstrated in the transmission electron micrograph of a two stage replica from a polished and etched section of the commercial purity alloy (Figure 7a). There is some evidence of alloy banding and the presence of non-metallic inclusions in the structures (see the optical micrograph of the high purity alloy in Figure 7b). The maraging steels exhibit a very fine precipitate structure within the prior austenite boundaries which are delineated by the etch as may be seen in the transmission micrograph of Figure 7c. As should be expected, the higher austenitizing temperature used for the commercial alloy (899° C) resulted in a slightly larger austenite grain size than in the high-purity alloy (austenitized at 843° C). Evidence of alloy banding is also prevalent in the maraging steels as is seen in Figure 7d, but the etching has generally obscured the non-metallic inclusions present in the microstructures so that they are not seen in Figure 7d.

The fine internal structure of these martensitic steels are shown in the transmission electron micrographs of Figure 8. The thin foils were produced by cutting sections approximately 0.5 mm (20 mils) thick using a water-cooled cut-off wheel. These sections were then hand ground on silicon carbide papers using water cooling to a thickness of approximately
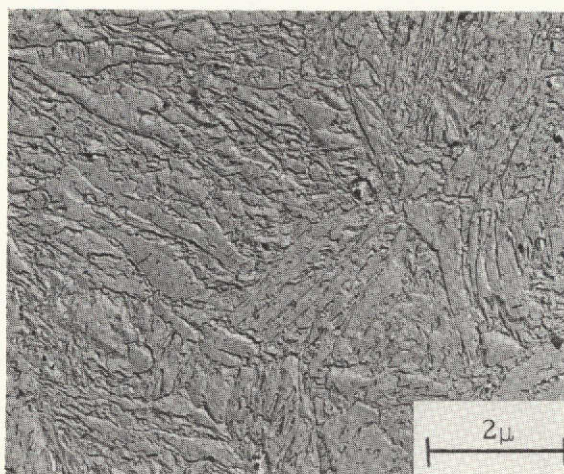
a) Transmission Micrograph of Commercial AISI 4340.

b) Optical Micrograph of High Purity AISI 4340.
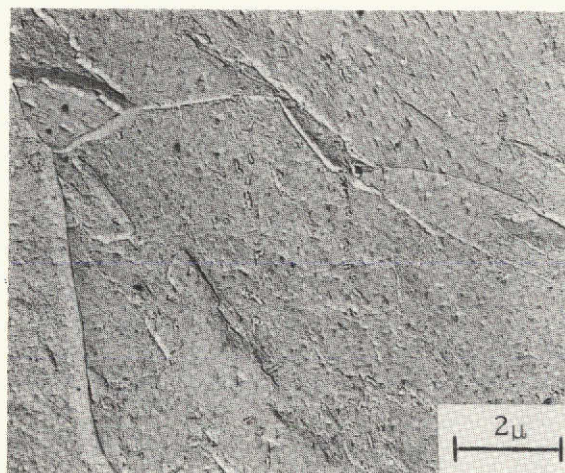
c) Transmission Micrograph of Commercial 18 Ni Maraging.

d) Optical Micrograph of High Purity 18 Ni Maraging.

Figure 7 Micrographs of Polished and Etched Sections of High Strength Steels.

0.1 mm (4-5 mils). Final thinning was accomplished electrolytically using a thinning solution of chromium trioxide in glacial acetic acid. As seen in Figure 8a, the quenched and tempered AISI 4340 alloys exhibited an acicular grain structure, high dislocation density and elongated carbides precipitated generally at the martensite lath boundaries (as indicated by the arrows in the high magnification micrograph). These observations are in agreement with previous investigators of this same alloy, tempered to the same strength level.[83]

The micrographs of the maraging steels in Figure 8b exhibit less acicular grain structures than the AISI 4340 alloys as is seen in the lower magnification micrograph, a high dislocation density, and a fine ribbon-like precipitate thought to be $Ni_3Mo$ (especially noticeable in the high magnification micrograph). These observations also coincide with those made by other investigators of maraging structures.[104]

### E. Inclusions

As indicated in Chapter II, past investigators have noted that in many instances non-metallic inclusions are the sites for void nucleation. In order to define the exact nature of the non-metallic inclusions in the four alloys, a metallographic investigation was carried out. For each of the four alloys, metallographic sections were examined from each of three orthogonal directions, the axes being defined by the rolling directions and the through thickness direction in each of the plates.

Polished sections through both of the AISI 4340 alloys revealed that the predominate inclusion type in these alloys appeared as a gray ellipse
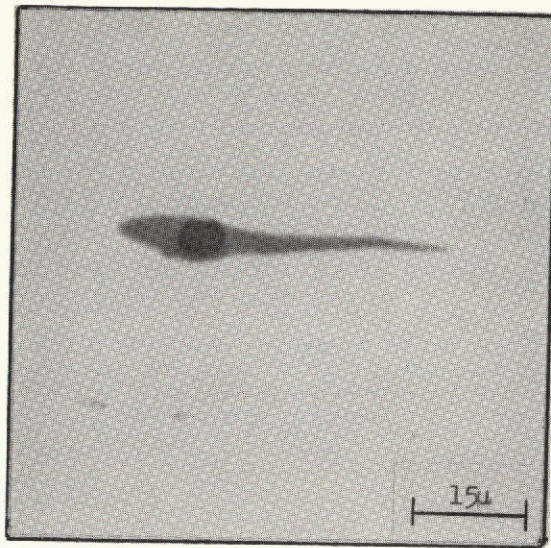
a) AISI 4340 (Arrows indicate carbides).



b) 18 Ni Maraging

This page is reproduced at the back of the report by a different reproduction method to provide better detail.

Figure 8   Transmission Electron Micrographs of High Strength Steels.

in each of the three perpendicular directions. Examples of the three orthogonal views of this inclusion type in the commercial purity AISI 4340 are shown in Figure 9. The sizes of the elliptical sections vary from view to view, being elongated in the rolling direction. In many instances, a smaller, irregular, dark particle was found within the large gray ellipse, as illustrated in the figure. The only differences noted between the non-metallic inclusions in the high-purity AISI 4340 and those in the commercial alloy were the size and axial ratios. Generally, the inclusions were observed to be larger in the commercial AISI 4340, and the major axes of the ellipses seemed more elongated in the rolling direction of the commercial alloy. Since these inclusions are oriented in the rolling directions, they were undoubtedly plastically deformed during the hot rolling operation. The exaggeration of the major axes of the ellipses in the commercial alloy as compared to the high-purity plate reflect the fact that the high-purity plate was cross-rolled, while the commercial plate was straight-away rolled. Based upon their appearance in the optical microscope and comparison with descriptions from previous inclusion studies,[105] these gray, ellipsoidal inclusions in the AISI 4340 alloys were tentatively identified as manganese sulfides (MnS); and the dark particles internal to the sulfides as some product of the deoxidation process upon which the sulfides are nucleated.
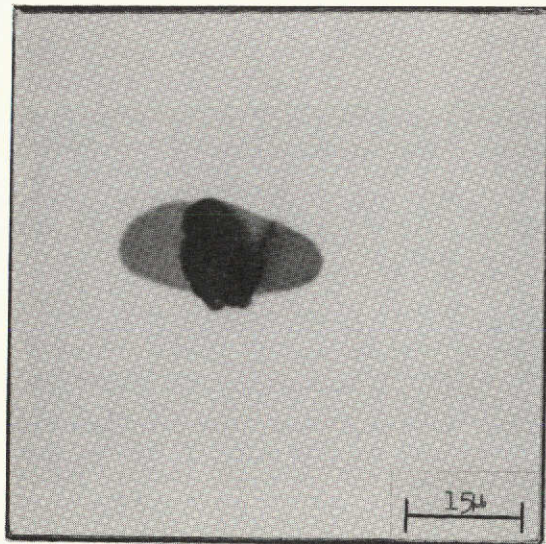
Figure 10 presents the three orthogonal views of typical examples of the most prevelant non-metallic inclusion type in the 18 Ni, 200 grade maraging alloys. Only the commercial purity alloy is presented in the figure.
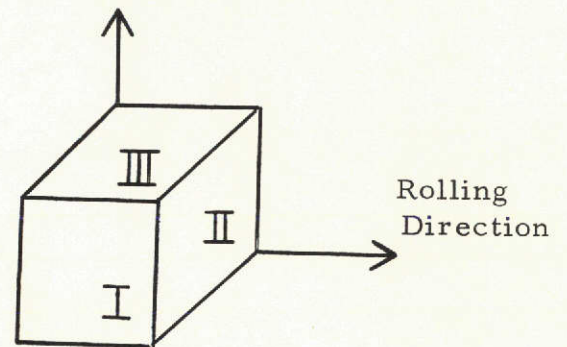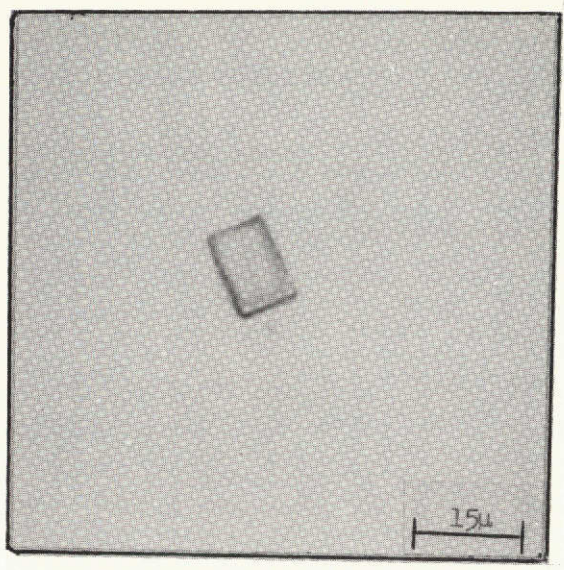
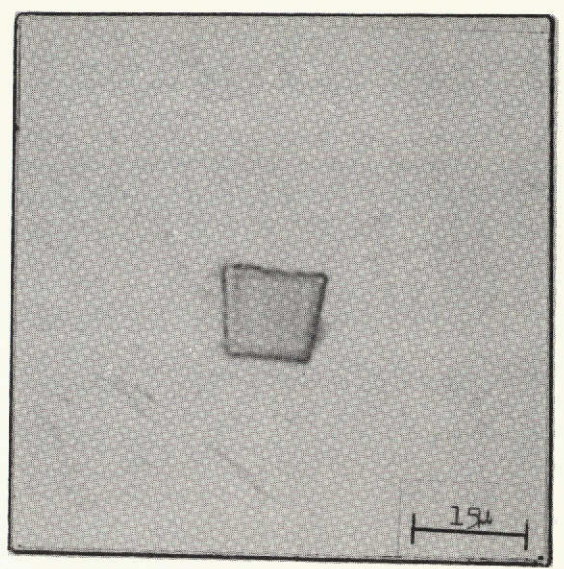Plane I
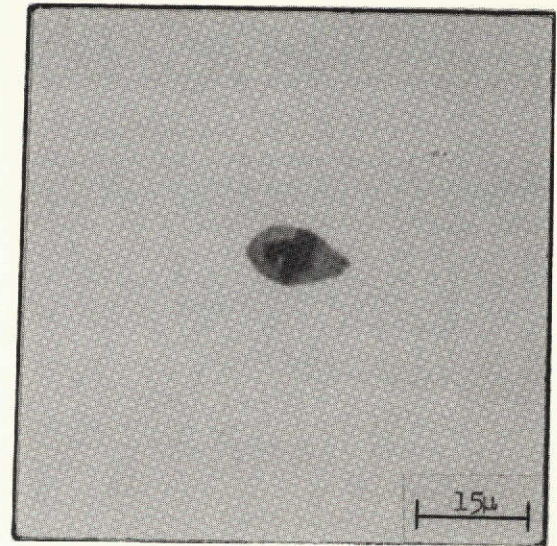


Plane II



Plane III

Thru Thickness Direction

Rolling
Direction
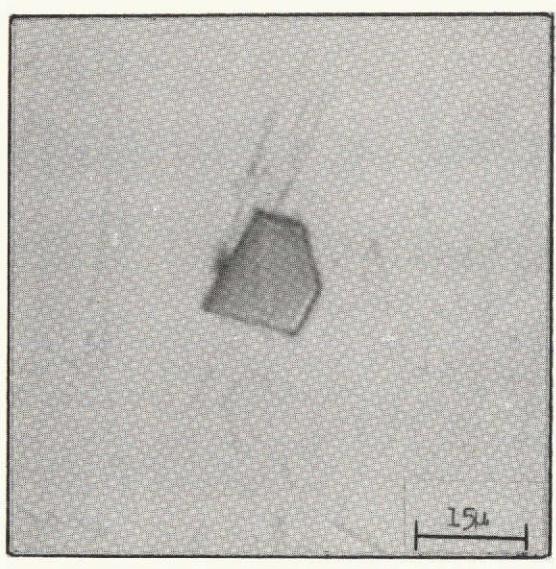
Figure 9   Optical Micrographs of Inclusions in AISI 4340 Steel
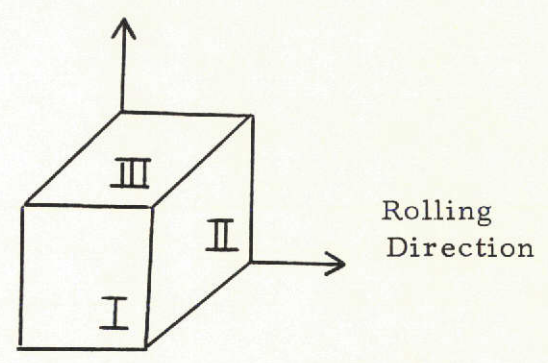
Plane I

Plane II

Plane III

Thru Thickness Direction

Rolling
Direction

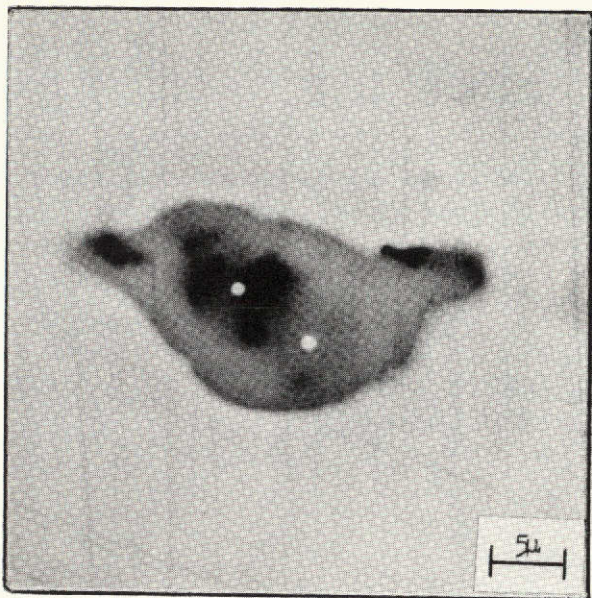Figure 10   Optical Micrographs of Inclusions in 18 Ni Maraging Steel

In all three views from both alloys, the inclusions appeared as sections of cubes and exhibited a pink color in the optical microscope. The cubes did not appear to have been plastically deformed during the hot-rolling operation, and the cubic sections appeared to have approximately the same size distribution in each of the three views of a given alloy. The cubes did appear to be larger in the commercial 18 Ni maraging steel. Comparison of these optical metallographic observations with those of a previous investigation[81] led to a preliminary identification of the inclusions in the maraging alloys as titanium carbo-nitrides (Ti(C, N)).

To ascertain whether or not the preliminary identification of the non-metallic inclusions in the four alloys was correct (as determined from the optical micrographs), specimens of each alloy, metallographically polished only through one micron diamond paste to avoid contamination, were examined by using a scanning electron microscope equipped with an X-ray energy-dispersive analyzer. Comparison of intensities of elemental characertistic X-rays from the inclusions and matrices confirmed the postulated inclusion identifications. The ellipsoidal inclusions in both the commercial and high-purity AISI 4340 alloys were found to be richer in manganese and sulfur than the matrix. The small irregular inclusions upon which the sulfides apparently nucleated were found to contain greater amounts of calcium and aluminum than the matrix in the commercial AISI 4340, suggesting that they are, in fact, a deoxidation product. (It is impossible to analyze for oxygen using this technique.) Unfortunately, the nucleating particles within the manganese sulfides were too small in the

high-purity AISI 4340 to provide sufficient volume for analysis. Figure 11 is an example of representative micrographs of a manganese sulfide inclusion in the commercial AISI 4340 alloy. Included are photomicrographs taken in the secondary electron mode and subsequent elemental X-ray scans of the same area. It is readily seen that the inclusion is rich in manganese and sulfur and that the dark nucleating particle is rich in aluminum. The bright spots within the nucleating particle and the sulfide in the micrograph produced in the secondary mode are due to contamination of areas where the electron beam was focused for prolonged X-ray counting in order to analyze the inclusions.

The same procedure was used for analyzing the inclusions in both maraging alloys. A representative example of micrographs taken of a suspected titanium carbo-nitride is presented in Figure 12. Again, the bright spots on the photograph taken in the secondary electron mode are points where prolonged X-ray counting was carried out. The inclusion is richer in titanium than the matrix. Unfortunately, no analysis can be made for carbon or nitrogen using this technique, but the detection of titanium together with their optical appearance strongly indicates that the cuboidal inclusions in the maraging alloys are titanium carbo-nitrides.

A quantitative metallographic investigation was undertaken to determine the exact nature of the inclusion populations in the four alloys. Based on the definition of the inclusion shapes indicated above, established quantitative metallographic techniques were used to determine the numbers, spacings, and sizes of the inclusions in the alloys. Polished plane sections
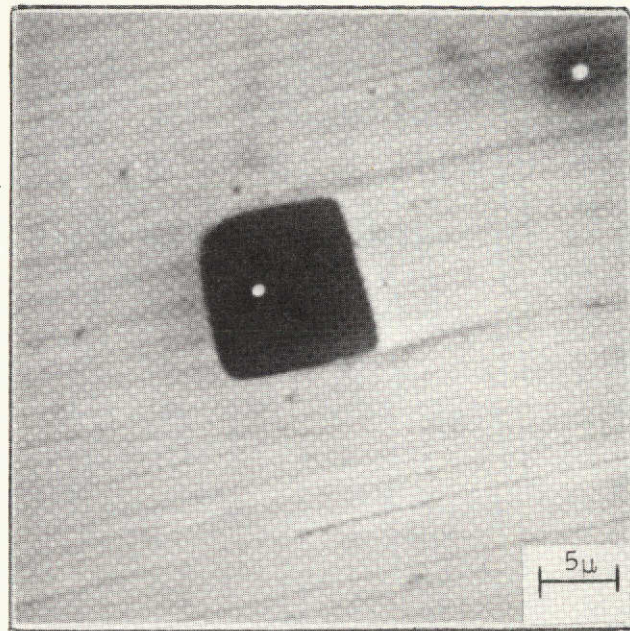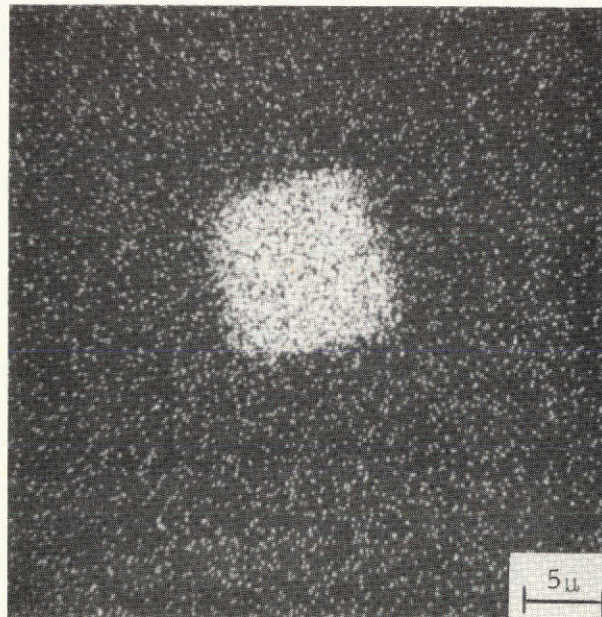
Secondary Electron Mode
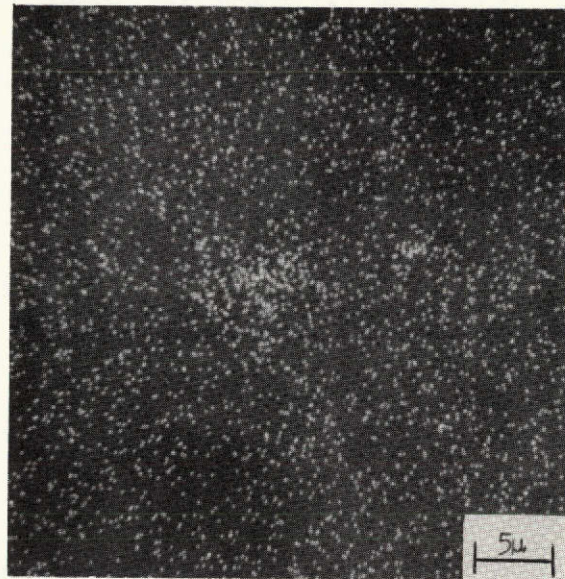


X-Ray Scan for Aluminum
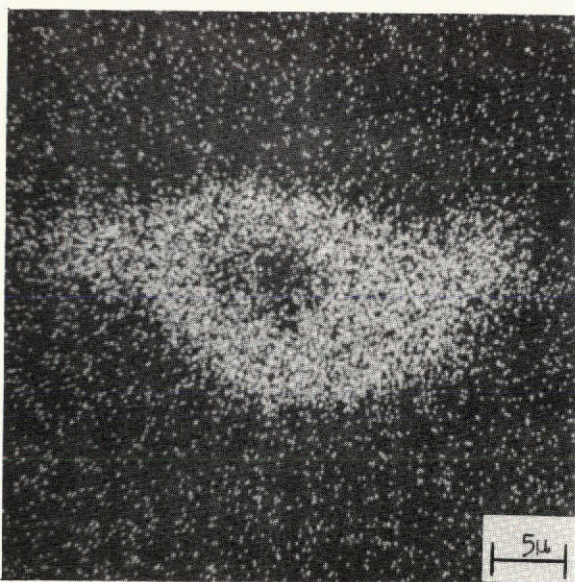
Figure 11 - Scanning Electron Micrographs of Inclusion in
AISI 4340 Steel

Secondary Electron Mode



X-ray Scan for Titanium

This page is reproduced at the back of the report by a different reproduction method to provide better detail.

Figure 12  Scanning Electron Micrographs of Inclusion in 18 Ni Maraging Steel.

normal to each of the three orthogonal axes as defined by the rolling directions and plate thicknesses were examined for each alloy. Optical photomicrographs were taken at sixteen predetermined positions on each plane section. The positions were defined by four-point by four-point square arrays on the sections. Photomicrographs were taken at a magnification of 250X and then enlarged to 500X to facilitate counting and measuring of the inclusions in each view. All features which could be identified as inclusions were counted and their dimensions measured.

As shown above, the manganese sulfide inclusions in the AISI 4340 alloys have the shape of ellipsoids, with their three unequal axes aligned in the orthogonal directions defined by the rolling direction, the cross-rolling direction, and the through thickness direction of the plates. The quantitative metallographic analysis for this shape is due to DeHoff and Rhines,[106,107] assuming a constant shape ellipsoid, i. e., the ratio of the axes remains constant. The dimensions of the ellipsoid are defined by the lengths of its three axes: $d_1$ (along the primary rolling direction), $d_2$ (along the cross-rolling direction), and $d_3$ (along the direction through the plate thickness). The number of inclusions per unit area observed on a test section perpendicular to axis 1 (the primary rolling direction) is given the symbol $N_{A1}$. Similarly defined are $N_{A2}$ and $N_{A3}$. Furthermore, $Z_{13}$ is defined as the reciprocal of the length of the axis of those elliptical sections which are seen on plane "one" (normal to the primary rolling direction) with the measurement being made in the "three" direction (the through thickness direction).

The number of ellipsoidal inclusions per unit volume of material $(N_V)$ is then given by the expression:

$$N_V = \frac{2}{\pi} N_{A3} \bar{Z}_{13} . \qquad \text{[IV-4]}$$

The mean dimensions of the ellipsoidal inclusions $(\bar{d}_i)$ are given by:

$$\bar{d}_1 = \frac{\pi N_{A1}}{2 N_{A3} \bar{Z}_{13}} \qquad \text{[IV-5]}$$

$$\bar{d}_2 = \frac{\pi N_{A2}}{2 N_{A3} \bar{Z}_{13}} \qquad \text{[IV-6]}$$

$$\bar{d}_3 = \frac{\pi}{2 \bar{Z}_{13}} . \qquad \text{[IV-7]}$$

The titanium carbo-nitrides which are the predominate inclusion type in the 18 Ni maraging alloys have the shape of cubes as illustrated above and have no preferred orientation in the matrix. The quantitative metallographic treatment of this shape is due to Hull and Houk[108] and Myers.[109] The number of inclusions per unit area observed on a random plane is given the symbol $N_A$, and the number of interceptions of inclusions per unit length of a test line radomly placed on plane sections is given the symbol $N_L$.

The number of cuboidal inclusions per unit volume of material $(N_V)$ is then given by the expression:

$$N_V = \frac{2N_A^2}{3N_L} . \qquad \text{[IV-8]}$$

The average dimension of the cube edges $(\bar{a})$ is given by:

$$\bar{a} = \frac{N_L}{N_A} . \qquad \text{[IV-9]}$$

For both types of inclusion shape, the average center-to-center distance ($\bar{\lambda}$) between the nearest neighbor inclusions in a unit of volume is given by an expression first derived by Hertz:[110]

$$\bar{\lambda} = 0.554 \, N_v^{-1/3} \, . \qquad\qquad \text{[IV-10]}$$

The volume fraction of inclusion particles ($V_v$) contained in any of the alloys was determined using a standard point counting technique with a 1/4-inch square point grid at 500X. The average fraction of points falling on the inclusions is given the symbol $\bar{P}_p$ and the volume fraction of inclusions ($V_v$) is then equal to the average point fraction:[112]

$$V_v = \bar{P}_p \qquad\qquad \text{[IV-11]}$$

The results of the quantitative metallographic study are summarized in Table III. The limits given for each reported value represent plus and minus one standard deviation (approximately 70 percent confidence limits). It should be noted from the table that the number of inclusions per unit volume is greater for the high-purity alloys than for the commercially produced plates, but that the inclusion sizes and volume fractions are substantially larger in the commercial alloys. Note also that the volume fractions of inclusions in the maraging steels are larger than in the AISI 4340 alloys. The center-to-center spacing of inclusions follows the inverse relation of the number per unit volume, namely, the interparticle spacings are greater in the commercial alloys than in the high purity alloys. As may be seen from the results, the variability of the various measurements is quite high. However, treatment of the data using standard statistical

TABLE III

Results of Quantitative Metallographic Investigation
of Inclusions in High Strength Steels

| | Commercial AISI 4340 | High Purity AISI 4340 | Commercial 18 Ni Maraging | High Purity 18 Ni Maraging |
|---|---|---|---|---|
| $N_v$ $\left(\dfrac{\text{inclusions}}{\text{cm}^3}\right)$ | $4.9 \times 10^6 \pm 2.6 \times 10^6$ | $6.8 \times 10^6 \pm 4.6 \times 10^6$ | $2.9 \times 10^6 \pm 1.5 \times 10^6$ | $5.4 \times 10^6 \pm 5.1 \times 10^6$ |
| $\overline{d}_1$ or $\overline{a}$ ($\mu$) | $9.7 \pm 5.8$ | $4.5 \pm 4.1$ | $8.6 \pm 6.4$ | $3.0 \pm 3.8$ |
| $\overline{d}_2$ ($\mu$) | $7.3 \pm 6.3$ | $4.9 \pm 4.2$ | --- | --- |
| $\overline{d}_3$ ($\mu$) | $5.5 \pm 1.4$ | $3.3 \pm 0.2$ | --- | --- |
| $\overline{\lambda}$ ($\mu$) | $33 \pm 6$ | $29 \pm 7$ | $39 \pm 7$ | $32 \pm 10$ |
| $V_v$ (%) | $0.14 \pm 0.05$ | $0.06 \pm 0.03$ | $0.21 \pm 0.08$ | $0.09 \pm 0.05$ |

methods for hypotheses concerning two means[113] shows that the above

conclusions concerning numbers, sizes, and spacings of the inclusions are

statistically meaningful with 90 percent confidence.

Analysis of the data for the AISI 4340 alloys reveals that the num-

ber of inclusions per unit volume in the high-purity alloy is greater by at

least $0.2 \times 10^6$ inclusions/cm$^3$ than in the commercial grade plate.

Similarly, with 90 percent confidence, the average inclusion size is larger

in the commercial alloy with $\bar{d}_1$ at least $2.9\mu$ greater than in the high-purity

alloy. Likewise, $\bar{d}_2$ and $\bar{d}_3$ are at least $0.1\mu$ and $1.7\mu$ greater, respec-

tively, in the commercial AISI 4340 than in the high-purity melt. It was

also determined that $\bar{\lambda}$ is at least $1.7\mu$ larger in the commercial alloy than

in the high-purity alloy, and that $V_v$ is at least 0.04 percent greater in the

commercial alloy.

Similar statistical treatment of the data for the 18 Ni, 200 grade

maraging steels shows that $N_v$ of the high-purity melt is at least $0.8 \times 10^6$

inclusions/cm$^3$ greater than $N_v$ for the commercial alloy, again with 90

percent confidence. The size of the average titanium carbo-nitride cube

edge is at least $3.2\mu$ greater in the commercial alloy while $\bar{\lambda}$ also is at

least $3.0\mu$ greater in the commercial alloy than in the high-purity plate of

18 Ni, 200 grade maraging steel. The volume fraction of inclusions in the

commercial maraging steel was at least 0.05 percent greater than in the

high-purity alloy.

CHAPTER V

FRACTOGRAPHY

A. <u>Comparison of Fracture Surfaces from Various Fracture Tests</u>

A fractographic study was carried out on the four alloys to define

the nature of the fracture surfaces. The fracture surfaces from compact

tension specimens ($K_{Ic}$ specimens), smooth, round tensile bars, and mildly

notched tensile bars were examined for each alloy. (The only exception was

the commercial 18 Ni, 200 grade maraging steel for which no compact ten-

sion fracture surfaces were available.) Examination of the available com-

pact tension fracture surfaces for the alloys at low magnification showed

them to be rough and fibrous in appearance. Both the smooth and notched

round tensile bars for all alloys exhibited a cup and cone type fracture, al-

though the sizes of the shear lips on the notched tensile specimens were much

smaller than those of the smooth specimens. The central regions on all the

tensile bars were rough and fibrous in appearance when viewed at lower

magnification.

Two stage, cellulous acetate-platinum shadowed carbon replicas

were taken from the areas of fast fracture initiation on the $K_{Ic}$ fracture sur-

faces and from the central areas of normal rupture on the smooth and notched

tensile fracture surfaces for each of the alloys. The replicas were examined

using an electron microscope, and it was found that the features on the fracture surfaces were qualitatively the same for each of three fracture tests ($K_{Ic}$, smooth round tension and notched round tension) of any given alloy. The fractures were entirely by dimpled rupture (plastic fracture). Examples of representative fractographs taken of replicas from each type of fracture test specimen for the four alloys are presented in Figures 13-16. Note the great similarity of the features on the fracture surfaces of all test specimens for any particular steel and the similarity of fracture surfaces for both commercial and high-purity heats of the two alloy types. Detailed examination of the fracture surfaces follows in the next two sections. All reported observations are based upon extensive examination of stereo pairs.

## B.  18 Ni Maraging Fracture Surfaces

Fractographs at higher magnifications than those found in the previous section are presented in Figures 17 and 18 as representative of the fracture surfaces of both 18 maraging steels. Examination of these figures reveals the fracture surfaces to be almost completely covered by large equiaxed dimples approximately 10-20 microns in diameter. At the positions marked "X" on the fractographs, examples of impressions of carbonitride particles may be seen at the bottoms of dimples. The particular carbo-nitride marked "Y" in Figure 18 exhibits clearly a cleavage fracture pattern, suggesting that the associated dimple was nucleated by the separation of the halves of the fractured non-metallic inclusion. The observation of cleavage patterns on carbo-nitride particles in the large dimples of the maraging steels was a general observation. It should also be noted that the
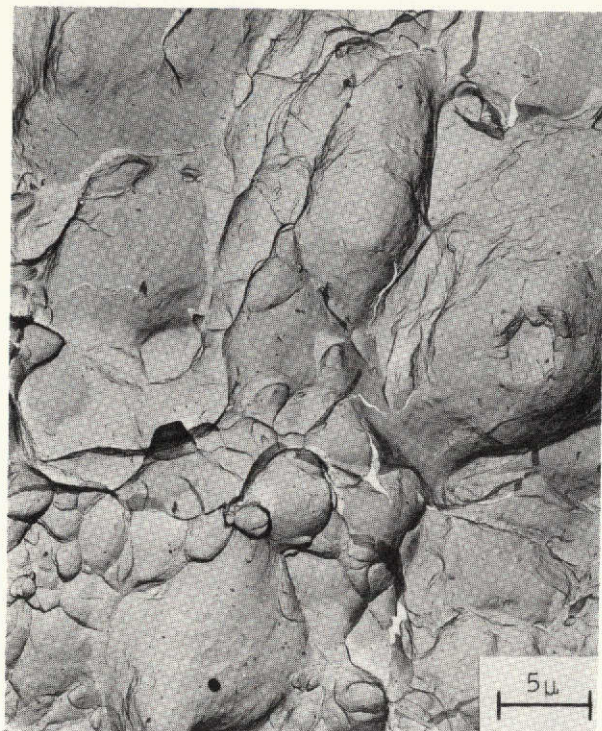
56



Smooth Tension



Notched Tension

Figure 13    Electron Fractographs of Commercial 18 Ni Maraging Steel

Smooth Tension

Notched Tension

$K_{Ic}$

Figure 14   Electron Fractographs of High-Purity 18 Ni Maraging Steel.

Smooth Tension

Notched Tension
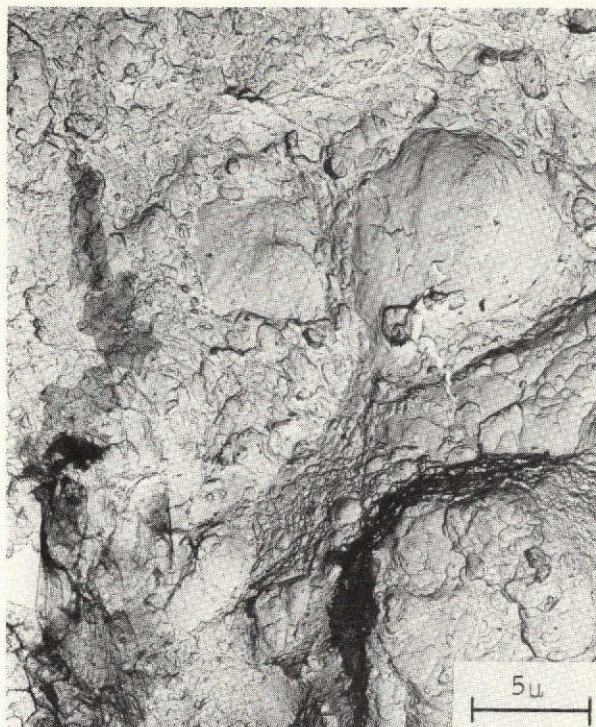
$K_{Ic}$

Figure 15    Electron Fractographs of Commercial AISI 4340 Steel

Smooth Tension
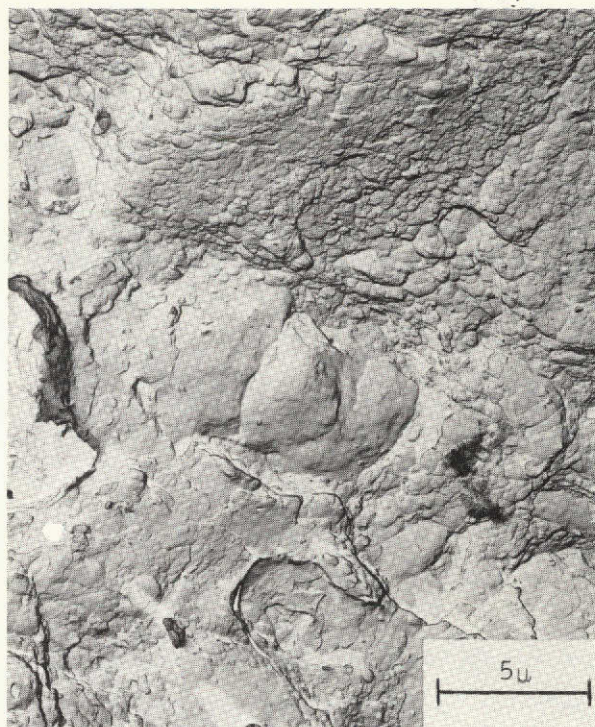
Notched Tension

$K_{Ic}$

This page is reproduced at the back of the report by a different reproduction method to provide better detail.

Figure 16  Electron Fractographs of High Purity AISI 4340 Steel.

Figure 17  Electron Fractograph From Central Region of Smooth
Tensile Fracture in Commercial 18 Ni Maraging Steel.
(Carbo-nitrides indicated by X; Deformation markings
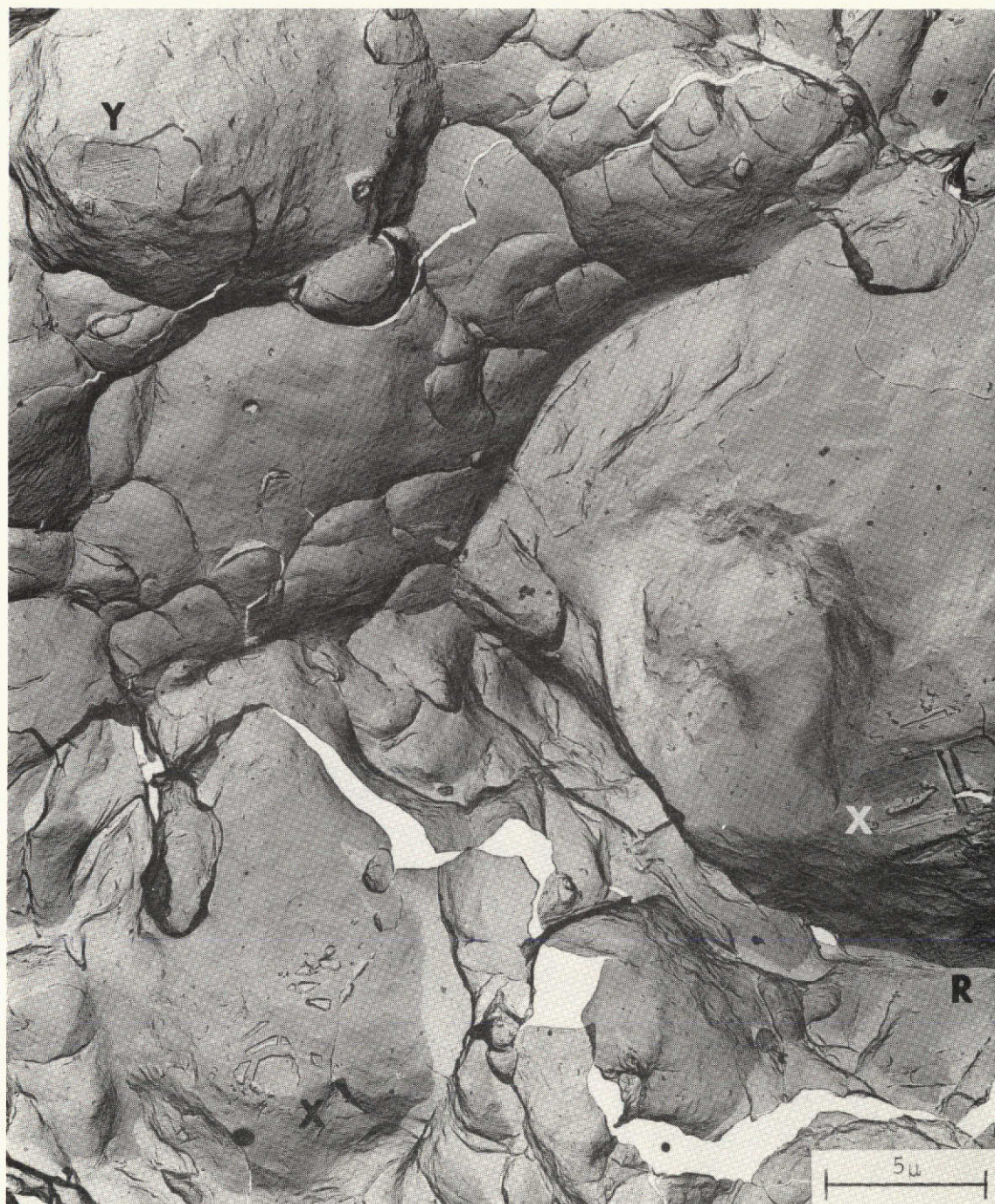indicated by R).

Figure 18  Electron Fractograph from Central Region of Smooth
Tensile Fracture in High-Purity 18 Ni Maraging Steel.
(Carbo-nitrides indicated by X; Cleavage fracture
pattern on carbo-nitride indicated by Y; Deformation
markings indicated by R).

carbo-nitride particles marked by "X" in the two figures appear to be either collections of a number of particles or the fragmented pieces of a shattered single inclusion. A clearer illustration of this point is presented in Figure 19. Stereoscopic examination of this fractured carbo-nitride lying in the bottom of a large dimple revealed that the pieces fit together much like a jig saw puzzel as indicated by matching the lettered points in Figure 19. Although a few carbo-nitrides were observed to be cracked in the commercial maraging steel in the previously discussed metallographic study and as discussed further in the following chapter, no separation of broken pieces nor noticeable clustering of inclusions was observed in the plane section examinations. The conclusion is that the shattering and substantial separation of the broken pieces of the carbo-nitrides observed on the fracture surfaces occurred during the fracture process.

At the positions marked "R" in Figures 17 and 18, evidence of surface rumpling of the dimple walls is seen. These wavy, linear features are reminiscent of the intense deformation markings on the free surfaces of tensile specimens which have been strained well into the plastic region. The implication is that the dimple walls were, in fact, free surfaces during a portion of the plastic deformation of the matrix and that large amounts of plastic deformation occurred after void initiation.

C. AISI 4340 Fracture Surfaces

Representative fractographs of the fracture features observed on the AISI 4340 fracture surfaces are presented in Figures 20 and 21. Each of these fractographs is composed of a large dimple 5-15 microns in

1.0µ

Figure 19   Fractured Carbo-Nitride on Notched Tension Fracture
Surface of High-Purity 18 Ni Maraging Steel.
(Like letters indicate matching points of shattered
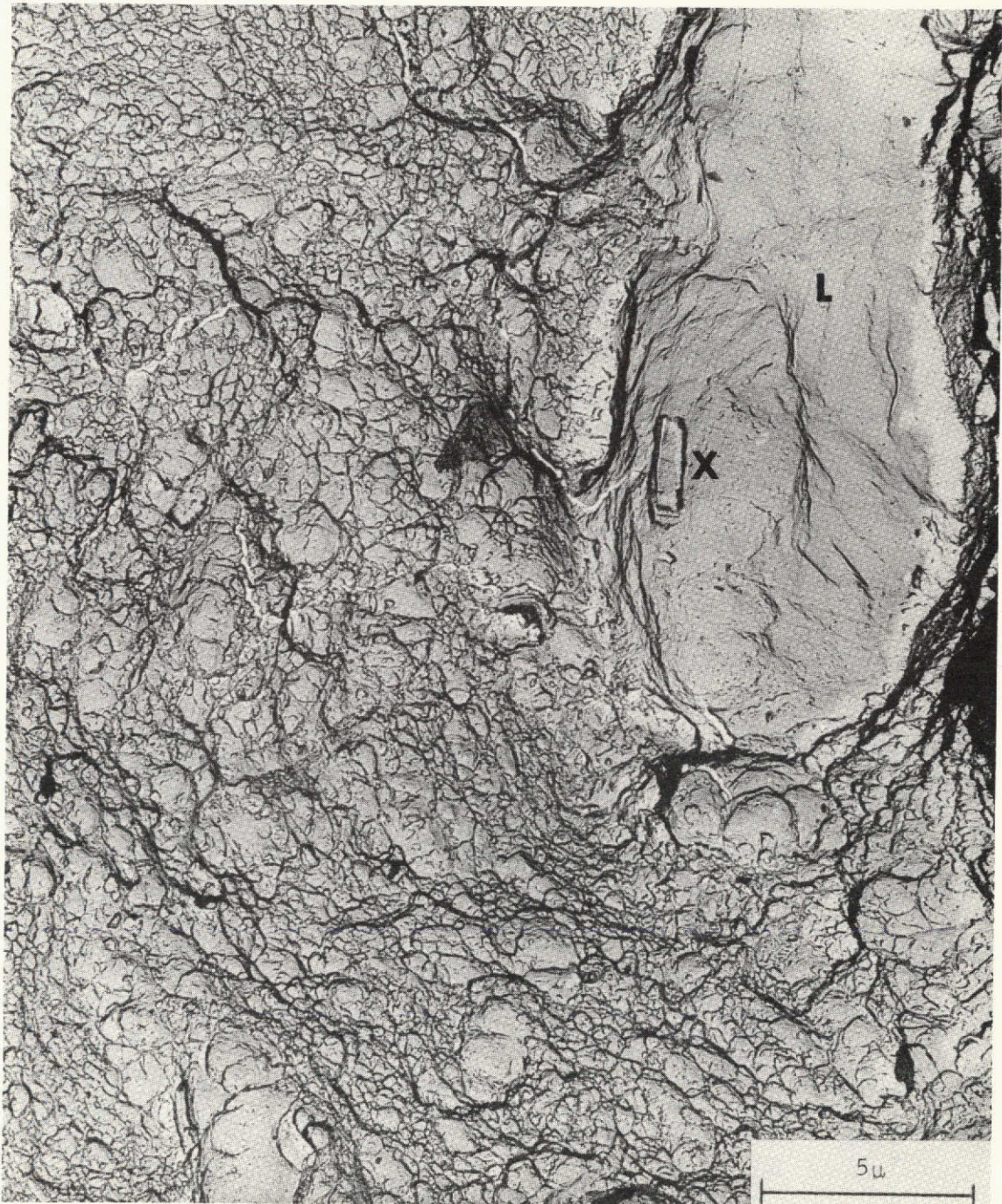inclusion).

Figure 20   Electron Fractograph from Central Region of Smooth
Tensile Fracture of Commercial AISI 4340 Steel.
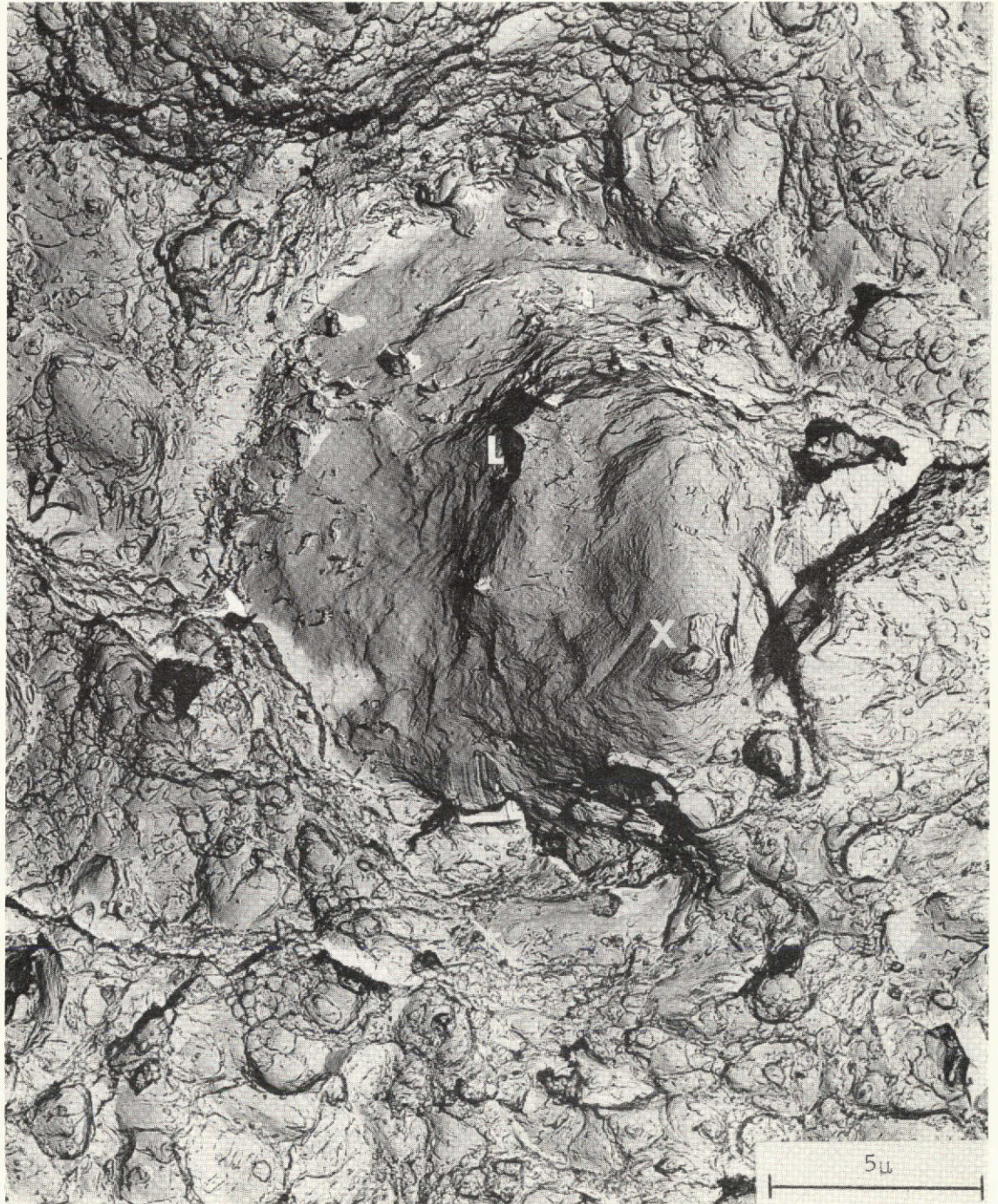(Large dimple indicated by L; Nucleating particle
indicated by X).

Figure 21   Electron Fractograph from Central Region of Smooth
Tensile Fracture of High-Purity AISI 4340 Steel.

diameter marked with the letter "L" in the figures while the remainder of

the area of each fractograph is covered with very fine dimples one-to-two

orders of magnitude smaller. No fundamental differences between the

fractures of the high-purity and commercial AISI 4340 alloys could be dis-

cerned from their fracture surfaces. Both alloys exhibit extensive surface

rumpling on the large dimple walls as was observed in the maraging steels.

The points marked "X" within the large dimples are most probably the im-

pressions of the nucleating particles for the large dimples. Although the

replicated shapes of these particles are not distinctive, their general sizes

correspond with those of the manganese sulfide particles indentified as the

predominate non-metallic inclusions in these AISI 4340 steels. An example

of a nucleating particle (determined using stereoscopy) in a large dimple

in the AISI 4340 alloys whose shape is more easily associated with the pre-

viously established ellipsoidal shape of the sulfides is shown in Figure 22.

Some evidence of deformation markings and steps on the inclusion surface

was observed by stereoscopy with these features indicated by the arrows

in the figure.

Careful examination of the areas of fine dimples shows that many of

these small dimples contain the impression of a nucleating particle. Exam-

ples of these impressions are marked by "X" in Figure 23, a fractograph

of a region of small dimples taken at high magnification. The small size

of these particles suggests that they may be carbides but conclusive demon-

stration of this hypothesis must wait for a later section of this chapter. Al-

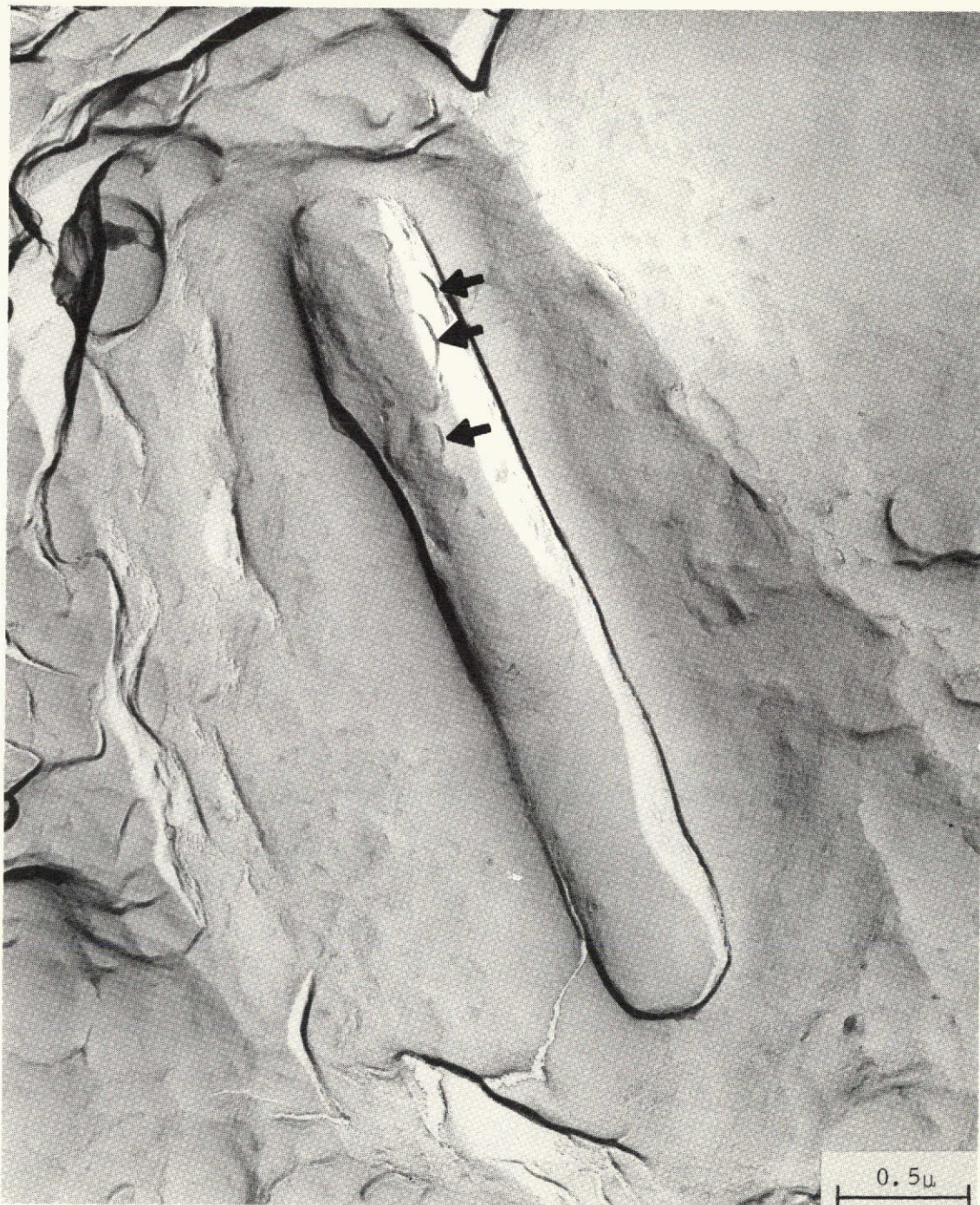though many of the fine dimples in Figures 20 and 21 appear to be shear-type

Figure 22   Sulfide on Notched Tension Fracture Surface of Commercial
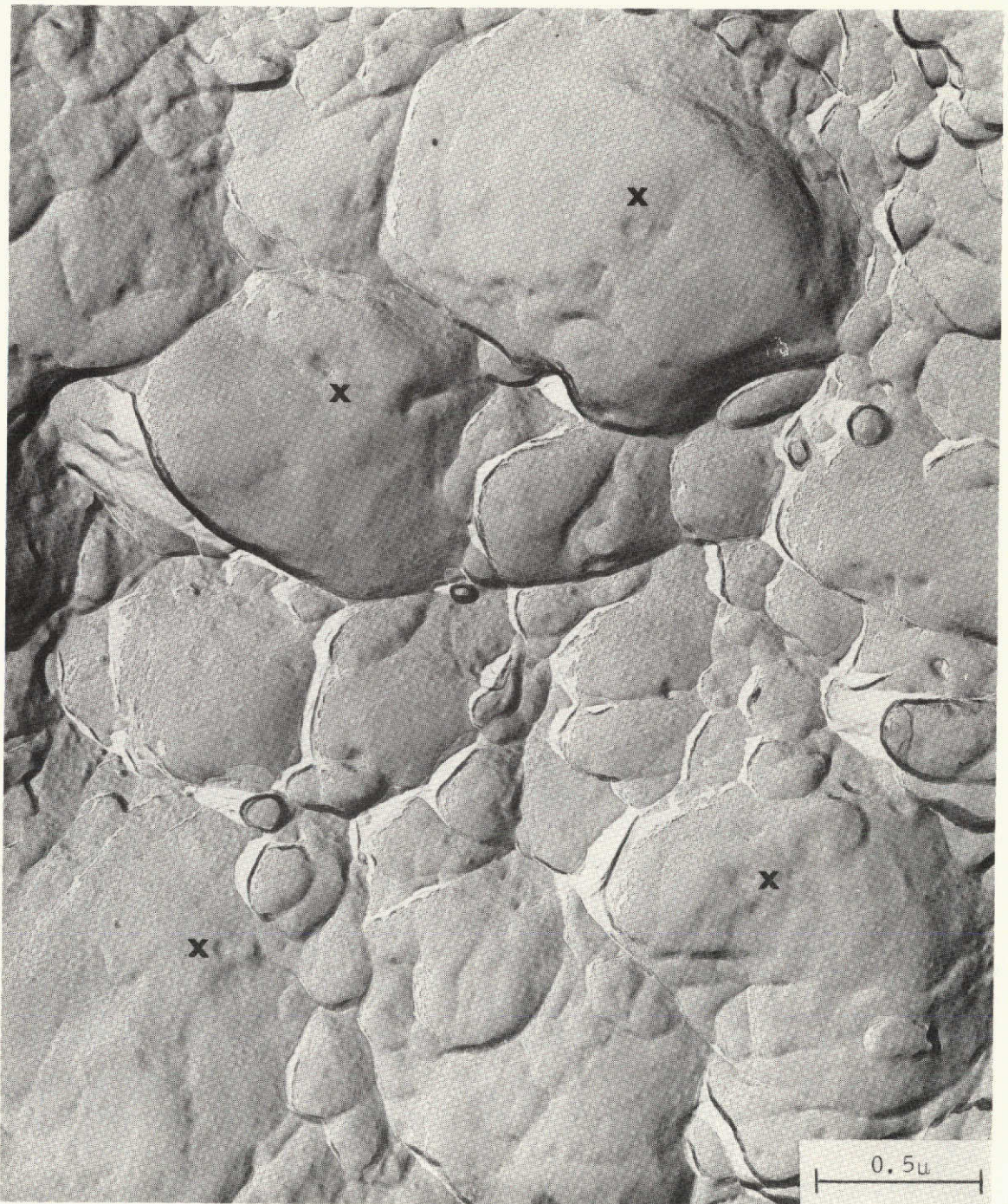AISI 4340 Steel.
(Deformation markings indicated by arrows).

Figure 23  Fine Dimples on Notched Tension Fracture of Commercial AISI 4340 Steel.
(Impressions of nucleating particles indicated by X).

dimples, stereoscopic viewing reveals that most of the small dimples are in fact equiaxed. It is important to base fractographic observations only upon stereoscopic evidence since it is quite possible to have equiaxed dimples appear as shear dimples and vice versa if only single photographs are used. [114, 115]

## D. Measurements Taken from Fracture Surfaces

In a further attempt to understand the relationship between the non-metallic inclusions in these alloys and the features on the fracture surfaces, a series of quantitative measurements of dimple spacings were made on the fractographs. The procedure followed was to consider the fracture surfaces as plane sections and the dimples to be analogous to grains, such that the measurements made were those generally associated with the determination of the average linear distance across a grain as given by Smith: [159]

$$\overline{D} = L/N \qquad\qquad [V-1]$$

where L is the length of test line traversing the test section, and N is the number of cell boundaries intersected by the legnth of test line. This treatment of the rough fracture as if it were a flat surface obviously introduces error, but should give a first approximation to the average diameter of the dimples, or, of more interest, the treatment provides an approximation to the average center-to-center spacing of the dimples. Measurements were made on all three types of fracture surface ($K_{Ic}$, smooth round tensile and notched round tensile specimens) to provide a quantitative comparison between the fractures from the three tests for each alloy. Extensive use was made of stereographic pairs of fractographs to facilitate distinguishing

accurately the boundaries between dimples. The results of the measurements from the fractographs are presented in Table IV, together with a tabulation of the average inclusion spacing determined earlier by quantitative metallography to permit ready comparison. All limits on the data represent plus and minus one standard deviation.

The results in Table IV point to a correlation between the average inclusion spacing as determined by quantitative metallography and the approximation of the large dimple spacings. The reasonable agreement between these measurements for each alloy is remarkable when considering the approximations made in the determination of dimple spacings. These results coupled with the frequent association of large dimples and inclusions on the fracture surfaces, as shown by the fractographs, strongly suggest that the large dimples are the result of void initiation at the non-metallic inclusions. One more point should be made concerning the data presented in Table IV. The approximate values of large dimple spacings determined from $K_{Ic}$ and the two types of tensile fracture surfaces are essentially the same for the three tests for any given alloy. Good agreement is also found among the small dimple spacings from $K_{Ic}$ and tensile fractures in the AISI 4340 alloys. This correlation confirms the previous observation that the fracture surface features in the region of fast fracture initiation on $K_{Ic}$ specimens are the same as those from the central regions of normal rupture on the smooth and notched round tensile bars for these alloys. Thus, it is suggested that the initial or critical processes which lead to fracture

TABLE IV

Approximations of Dimple Spacings on Fracture Surfaces of High Strength Steels

| | Commercial AISI 4340 | High Purity AISI 4340 | Commercial 18 Ni Maraging | High Purity 18 Ni Maraging |
|---|---|---|---|---|
| $\bar{\lambda}$<br>Spacing of Inclusions from Polished Sections ($\mu$) | 33 ± 6 | 29 ± 7 | 39 ± 7 | 32 ± 10 |
| $\bar{D}_K$<br>Approximate Spacing of Large Dimples on $K_{Ic}$ Fractures ($\mu$) | 18 ± 7 | 24 ± 6 | - | 14 ± 3 |
| $\bar{D}_S$<br>Approximate Spacing of Large Dimples on Smooth Tensile Fractures ($\mu$) | 23 ± 11 | 16 ± 6 | 26 ± 14 | 17 ± 5 |
| $\bar{D}_N$<br>Approximate Spacing of Large Dimples on Notched Tensile Fractures ($\mu$) | 24 ± 1 | 34 ± 13 | 27 ± 13 | 31 ± 6 |
| $\bar{d}_K$<br>Approximate Spacing of Small Dimples on $K_{Ic}$ Fractures | 0.3 ± 0.1 | 0.6 ± 0.2 | - | - |
| $\bar{d}_S$<br>Approximate Spacing of Small Dimples on Smooth Tensile Fractures ($\mu$) | 0.4 ± 0.1 | 0.4 ± 0.2 | - | - |

TABLE IV (continued)

| | Commercial AISI 4340 | High Purity AISI 4340 | Commercial 18 Ni Maraging | High Purity 18 Ni Maraging |
|---|---|---|---|---|
| $\bar{d}_N$ Approximate Spacing of Small Dimples on Notched Tensile Fractures ($\mu$) | $0.8 \pm 0.1$ | $0.7 \pm 0.1$ | - | - |
| Fraction of $K_{Ic}$ Fracture Surface Covered by Small Dimples (%) | $91.2 \pm 0.4$ | $97.0 \pm 0.2$ | $\sim 0$ | $\sim 0$ |
| Fraction of Smooth Tensile Fracture Surface Covered by Small Dimples (%) | $92.3 \pm 1.0$ | $94.3 \pm 0.5$ | $\sim 0$ | $\sim 0$ |
| Fraction of Notched Tensile Fracture Surface Covered by Small Dimples (%) | $93.1 \pm 0.6$ | $93.9 \pm 0.3$ | $\sim 0$ | $\sim 0$ |

are similar for all three tests in these particular alloys.

The major difference between the fracture surfaces of the 18 Ni, 200 grade maraging steels and the AISI 4340 steels is the much greater fraction of the fracture surfaces of the AISI 4340 steels covered by very fine dimples approximately half a micron in diameter. Using the same point counting technique as outlined in the preceding chapter (that due to Underwood)[111] and assuming again that the fracture surfaces were flat, a determination of the fraction of the areas of the fracture surfaces covered by small dimples was carried out. The results of these measurements are also presented in Table IV. Note again that the results from the three fracture tests are comparable. Although there was some evidence of a few small dimples on the 18 Ni, 200 grade maraging fracture surfaces (see Figures 17 and 18), the areas of small dimples were not extensive enough to measure a statistically significant area fraction for the maraging alloys. The maraging fracture surfaces considered as a whole had approximately 100 percent area fraction of large dimples.

E. Extraction of Particles from Fracture Surfaces

The sizes of the small dimples on the AISI 4340 fracture surfaces and the sizes of the impressions of nucleating particles within them suggest that the small dimples are nucleated on carbide particles in the quenched and tempered martensitic structure. In order to determine the nucleating particles for these fine dimples, a series of extraction replicas were taken from smooth tensile fracture surfaces of both AISI 4340 alloys. The replicas were made by shadowing the actual fracture surfaces with

platinum from an angle of approximately 45° and then evaporating a heavy coating of carbon onto the fracture surfaces from directly overhead. The fracture surfaces with carbon and platinum deposits were immersed in a one percent solution of bromine in methyl alcohol for about one minute to attack the matrix and help expose the particles in the bottoms of the dimples. The fractures were than soaked while agitated for several hours in ethyl alcohol to remove all the bromine solution. The central portions of the tensile fractures were then scribed and electropolished in a solution of perchloric acid, ethyl alcohol, and glycerol during which the scribed blocks of carbon replica floated off the fracture surfaces. The replicas, after cleaning in ethyl alcohol, were examined in the electron microscope.

The procedure outlined above resulted in the extraction of many fine particles associated with the small dimples on the fracture surfaces of both commercial and high-purity AISI 4340 alloys. An example of an extraction replica taken from the commercial alloy is presented in Figure 24. Examples of extracted particles are indicated by the arrows on the fractograph. In order to identify the particles, electron diffraction techniques using the electron microscope were employed so that individual particles associated with the small dimples could be examined. Figure 25 presents individual extracted particles from both the commercial and high-purity fracture surfaces, together with the selected area electron diffraction patterns from the particles. The concentric ring patterns about the central spots of the diffraction patterns result from the fine grained polycrystalline platinum deposits used to shadow the replicas,
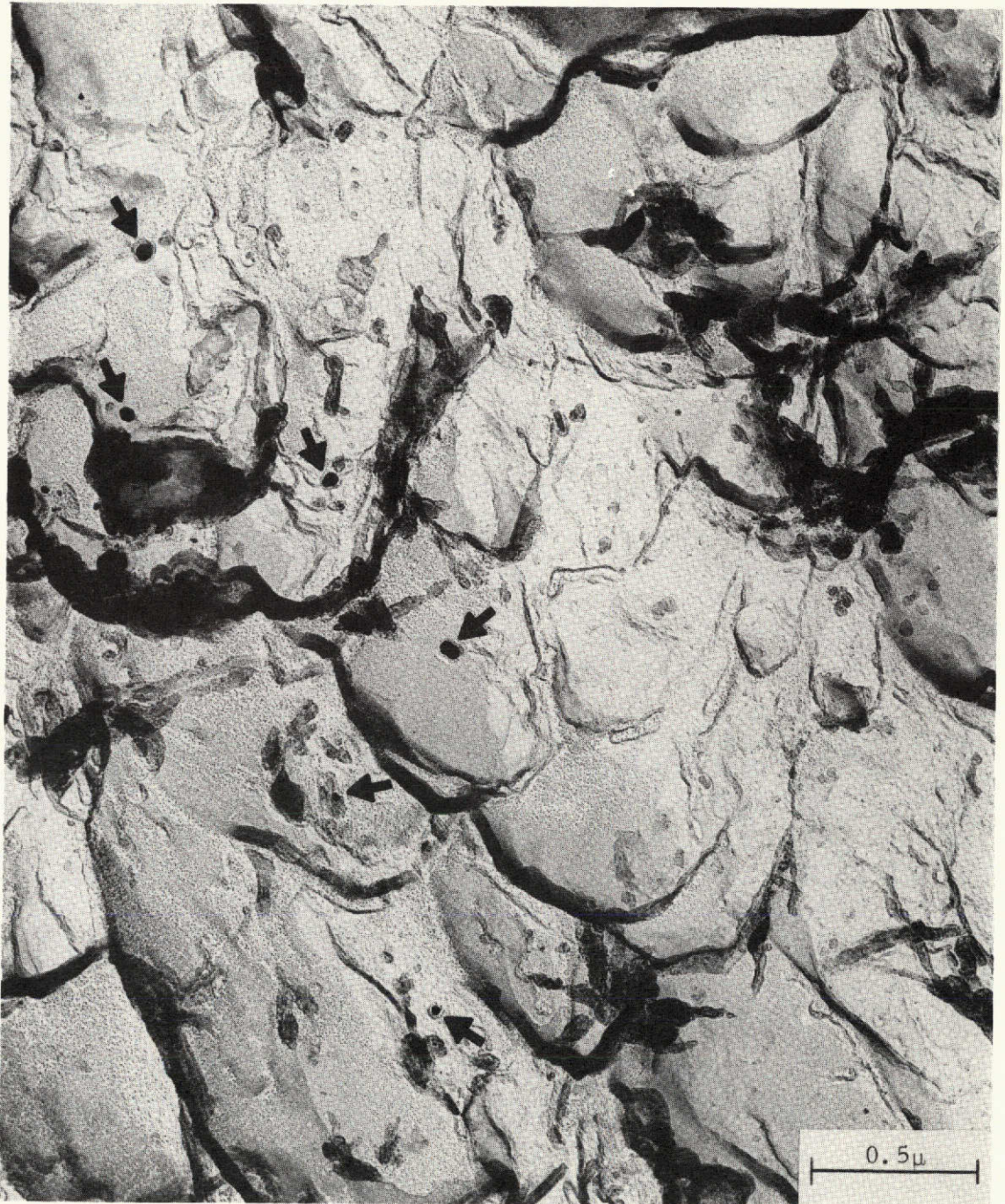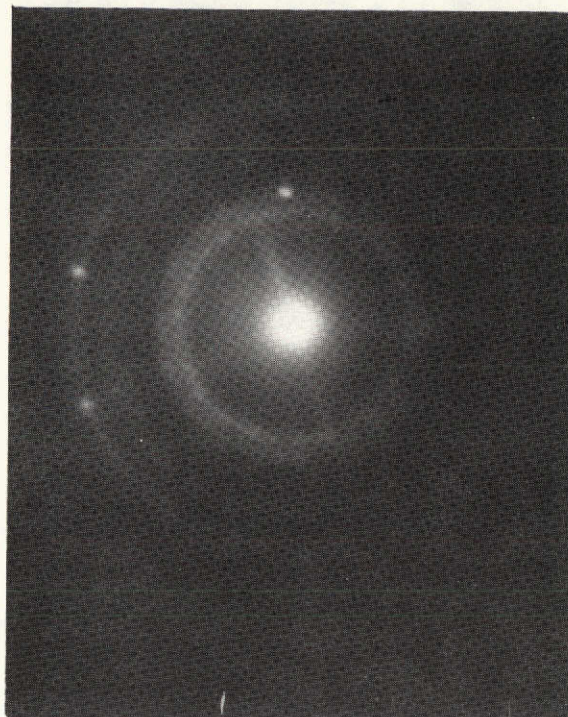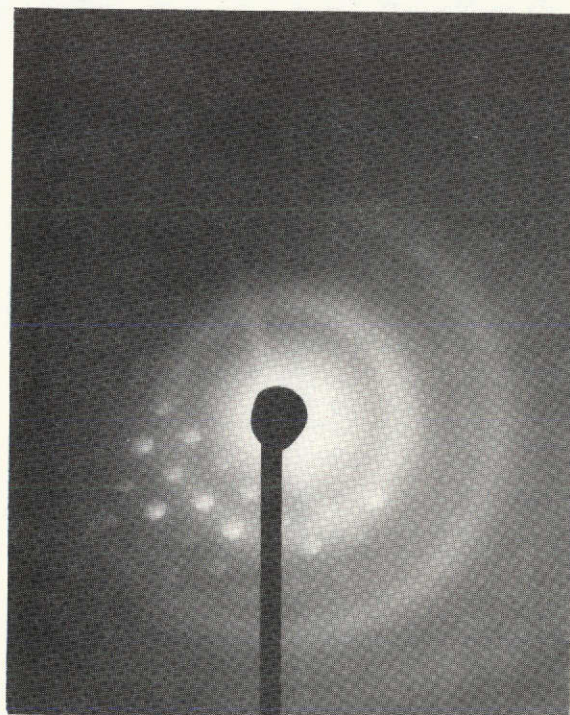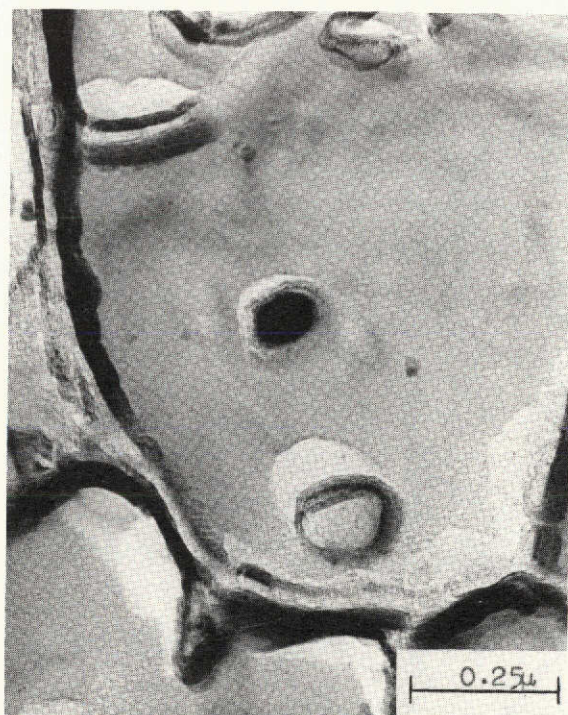
Figure 24 Extraction Replica from Smooth Tensile Fracture of
Commercial AISI 4340 Steel.
(Arrows indicate extracted particles).

Commercial AISI 4340



High Purity AISI 4340

Figure 25  Extracted Particles and Associated Electron Diffraction Patterns from Smooth Tensile Fractures of Commercial and High Purity AISI 4340 Steels

while the discrete spots in the patterns result from diffraction from the

small single crystal particles extracted from the fracture surfaces. This

latter contention was verified using dark field microscopy on all diffracting

particles.

A number of selected area diffraction patterns were taken from

particles from both high-purity and commercial alloys. Based on previous

studies, [83,116] the carbides in these alloys for the particular heat treat-

ment used were thought most probably to be cementite. The calculated lat-

tice spacings of the planes within the extracted particles producing the spot

patterns observed were compared with the reported d spacings of cementite

from previous investigations. [116-118] These results are presented in

Table V. The excellent correlation of the interplanar spacings of the ex-

tracted particles with those of cementite lead to the conclusion that cemen-

tite particles in the AISI 4340 alloys must be the nucleating particles for the

formation of the small dimples on the fracture surfaces of these alloys.

F. Fracture Profiles

To investigate further the fracture surface features of these alloys,

fractured tensile halves (both notched and smooth specimens) were nickel

plated, sectioned longitudinally and polished to the mid-plane. Examination

of the fracture profiles both etched and unetched by optical microscopy re-

vealed little concerning the fracture paths in the various alloys. Occasion-

ally, an inclusion was found on the fracture surface associated with the

cross-section of a large dimple, as is illustrated in Figure 26a. In the

TABLE V

## Observed d Spacings from Selected Area
## Diffraction Patterns of Extracted Particles

| Observed d Values (Å) | Previously Reported d Values (Å) for Cementite | | hkl |
| --- | --- | --- | --- |
| | (117) X-Ray | (116,118) Electron Diffraction | |
| 1.03 | 1.026 | 1.03 | 135 |
| 1.12 | 1.123 | 1.12, 1.13 | 323 |
| 1.34 | 1.339 | - | 124 |
| 1.52 | 1.506 | 1.51 | 222 |
| 1.60 | 1.582 | 1.59 | 123 |
| 1.68 | 1.679 | 1.67 | 220 |
| 1.86 | 1.862 | 1.87, 1.84 | 202 |
| 1.97 | 1.968 | 1.96 | 211 |
| 2.09 | 2.098 | - | 121 |
| 2.23 | 2.207 | - | 120 |
| 2.55 | 2.536 | 2.54 | 020 |
| 2.79 | - | 2.79 | - |
| 3.35 | 3.358 | - | 110 |
| 3.72 | 3.75 | 3.74 | 101 |
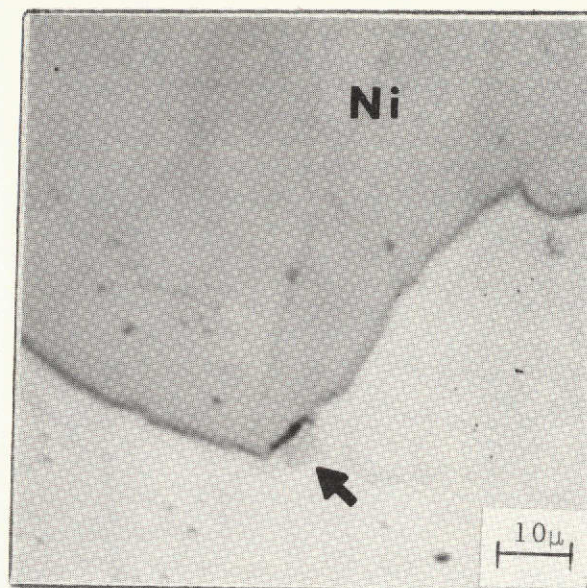
a) Notched Tensile Fracture of High Purity 18 Ni Maraging Steel. (Inclusion indicated by arrow)
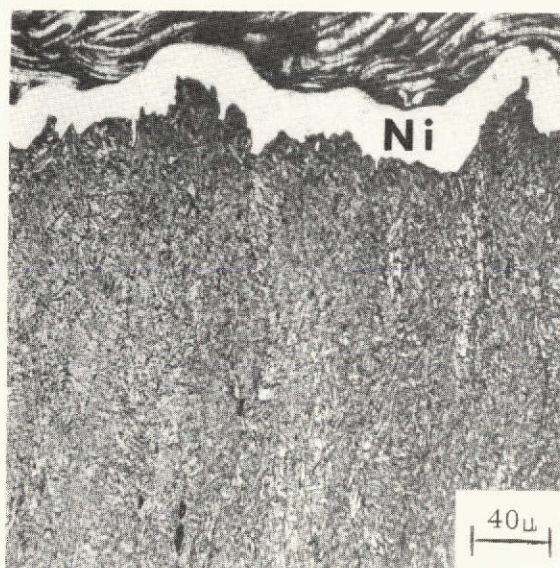
b) Smooth Tensile Fracture of High-Purity AISI 4340.
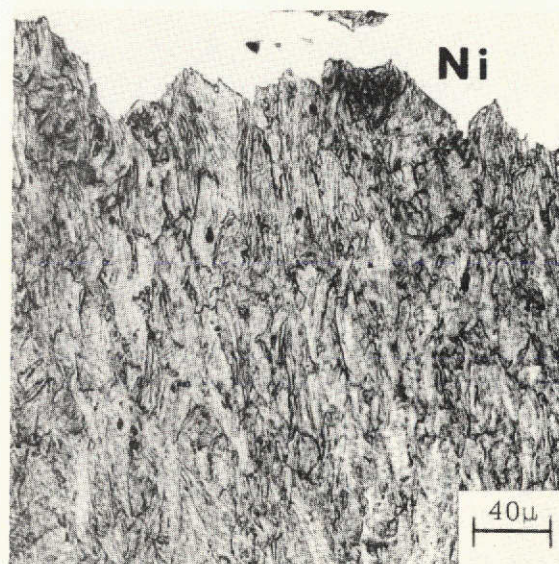
c) Smooth Tensile Fracture of Commercial 18 Ni Maraging Steel.

Figure 26   Optical Micrographs of Profiles of Tension Fractures.

etched condition, the fracture cross-sections showed that the matrix near the fracture surface was severely deformed and generally the flow pattern tended to elongate the structure in the direction of the applied tensile stress, as illustrated in Figure 26b and c.

Two-stage replicas were also taken of the fracture profiles at the mid-thickness of each specimen. Each section was polished and lightly etched before replication to delineate the fracture profile and to provide a means of observing whether or not the fractures tended to follow micro-structural features. Representative micrographs from the two alloy types are presented in Figure 27. Both the high-purity and commercial grade materials for each alloy system exhibited the same fracture profile features, but there is evidence that the fracture path is different in the two alloy systems.

The fracture profile seen in Figure 27a of an AISI 4340 specimen shows the fracture to be quite irregular and to follow the boundaries of the acicular ferritic structure. This observation of the fracture path following the ferrite boundaries is in agreement with the findings of a previous study by Turkalo[119] of fracture in a plain carbon steel, heat treated to produce a quenched and tempered martensitic structure. This fact also correlates with the observation made in Chapter IV, that the carbides tend to precipitate at the martensite lath boundaries; and since it was shown in the preceding section that the small dimples on the AISI 4340 fracture surfaces are nucleated by cementite particles, it is expected that the fracture
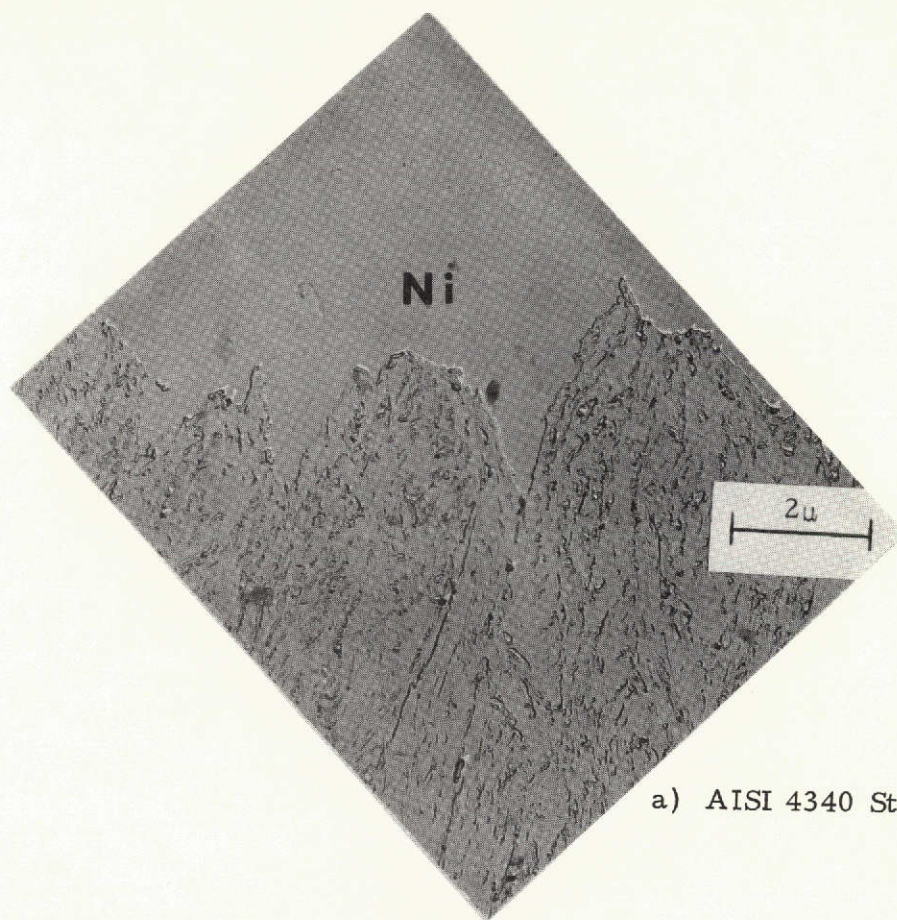
a) AISI 4340 Steel
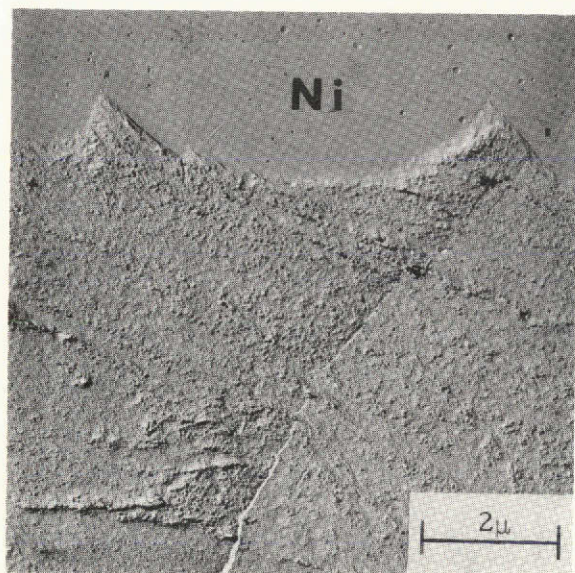
b) 18 Ni Maraging Steel

Figure 27  Transmission Micrographs of Replicas From Profiles of Smooth Tension Fractures.

would generally follow the martensitic boundaries.

In contrast, the fracture profiles of the 18 Ni, 200 grade maraging steels, as shown in Figure 27b, exhibit no apparent preference of the fracture for following particular microstructural features.

CHAPTER VI

DEFINITION OF CRITICAL REGIONS FOR
FRACTURE INVESTIGATION

A.  Metallographic Specimen Preparation

As discussed in the previous chapter, it was observed that for any

one of the four alloys, the fracture features in the region of fast fracture

initiation on $K_{Ic}$ specimens were the same as those from the central regions

of normal rupture on smooth and mildly notched round tensile specimen

fracture surfaces.  These observations lead one to speculate that the mecha-

nisms of plastic fracture are at least qualitatively the same for the three

specimen geometries in these particular alloys.  While precracked fracture

toughness specimens are meant to simulate flawed material in service,

they are expensive to produce, and it is generally quite difficult to arrest

the fracture process once it has begun, especially in high-strength materials.

Thus, it was decided to study the initiation and progression of plastic frac-

ture in smooth and mildly notched round tensile specimens with the belief,

based on the above fractographic observations, that the observed processes

would be comparable to those taking place at the tip of a crack.

The general procedure for the metallographic portion of the investiga-

tion was to load a tensile specimen to some predetermined level of plastic

strain, unload and section the specimen longitudinally, exposing the longitudinal midplane to metallographic examination. One smooth and one notched tensile specimen of each alloy was strained to fracture in order to determine the tensile flow properties of the alloys. (See Chapter IV for the tensile curves, tensile specimen geometries, and orientation.) The fractured tensile halves after metallographic preparation were than used to determine the most advantageous orientation of the midplane for observing voids (either perpendicular to or parallel to the primary rolling direction).

After straining, the necked specimens were prepared for metallography. Based on the observations made on sections of the fractured tensile halves, it was decided to surface grind the necked sections to within 0.075 mm (3 mils) of the mid-point of the minimum diameter of the neck. Experience indicated that using automated polishing equipment the final metallographic polishing would remove approximately 0.075 mm (3 mils) and thus, the above procedure would permit viewing of the longitudinal midplane of each specimen. The grinding was done such that the plane exposed was perpendicular to the primary rolling direction and parallel to the tensile axis. This particular orientation was found to offer the most advantageous view of voids in the AISI 4340 alloys due to the elongation of the sulfides perpendicular to the section plane. Orientation made no difference with the 18 Ni maraging steels, since the carbo-nitride particles had no preferred orientation. The orientation of the tensile specimens during straining and the orientation of the sectioning process are illustrated in
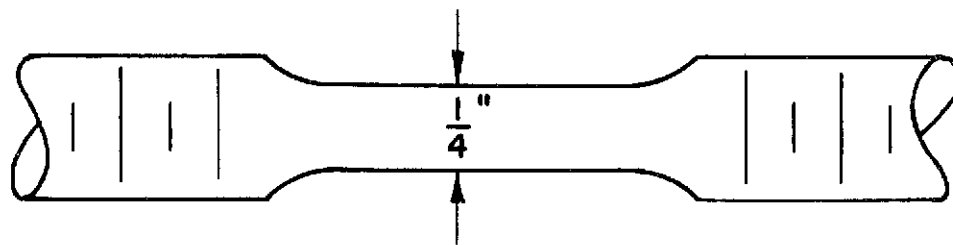
Figure 28.

Once a specimen was surface ground, as illustrated, the neck was

cut from the tensile specimen using an abrasive cut-off wheel and mounted

so as to expose the ground plane. Final polishing was carried out using

automated equipment and 240, 320, 400, and 600 grit silicon carbide abra-

sive papers; 6, 3, and 1 micron diamond paste; and finally a slurry of 0.05

micron alumina powder and distilled water. This procedure, as stated

above, removed 0.075 mm (3 mils) of specimen thus exposing the longitudinal

midplane of the neck. The polishing technique resulted in no noticeable

distortion of voids or any pulling out of inclusions from the matrix. The

specimens were then studied extensively in the unetched condition using
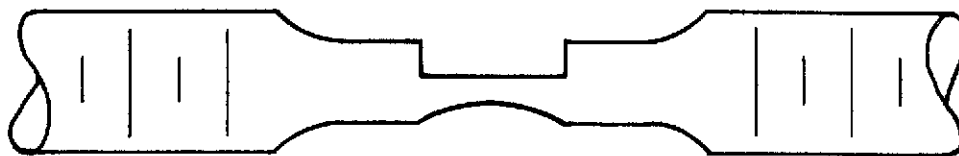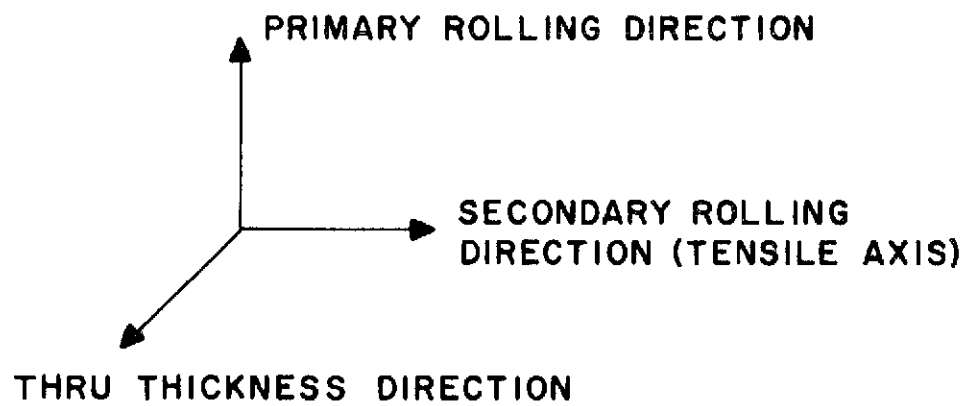
light microscopy.

## B. Areas Investigated

A detailed metallographic investigation was carried out using the

strained and sectioned tensile specimens to describe the processes of

void initiation, growth, and coalescence in these alloys. Since, as shown

by Bridgman (See Chapter IV), the stress state varies with position on the

midplane of the tensile neck, it was decided to arrive at some sort of average

measurements by completely examining predetermined areas in the centers

of the midplanes. To determine the areas from which measurements would

be made, the fractured tensile halves of each alloy, sectioned to expose the

midplanes, were examined.

As is seen in the photomicrographs of the nickel-plated fractured

a) BEFORE TESTING

PRIMARY ROLLING DIRECTION

SECONDARY ROLLING
DIRECTION (TENSILE AXIS)

THRU THICKNESS DIRECTION

b) NECKED SPECIMEN AFTER SURFACE GRINDING

Figure 28 Orientation of Tensile Specimens and Section Plane.

tensile specimens presented in Figures 29-32, the presence of large voids

is not limited to the fracture path, but rather voids extend away from the

fracture surfaces in the direction of the tensile axis. To provide measure-

ments which offer an average of stress conditions found in the neck yet are

pertinent to the fracture process, an area centered on the point of inter-

section of the minimum diameter of the neck and a longitudinal bisector of

the specimen was metallographically examined. The dimensions of the area

varied from alloy to alloy. These dimensions were chosen with reference

to the fractured tensile halves so that the longitudinal dimension of the area

extended to include all voids of substantial size away from the fracture sur-

face, and the transverse dimension of the area was taken as the width of

the area of normal rupture on the fracture surface, i. e., the shear lips are

not included.

As may be seen in the photomicrographs of the fractured tensile

halves (Figures 29-32), the extent of the presence of large voids is greater

for the commercial alloys than for the high-purity alloys. Also, the areas

of voids are more restricted in the longitudinal direction in the notched

specimens than in the smooth. This observation undoubtedly results from

the fact that the presence of the notch concentrates the stress and strain in

a narrow region centered on the notch. These observations are described

quantitatively in Table VI where the exact sizes of the areas examined

(hereafter referred to as critical areas) in each alloy are tabulated. It is

also seen in Table VI that the size of the critical area of major void formation

Smooth Specimen
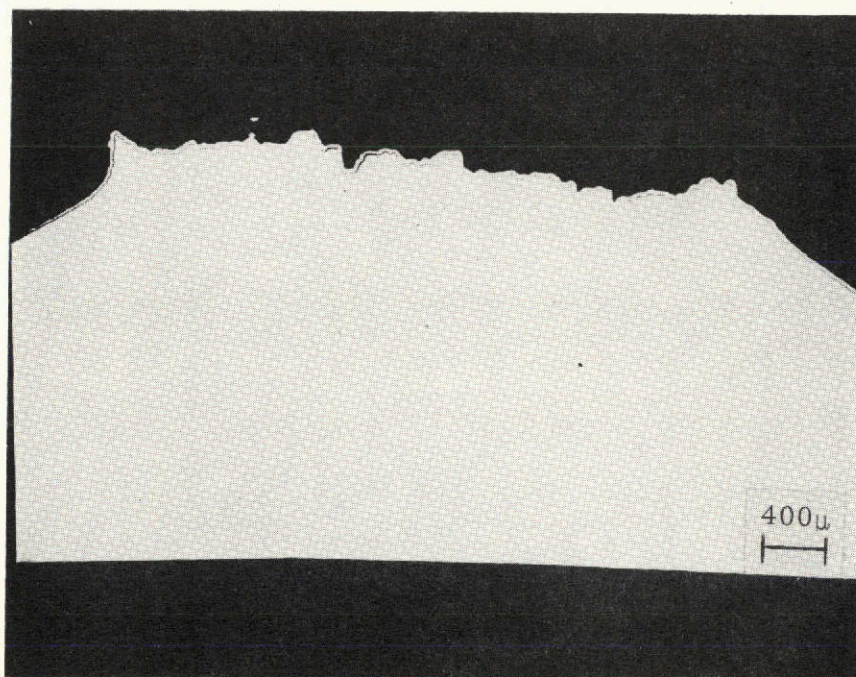


Notched Specimen

Figure 29  Midplanes of Fractured Tensile Specimens of Commercial AISI 4340 Steel.
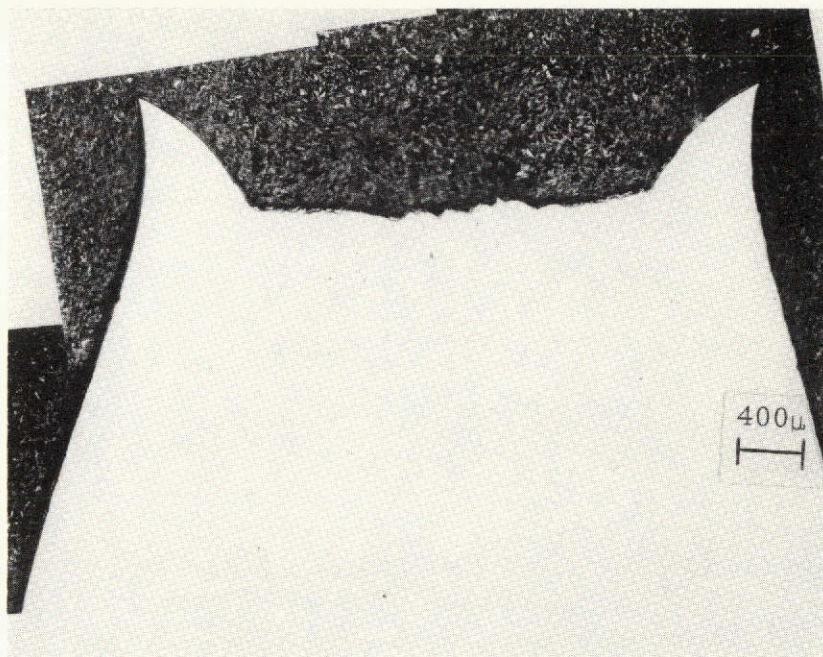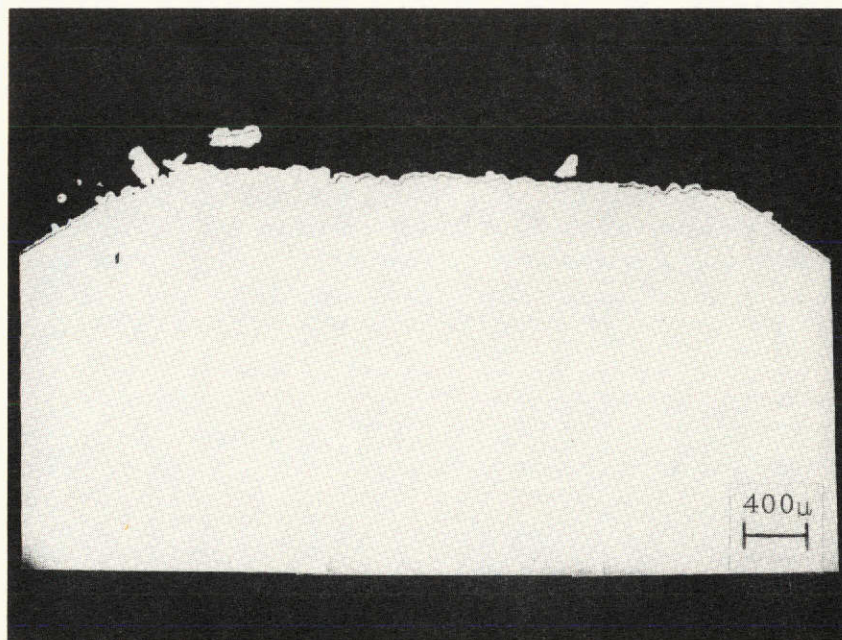
Smooth Specimen



Notched Specimen

Figure 30   Midplanes of Fractured Tensile Specimens of
High-Purity AISI 4340 Steel.
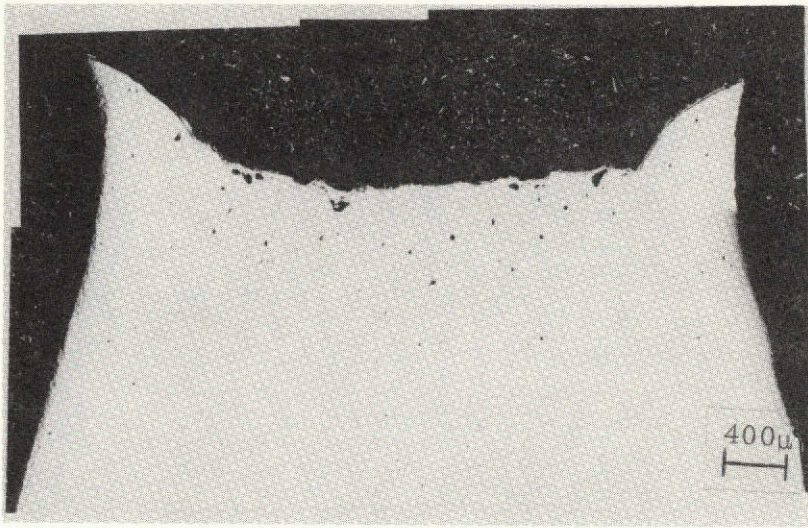
Smooth Specimen
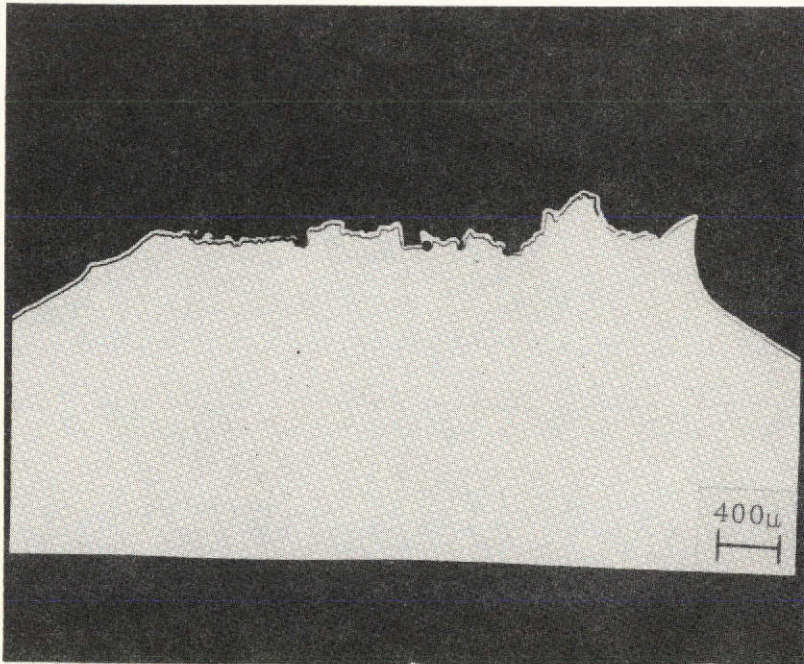


Notched Specimen

Figure 31 Midplanes of Fractured Tensile Specimens of Commercial 18 Ni Maraging Steel.
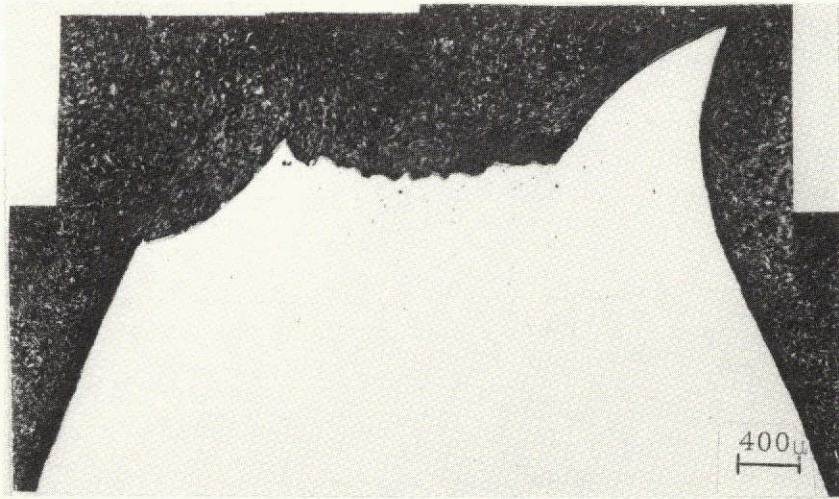
Smooth Specimen
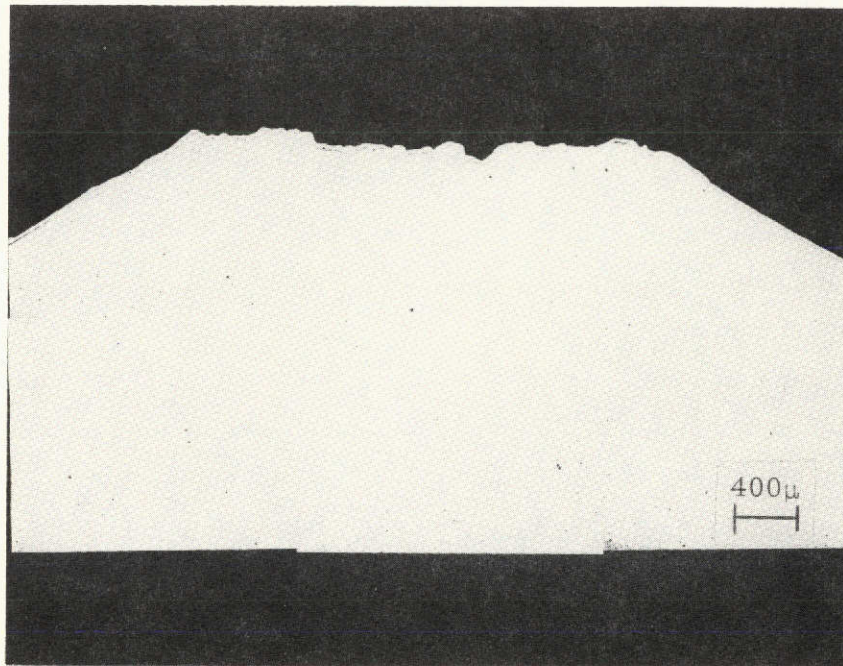


Notched Specimen

Figure 32  Midplanes of Fractured Tensile Specimens of
High-Purity 18 Ni Maraging Steel.

TABLE VI

Dimensions of Critical Areas Metallographically Examined
in Strained Tensile Specimens

| Alloy | Specimen Type | Length (mm) | Width (mm) |
|---|---|---|---|
| Commercial AISI 4340 | Smooth | 2.25 | 3.00 |
| | Notched | 1.35 | 4.40 |
| High-Purity AISI 4340 | Smooth | 2.10 | 2.80 |
| | Notched | 1.20 | 4.20 |
| Commercial 18 Ni | Smooth | 2.15 | 2.60 |
| | Notched | 1.20 | 4.05 |
| High-Purity 18 Ni | Smooth | 1.95 | 2.00 |
| | Notched | 1.05 | 3.80 |

decreases continuously as the level of toughness of the alloys increase; i.e., from the least tough alloy--commercial AISI 4340, to the most tough--high-purity 18 Ni maraging. As will be demonstrated in the following chapters, voids initiate first and grow more rapidly from the largest inclusions. As was shown in Table III, the commercial alloys contain larger inclusions than the high purity alloys which provides an explanation for the observed correlation between the sizes of critical regions and the values of fracture toughness. The tougher alloys contain smaller inclusions and thus experience void nucleation at a later stage and lower rates of void growth than the less tough alloys. Thus the sizes of the critical regions in the tougher alloys are small since void initiation and growth have proceeded slowly and are consequently confined to a narrow region centered on the tensile neck within which the stresses are greatest.

The procedure followed in the metallographic investigation involved viewing each square micron of the predetermined critical area of midplane in a strained and sectioned tensile specimen. The image of an area 0.15 mm x 0.20 mm was projected on a ground glass screen on the metallograph at a magnification of 1000X. Using graduated controls on the specimen stage for specimen translation, this projected microscopic area was made to translate over the entire macroscopic critical areas listed in Table VI. Detailed examination of each microscopic area was then carried out at 1000X.

# CHAPTER VII

## VOID INITIATION

### A. 18 Ni Maraging Steel

As was illustrated in Chapter V, the fracture surfaces of the 18
Ni, 200 grade maraging steels are composed almost entirely of large
dimples. The presence of cleaved carbo-nitride inclusions lying in the
bottoms of the large dimples together with the good correlation between
inclusion spacing in the matrix and dimple spacing on the fracture sur-
faces led to the supposition that the dimples (voids) in the maraging steels
are nucleated by the carbo-nitride inclusions. The metallographic inves-
tigation of the series of strained and sectioned tensile specimens confirms
this hypothesis. In both high-purity and commercial 18 Ni maraging alloys
and for both smooth and notched tensile specimens for which straining was
interrupted before fracture, the cracking of carbo-nitride inclusions was
observed directly as the exclusive origin of voids in these alloys.

Examples of cracked titanium carbo-nitride particles in both high-
purity and commercial grade maraging steels and for both specimen geome-
tries are presented in Figure 33. It was observed generally that the larger
inclusions fractured first, i.e., at lower strains, with the process of
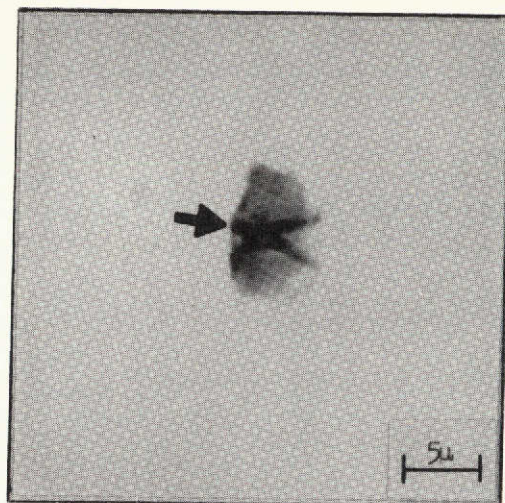
High-Purity, Smooth Specimen
($\epsilon = 0.049$)

Tensile
Axis
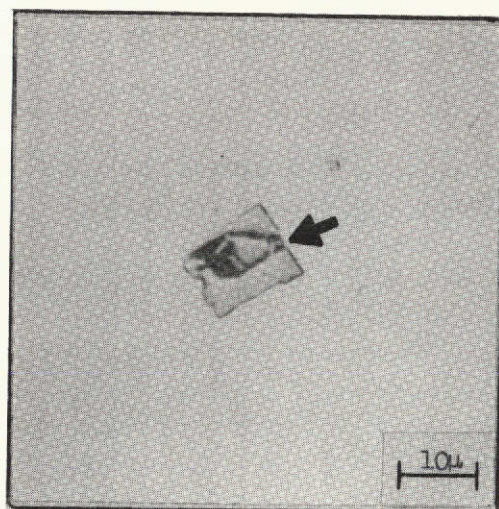


Commercial Purity, Notched Specimen
($\epsilon = 0.082$)

Figure 33   Void Initiation by Fracture of Carbo-Nitride Inclusions in
18 Ni Maraging Steel Strained Plastically   (Arrows
indicate voids)

cracking continuing as the strain increased with smaller and smaller inclusions beginning to fail. Although, as indicated below, some inclusions were fractured before straining, it was the general observation that cracking of the carbo-nitrides occurred after loading the specimens into the plastic region and at stress levels above 200 ksi which correlates well with the results of Floreen and Hayden.[139]

Using the procedure outlined in the previous chapter for scanning the predetermined critical areas (see Table VI) on the midplanes of the strained and sectioned tensile specimens, the void initiation process was studied in these maraging steels. In each microscopic area projected on the metallograph, the number of inclusions present were counted together with the number of voids present and the number of inclusions with associated voids, i.e., cracked inclusions and those associated with well developed voids. These tabulations permitted calculation of the percent of inclusions which have voids associated with them at each level of strain, a quantity which is a measure of the extent of void nucleation.

The results for the percent of inclusions in the maraging steels which had voids associated with them are presented in Figure 34. Each datum point represents observations from at least 127 inclusions. These plots indicate that void initiation is a continuous process with increasing strain. Note that in the commercial grade steel, 19.3 percent of the carbo-nitrides were fractured before any load was applied, i.e., in the as-received condition. The largest inclusions present were generally the ones which were fractured before straining. It appears that if the curves for the commercial alloys
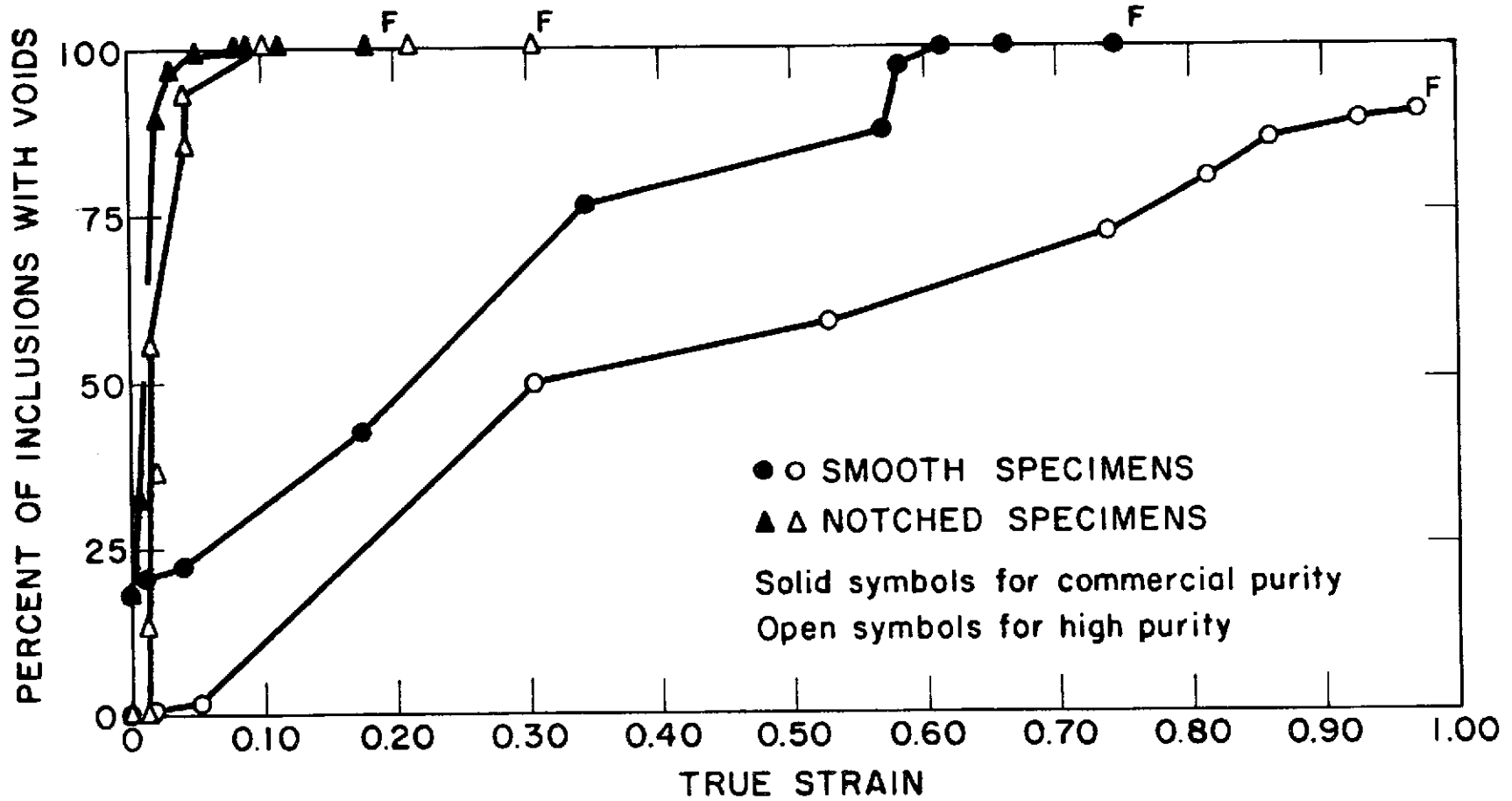
Figure 34  Percent of Inclusions with Voids as a Function of
True Strain for 18 Ni Maraging Steel ("F" indicates
value taken from fractured specimen).

were to be shifted to the right by the amount of strain required for 19 per-

cent of the inclusions to be fractured in the high-purity alloys, that the

curves for commercial and high-purity alloys would coincide. This sug-

gests that the distribution of inclusion sizes for the commercial and high-

purity alloys are similar in the size range in which the majority of the par-

ticles lie. The typical frequency distribution curve for sizes in particulate

systems has its maximum peak skewed toward the smaller sizes and the

mean size lies to the high value side of the peak.[120] Thus it is possible

for the inclusion size frequency distributions of the commercial and high-

purity maraging alloys to roughly coincide over the middle size range even

though the means of the two distributions are substantially different. It

was observed in the smooth specimens of the high-purity alloy that the

smallest inclusions, approximately one micron in size, did not crack even

at the fracture strain. Also, as seen in Figure 34, the rate of void initiation

(based on strain) was much greater for the notched specimens.

Careful tabulation of the locations of void nucleating inclusions in

both smooth and notched tensile specimens indicated that there is no apparent

dependence of void initiation on position within the critical region for the

smooth tensile necks, but that there is for the notched specimens. A demon-

stration of this observation is presented in Figure 35 where the percent of

inclusions with voids within the critical regions are recorded at various dis-

tances from the longitudinal center line of the strained specimens. Figure

35 shows data for notched and smooth specimens for various levels of strain

a) SMOOTH SPECIMEN, $\epsilon$ = 0.176

b) SMOOTH SPECIMEN, $\epsilon$ = 0.568

c) NOTCHED SPECIMEN, $\epsilon$ = 0.024
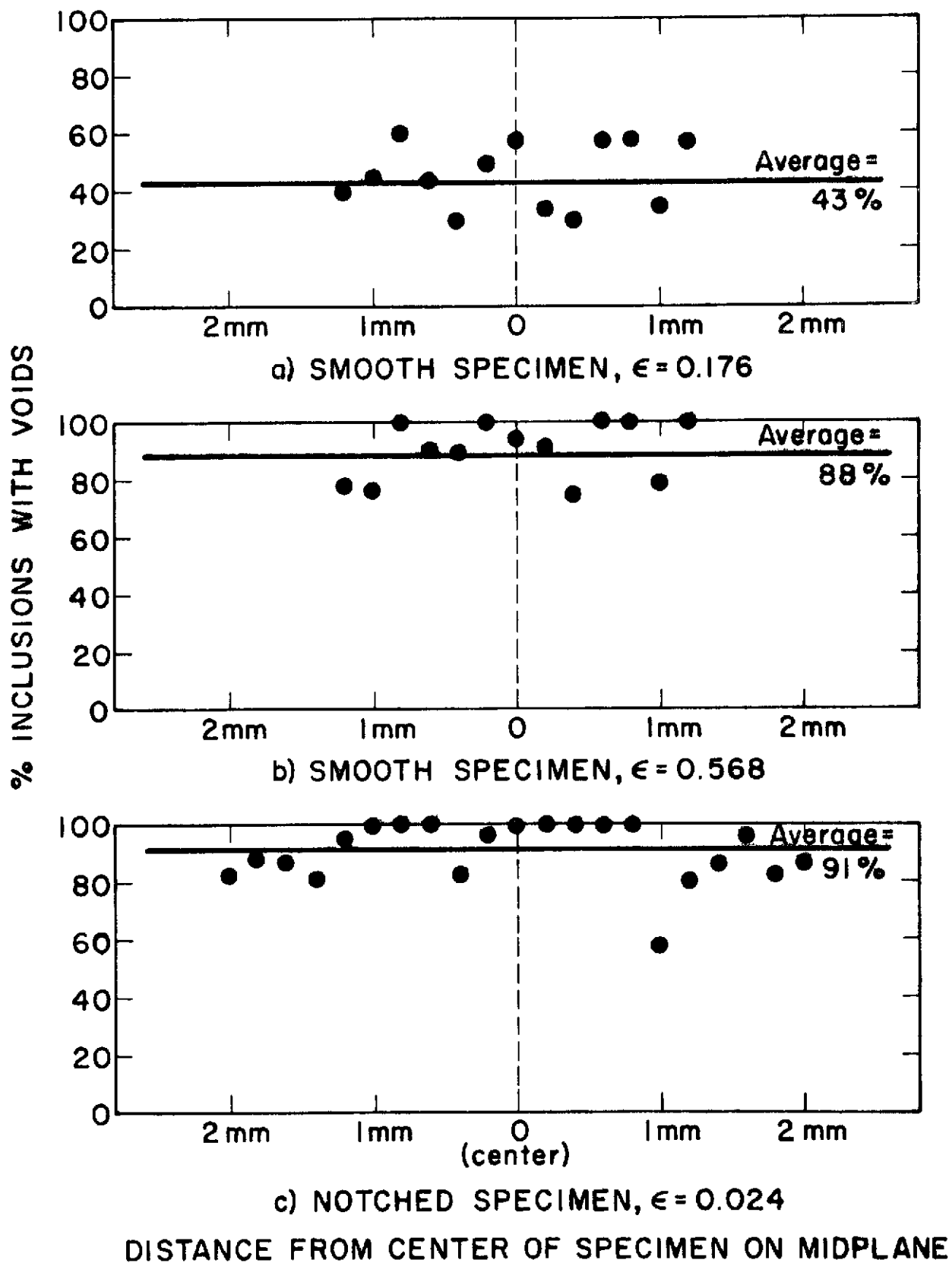
DISTANCE FROM CENTER OF SPECIMEN ON MIDPLANE

Figure 35  Dependence of Void Nucleation on Location in Tensile
Neck for Commercial 18 Ni Maraging Steel.

for the commercial alloy. The same observation was made for the high-purity alloy. As shown by the Bridgman analysis (see Chapter IV), the longitudinal stress and the off-axis principal stresses (the level of tri-axiality) vary with position across the diameter of the neck. For example, for the stress and strain conditions within the smooth specimen represented in Figure 35a, the longitudinal stress varies across the minimum diameter from 237 ksi at the midpoint to 232 ksi at the edges of the critical region being studied. At the same time, the lateral stresses vary from 19 ksi at the mid-point to 14 ksi at the outer edges of the critical region. With this small variation in stress, it is not too surprising that the initiation process exhibits no effects of location in the neck. Likewise, in the smooth speci-men presented in Figure 35b, the variation in stresses is again rather small and the percent of cracked inclusions shows no dependence on position. However, in the notched specimens, as in Figure 35c, the variation of the stresses across the neck is significant. For the notched specimen presented in 35c, the longitudinal stress varied from 314 ksi at the mid-point to 253 ksi at the edges of the critical region, while at the same time the lateral stresses varied from 111 ksi to 50 ksi from center to edge. With this varia-tion in stresses, the void initiation process seems to be favored at the cen-ter of the specimen. This behavior could be due to either the higher longi-tudinal stress or the higher degree of triaxiality at the center of the speci-men.

Since the notched specimens were tested with the purpose of being

able to study the effects of triaxial tension by comparison with the smooth

specimens, Figure 36 presents the percent of inclusions with voids plotted

against the average applied tensile stress for both types of specimens. As

is seen in the figure, the data for both specimen geometries in each alloy

fall on the same curve. This represents a very convincing reason for con-

cluding that the level of triaxial tension plays little or no role in the void

initiation process in the maraging alloys. For any given average applied

tensile stress in these alloys, the level of triaxial tension varies substantially

with the specimen type. To illustrate this point, it is useful to compare the

stress conditions in the two specimens presented in Figure 36b and c. For

the smooth specimen of Figure 36b, the average applied tensile stress is

256 ksi. The local longitudinal stress varies from 271 ksi to 266 ksi from

center to edge of the critical region while the lateral stresses vary from

35 ksi to 30 ksi. The notched tensile specimen presented in Figure 36c

had an average applied tensile stress of 265 ksi and, as pointed out above,

longitudinal stresses which varied from 314 ksi to 253 ksi while the tri-

axiality (lateral stresses) varied from 111 ksi to 50 ksi. Thus, for average

longitudinal stresses within 10 ksi of each other, the level of triaxiality,

i.e., the lateral stresses, varied by as much as 80 ksi. The difference of

3% cracked inclusions (88% for smooth and 91% for notched) is undoubtedly

the result of the added 9 ksi applied tensile stress in the notched specimen

rather than the much greater difference in level of triaxiality.

The correspondence of the notched and smooth tensile data, shown

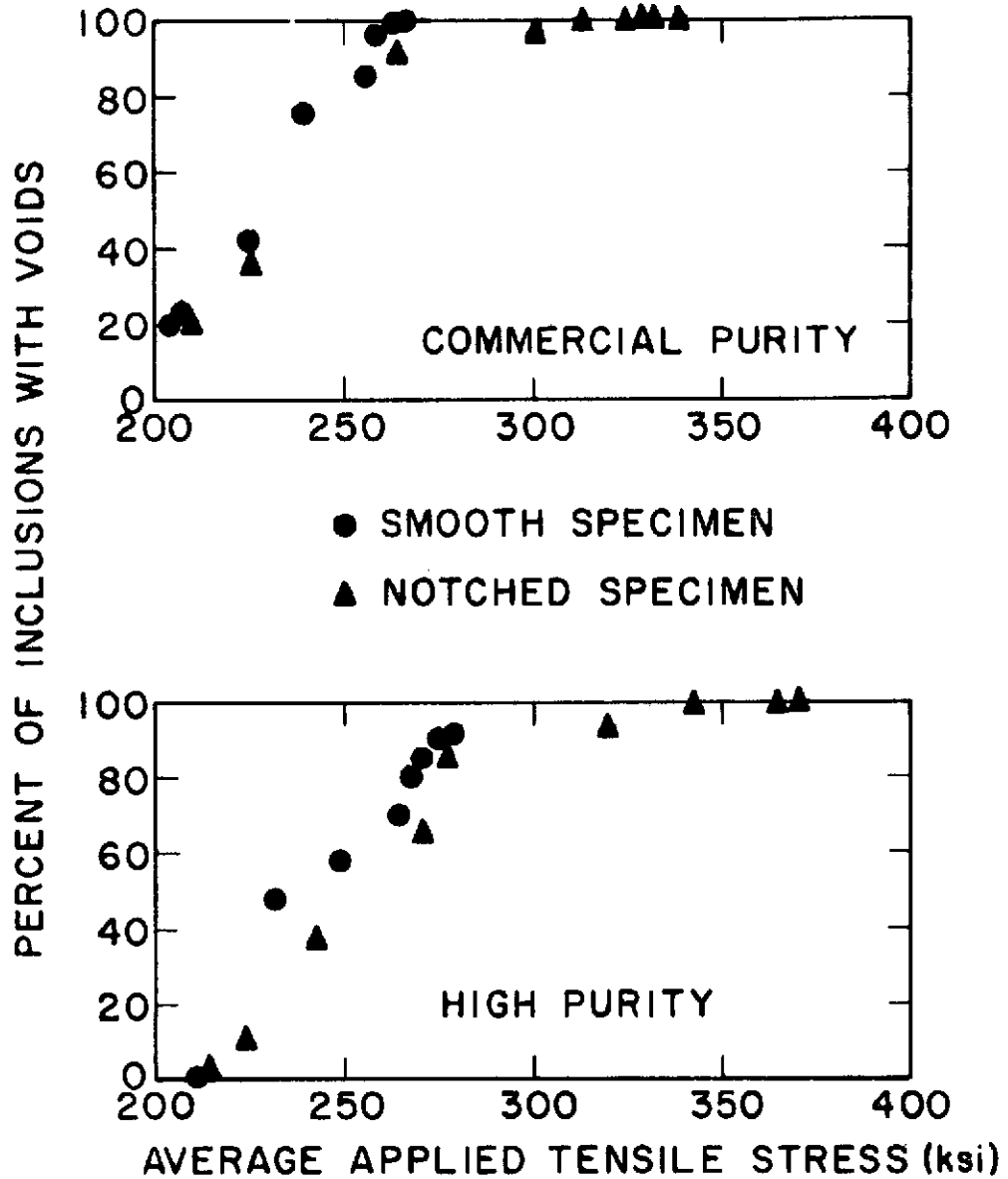in Figure 36, also indicates that the initiation of voids in the maraging steels

Figure 36   Percent of Inclusions with Voids as a Function of
Applied Tensile Stress for 18 Ni Maraging Steel.

does not depend upon the flow stress of the matrix, i. e. , the amount of

plastic deformation in the matrix (strain). As may be seen in the tensile

flow curves presented in Chapter IV, for any given applied tensile stress,

the flow stress of the matrix (related to the resolved shear stresses) is

substantially less in the notched specimens as compared with the smooth.

The fact that the initiation depends upon the applied normal stress is not

surprising since it has been noted above that the carbo-nitrides fail by

cleavage (see Chapter V), a fracture mode which obeys a normal stress

criterion.

The fact that the carbo-nitrides fail by cleavage indicates that they

are brittle and this property provides a basis for an explanation of the ob-

served fact that the larger inclusions fail at lower strains (applied stress).

As first developed by Weibull[121] and more recently discussed by others[122-

124] the fracture strengths of brittle solids depend upon the size of the solid

being loaded. Simply put, the argument is that the greater the volume of

brittle material, the greater is the probability of finding larger size flaws

in the structure which lead to fracture at lower stresses. Although it is

impossible to quantitatively apply the statistical approach to the fracture

strengths of the carbo-nitride inclusions in the maraging steels for lack of

sufficient data, the Weibull theory does qualitatively predict that the larger

the inclusion, the lower the stress at which it will fail.

To further demonstrate that the titanium carbo-nitrides were indeed

brittle, a series of microhardness tests were performed using a Tukon tester

with a 136° diamond pyramid indentor and a 5-gram load. Examples of

representative indentations are presented in Figure 37, and it is seen

qualitatively in the photomicrograph of Figure 37a that the hardness of the

inclusion is greater than the matrix. Uncorrected DPH hardness numbers

averaged $1508 \pm 210$ for the inclusions and $454 \pm 36$ for the matrix. Fur-

ther proof of the very brittle nature of the carbo-nitrides is provided in

Figure 37b. The missing fragment of the inclusion (marked by the arrow)

was dislodged during the indentation process as the inclusion shattered.

Thus, we are justified in using the Weibull argument qualitatively since

the carbo-nitride inclusions are quite brittle.

In an attempt to treat the nucleation problem more quantitatively,

the process was considered from the standpoint of the balance of energy

during the fracturing of inclusions. It is assumed that the necessary con-

dition for fracture of an inclusion is that the elastic strain energy $(U_e)$

stored in the inclusion and released when the inclusion fractures is suffi-

ciently large to provide the energy $(U_s)$ required to create the newly formed

crack surfaces:

$$U_e \geq U_s \, .\qquad\qquad\text{[VII-1]}$$

This treatment seems reasonable since, as demonstrated above, the par-

ticle is extremely brittle and much stronger than the matrix, indicating

that little or no plastic flow of the inclusion should occur during deformation.

If it is further assumed that the elastic stress field of the inclusion

has the same dimensions as the inclusion itself and that the size of the

crack to form is equal to the dimension of the inclusion (demonstrated in

Figure 33 above), then for cracking to occur:
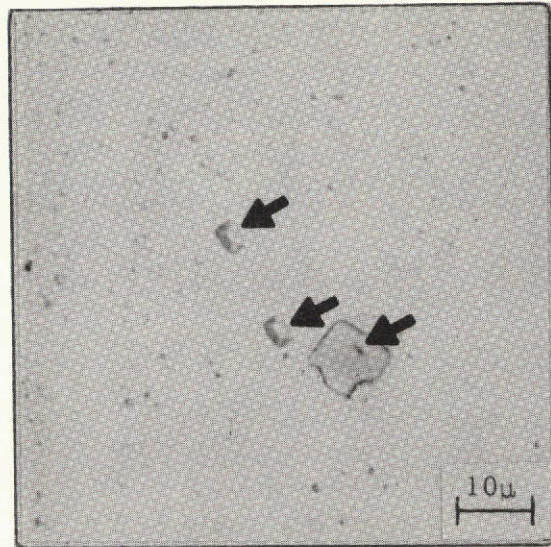
a) Hardness Indentations in matrix and inclusion (Indentations indicated by arrows).
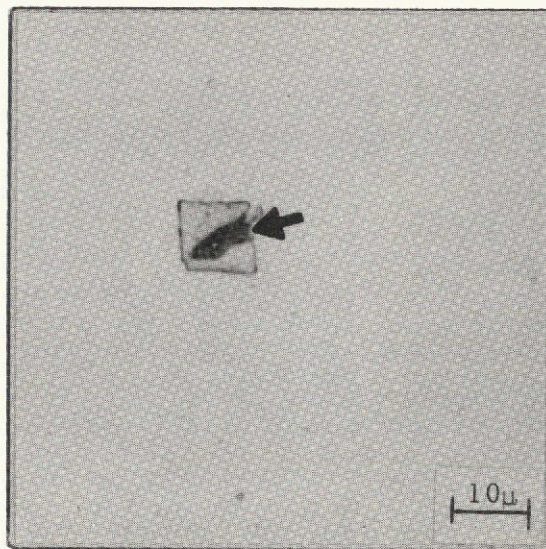


b) Inclusion Shattered by Indentation (Missing fragment indicated by arrow).

Figure 37  Microhardness Indentations in Commercial 18 Ni Maraging Steel.

$$\frac{1}{2} q \sigma \epsilon V_I \geq \gamma A_c \qquad\qquad \text{[VII-2]}$$

where $\sigma$ is the applied normal stress; q is the average stress concentration factor at the inclusion; $\epsilon$ the strain; $\gamma$ the surface energy of the inclusion; and $V_I$ and $A_c$ the volume of the inclusion and area of the newly created crack surfaces, respectively. This condition for a titanium carbo-nitride of side a becomes:

$$\frac{1}{2} q \sigma \epsilon a^3 \geq \gamma (2a^2). \qquad\qquad \text{[VII-3]}$$

Because the inclusion is assumed to deform only elastically, use of Hooke's Law provides that Equation [VII-3] becomes:

$$\frac{q^2 \sigma^2 a^3}{2E} \geq 2 \gamma a^2 \qquad\qquad \text{[VII-4]}$$

or the minimum applied tensile stress to cause cracking is given by:

$$\sigma = \left(\frac{\gamma E}{a}\right)^{1/2} \qquad\qquad \text{[VII-5]}$$

where it has been assumed that $q \approx 2$ after Gurland and Plateau[41] for hard inclusions in a plastic matrix.

Equation [VII-5] predicts that as the size of carbo-nitride inclusion increases, the stress to cause fracture decreases, as observed experimentally. To provide a check on the above treatment, use was made of the initiation data. As mentioned above, the size distribution of particulate systems is generally log normal with the mean lying to the right (large size) of the maximum frequency. Based on this knowledge, it was assumed for the maraging alloys that the average size inclusion in the distribution fractures at the applied stress where 30% of the inclusions are fractured. Using the observed

stresses and average inclusion sizes, a least squares fit of $\sigma$ versus $\left(\frac{1}{a}\right)^{1/2}$ for the maraging steels was determined and is shown in Figure 38. Although the data is sparse, a determination of the slope was made. Realizing that the slope is given by $(\gamma E)^{1/2}$ and using the reported value of E for titanium nitride[125] of $3.9 \times 10^{12}$ dynes/cm$^2$ then $\gamma$ was found to be $1150 \pm 800$ ergs/cm$^2$. This value corresponds reasonably well with those reported in the literature for titanium carbide. Rhee[126] reports a value of $1242 \pm 158$ ergs/cm$^2$ at room temperature and Livey and Murray[127] report a value of $1190 \pm 350$ ergs/cm$^2$ at 1100° C.

The maximum tensile stress applied to these alloys without all of the inclusions failing was for the smooth specimens of the high-purity alloy. At the fracture stress ($1.94 \times 10^{10}$ dynes/cm$^2$), only those inclusions approximately one micron and smaller in size were left uncracked. The above energy approach to the fracture process predicts that at an applied tensile stress of $1.94 \times 10^{10}$ dynes/cm$^2$, particles 0.83 microns on edge will crack. This result is considered to be in reasonably good agreement with the experimental observation and together with the above correlation of predicted surface energy with experiment provide confidence in the strain energy release analysis of the nucleation of voids by fracturing of the carbo-nitride inclusions.

One other point should be considered before turning to the AISI 4340 alloys. It was observed and shown in Figure 34 that in the commercial purity maraging alloy, 19 percent of the inclusions (the largest ones) were
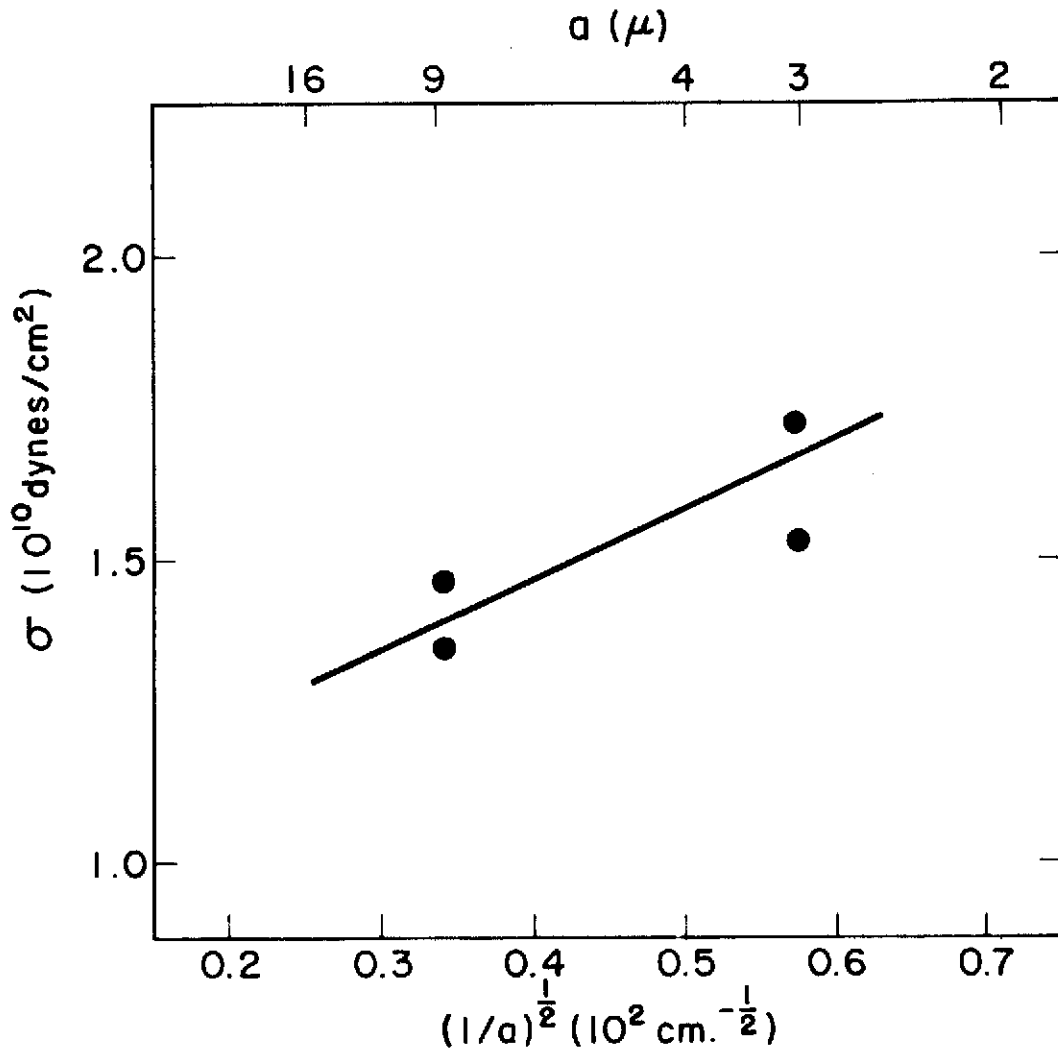
Figure 38   Inclusion Fracture Stress versus Inclusion Size
for 18 Ni Maraging Steel.

fractured in the as-received plate. It seems reasonable that the brittle in-

clusions can be broken during processing of the plate. Unpublished work

by Aquirre[128] indicates that titanium nitrides are cracked and shattered

during splat cooling, due either to differences in thermal contraction of

the inclusions and matrix or to the mechanical work introduced by the par-

ticular cooling technique used. Obviously, the presence of fractured in-

clusions is detrimental to the fracture resistance of these alloys. Thus,

it is advantageous to reduce the sizes of inclusions present in the alloy to

prevent fracture of the carbo-nitrides during fabrication and because dur-

ing subsequent deformation as in service it has been observed that the larger

inclusions nucleate voids at lower strains.

## B.  AISI 4340 Steel

In Chapter V it was shown that the fracture surfaces of the AISI 4340

alloys are covered by two populations of dimples. Good correlation between

the spacings of manganese sulfide inclusions in the matrix and dimple

spacings on the fracture surfaces together with limited examples of charac-

teristic inclusion impressions in the dimples led to the supposition that the

large dimples on the fracture surfaces of the AISI 4340 were nucleated by

manganese sulfide inclusions. The results of the metallographic study of

strained and sectioned tensile specimens confirms this hypothesis. It is ob-

served that the large voids are initiated almost exclusively by separation of

the sulfide-matrix interface in both specimen types in the AISI 4340 alloys.

Figure 39 presents examples of void initiation at sulfide inclusions, in both

high-purity and commercial grade AISI 4340 alloys. (The newly initiated
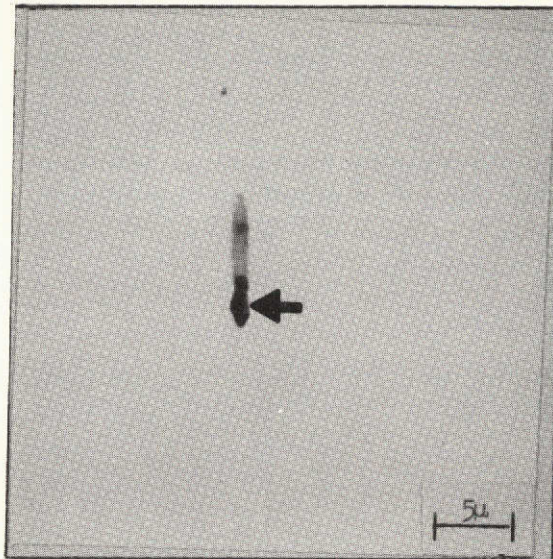
a) High Purity, $\epsilon = 0.057$

Tensile Axis
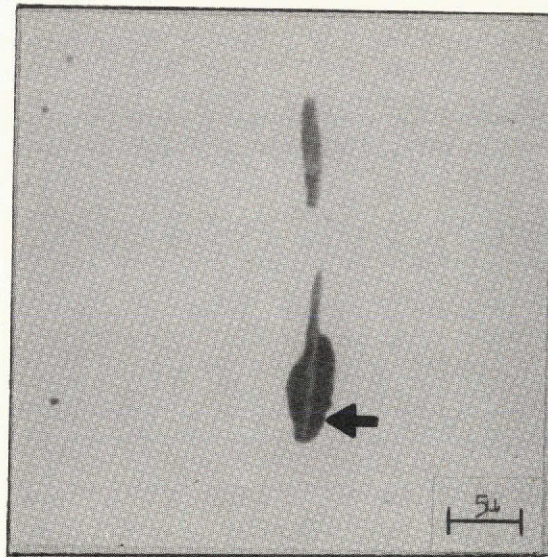


b) Commercial Purity, $\epsilon = 0.018$

Figure 39 Examples of Void Initiation by Interface Separation at the Matrix-Sulfide Interface in AISI 4340 Steel Strained Plastically (Arrows indicate voids)

voids are indicated by arrows. )

Only occasionally were sites other than the sulfide-matrix inter-
face observed to nucleate the large voids in the AISI 4340 alloys. How-
ever, these other nucleation sites (described below) were also always
associated with the sulfide particles. Occasionally with very large sul-
fides containing a large nucleating particle (deoxidation product), voids
were observed to form by fracturing of the sulfide along the boundary be-
tween the sulfide and the interior nucleating particle. An example of this
type of nucleation is presented in Figure 40a. (The white lines within the
void of Figure 40a are metal matrix intersected by the polishing plane,
indicating that the void surface is irregular.) Very long, thin sulfides
oriented along the tensile axis were sometimes found to be fractured across
a minimum section, as illustrated in Figure 40b. Neither of these nucleating
mechanisms was seen often, but rather the predominate mechanism of
sulfide-matrix interface failure provided most of the large void nucleation.

As was observed for the 18 Ni maraging steels, so also did the largest
inclusions nucleate voids first, i. e. , at lower strains, in the AISI 4340
alloys. As straining proceeded, smaller and smaller inclusions would then
begin to nucleate voids so that the nucleation process was continuous as
strain increased with progressively smaller inclusions acting as nucleating
sites for voids. No void initiation at the sulfide-matrix interface was ob-
served unless the matrix had flowed plastically.

While it was previously established (see Chapter V) that the small
dimples on the fracture surfaces of the AISI 4340 steels are nucleated by
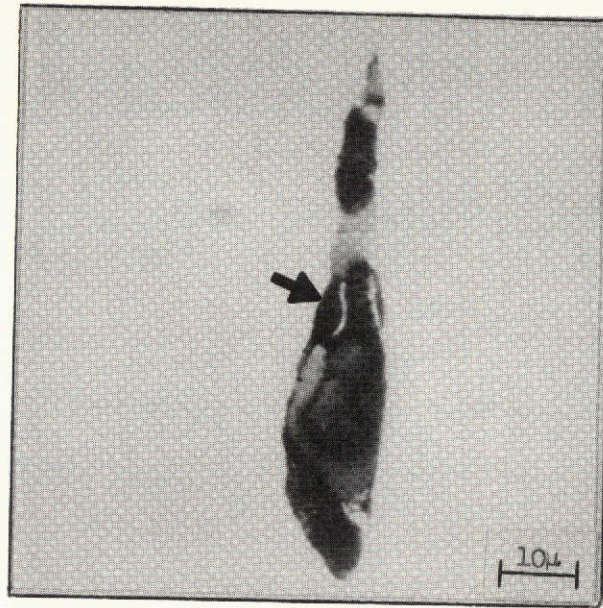
a) Void Initiation by Rupture
   of Sulfide-Nucleating
   Particle Interface,
   $\epsilon = 0.287$

Tensile
Axis
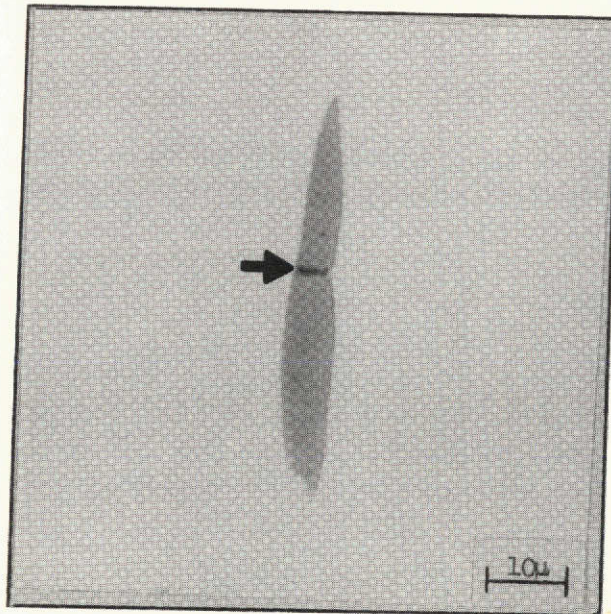


b) Void Initiation by Fracture
   of Sulfide, $\epsilon = 0.042$

Figure 40  Examples of Abnormal Nucleation Sites for Large Voids in
          AISI 4340 Steel Strained Plastically (Voids indicated by
          arrows)

carbide particles, it is of interest to know exactly how the small voids are nucleated, i.e., by interface separation between the carbide and the matrix or by fracture of the carbide? Although the nature of the impressions of the carbide particles on the fracture surfaces point to a mechanism of interface failure since they exhibit no fracture pattern within themselves (see Figure 23), the point is not conclusively decided by fractography.

In order to establish the exact mechanism of void nucleation at the carbides, a series of thin foils were prepared from near the fracture surfaces of broken AISI 4340 tensile specimens. The foils were made by hand grinding on abrasive papers from opposite directions in order to produce sections of the longitudinal midplane, approximately 0.075 mm (3 mils) in thickness. These mechanically produced foils were then electrolytically thinned in a 10% solution of perchloric acid in glacial acetic acid until they were thin enough for electron transmission.

Evidence was found that the small voids in the AISI 4340 steels are nucleated by decohesion of the carbide-matrix interface. Figure 41 presents two observed examples of voids formed by separation of the carbide-matrix interface. The voids are indicated by the arrows and the carbides by the letter "C". Selected area electron diffraction confirmed these particles to be cementite.

The strained and sectioned specimens of AISI 4340 were examined metallographically and the percentage of inclusions with voids in the critical regions were recorded for each strain. The results of this stage of the investigation are presented in Figure 42 with each datum point representing

Figure 41   Void Initiation by Decohesion of Carbide-Matrix Interface in AISI 4340 Steel Strained Plastically (Arrows indicate voids and "C" indicates carbide)
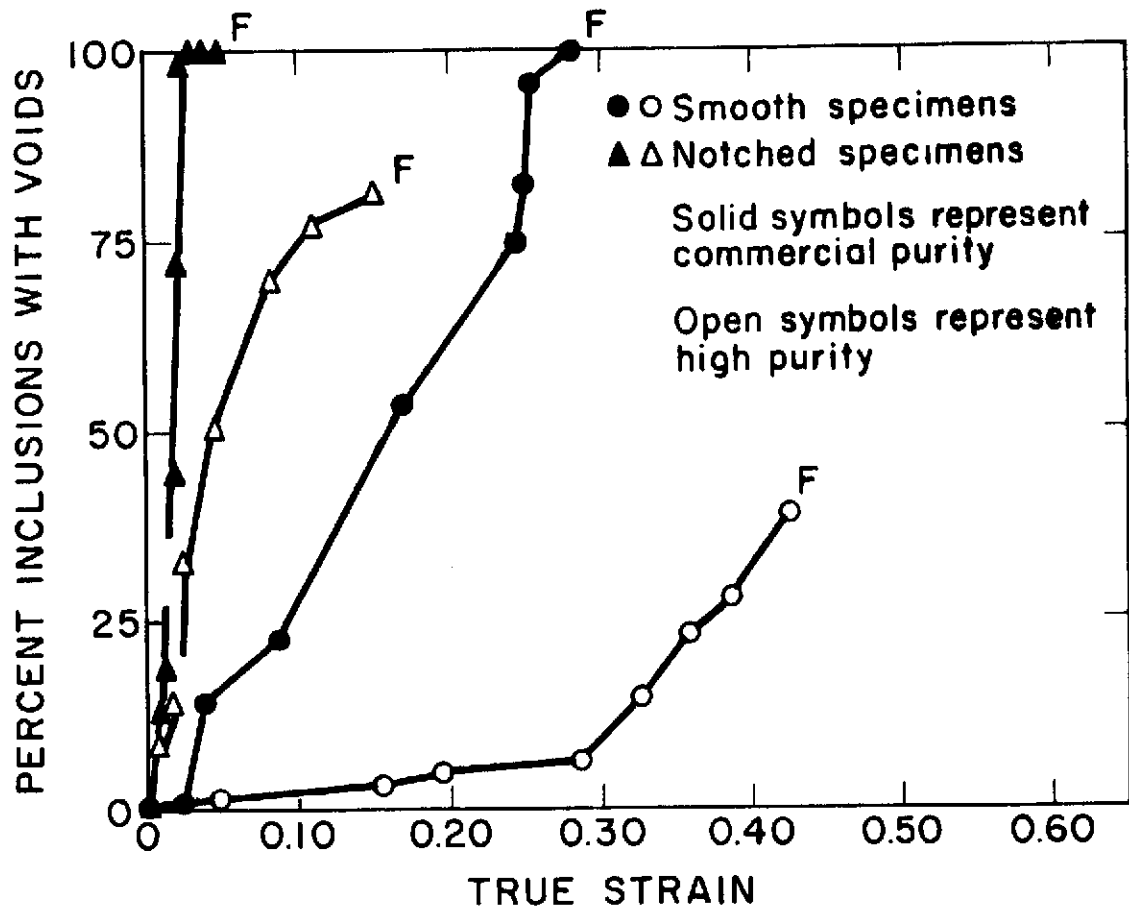
Figure 42   Percent of Inclusions with Voids as a Function of
True Strain for AISI 4340 Steel ("F" indicates
value taken from fractured specimen).

examination of at least 102 inclusions. The plots indicate that the initiation process is continuous as straining proceeds until the specimen fractures or all of the inclusions have nucleated voids. The data shows that in the commercial purity alloy voids are initiated at lower strains than in the high-purity; and the slopes of the plots indicate that the rate of void initiation is greater for the commercial purity AISI 4340, which is probably the result of the larger sizes of inclusions found in the commercial steel. The rates of void nucleation for the notched specimens are much greater than for the smooth, most probably because of the higher stresses involved at a given strain. It was generally observed that not all of the inclusions had nucleated voids in the critical regions of the high-purity alloys with those approximately 2 microns in longest dimension being void-free in the smooth fractured specimen, and those approximately 1 micron in longest dimension being void-free in the notched fracture specimen.

As was seen in the 18 Ni maraging steels and also exhibited in the AISI 4340 alloys, there is no apparent dependence of void initiation on the location within the neck of the smooth round tensile specimens. On the other hand, there is a noticeable tendency for a greater percentage of voids to form in the center of the notched specimens which have been strained appreciably. This behavior may be rationalized as before, namely, the variation in the applied normal stress and level of triaxiality is more severe in the notched specimens permitting some significant variation in nucleation behavior across the neck region.

In an attempt to determine if the observed effect of location within the neck on initiation has any dependence on the level of triaxiality or merely the variation in applied tensile stress in the AISI 4340 alloys, the percent inclusions with voids is plotted against the applied tensile stress in Figure 43. The behavior exhibited in the figure is the same as was observed for the 18 Ni maraging steels. The initiation process seems to be independent of the level of triaxiality and to be most generally dependent upon the level of applied tensile stress.

A series of microhardness tests were performed to determine the relative levels of resistance to deformation of the manganese sulfide inclusions and the matrix and thus provide some basis for understanding the observed void initiation behavior in the AISI 4340 steels. Using a Tukon tester and a 5 gram load, a series of diamond pyramid hardness readings were made; the results of which indicated an uncorrected hardness of the manganese sulfide particles of DPH 182 $\pm$ 17 as compared to 457 $\pm$ 38 for the matrix. The reported values for the sulfide inclusions are not valid since the indentations were generally the same size as the particles. Examples of several microhardness indentations in both inclusions and the matrix are presented in Figure 44. Clearly illustrated is the fact that the manganese sulfide inclusions are softer than the matrix. This observation is in agreement with Chao, et al.[129] who determined the hardness of artificially grown single crysrals of manganese sulfide to be approximately DPH 140. It may also be seen in Figure 44, as indicated by the arrow,
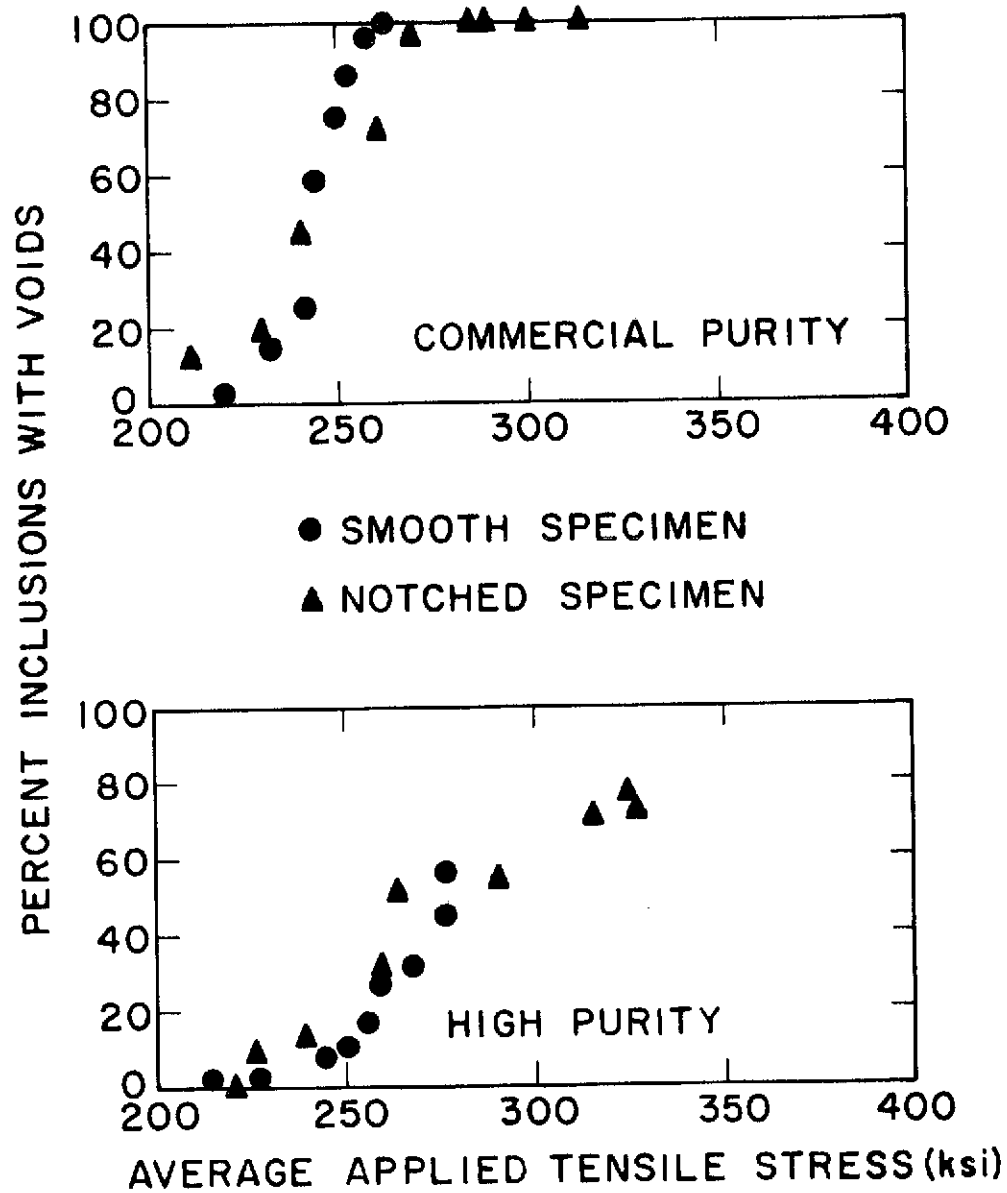
Figure 43  Percent of Inclusions with Voids as a Function of
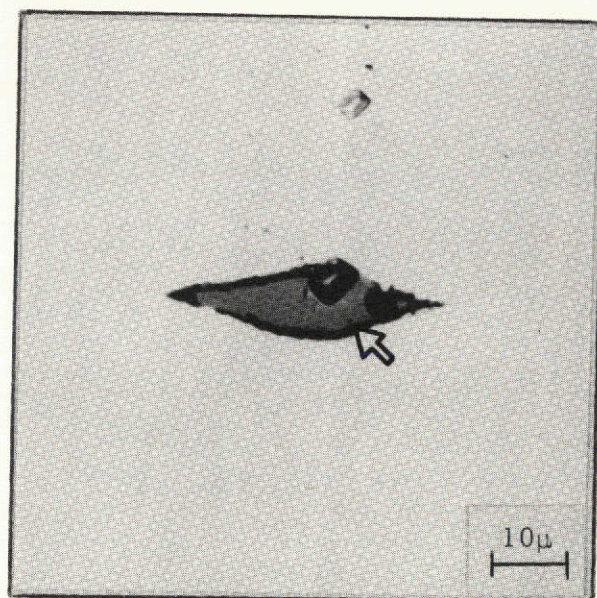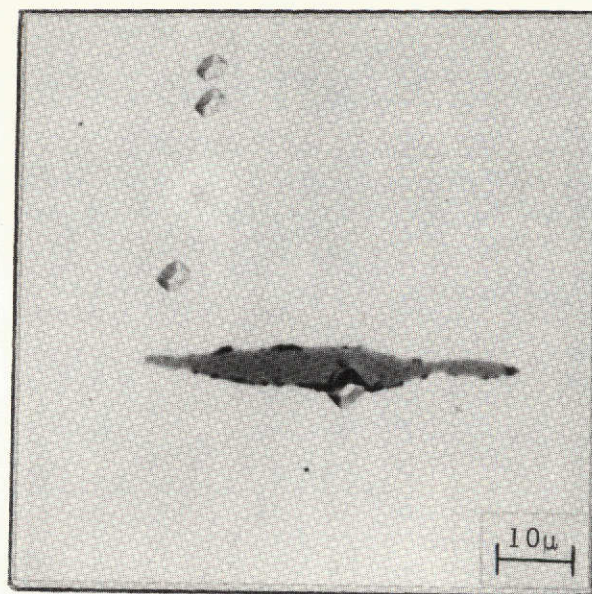Applied Tensile Stress for AISI 4340 Steel.

Figure 44  Microhardness Indentations in Commercial AISI 4340
Steel (Arrow indicates slip line on inclusion surface).

that the hardness indentation of the inclusion in the lower micrograph has resulted in a straight slip line on the free surface of the manganese sulfide particle, an observation that was general for most intented sulfides. Van Vlack, et al. [130,131] report that plastic deformation in manganese sulfide occurs by planar slip which results in straight slip steps on suitably oriented free surfaces.

Several investigations [132,133] of two-phase materials, where the predominate phase is hard and the dispersed phase soft, indicate that slip will be concentrated in the softer phase early in the strain history; but as fracture appraoches, intense deformation occurs in both phases. Chao and Van Vlack [134,135] compressed powder product steel specimens in which inclusions of manganese sulfide were embedded. The relative amount of deformation of the sulfides was measured from the change in shape experienced by the inclusions and from the movement of tungsten markers adjacent to the inclusions. They showed that more deformation occurred in the manganese sulfide particles than in the matrix.

These observations provide a possible explanation for the observed effects of inclusion size on nucleation of the large voids in the AISI 4340 alloys. As the material is loaded, more plastic deformation occurs in the manganese sulfide inclusions than in the matrix. Planar slip provides rather long, narrow slip bands within the inclusions which are blocked at the inclusion-matrix interface resulting in substantial stress concentration across the boundary and resultant fracture there. If the slip bands are

viewed as free slipping cracks, as visualized by Zener,[136] then the local

normal stress at the tip of the band is proportional to the product of the

applied shear stress on the band and the square root of the length of the

band.[136,137] The maximum normal stress acts across a plane oriented

at approximately 70° to the extension of the slip band into the matrix. If

the average length of shear band depends upon the size of the inclusion as

seems reasonable, then this model would predict that the local stress at

the boundary increases with the size of the sulfide and thus the boundaries

at the larger inclusions should fail first as has been observed.

In an attempt to treat more quantitatively the initiation of voids at

manganese sulfide inclusions in the AISI 4340 alloys, it is postulated that

the normal stress ($\sigma_I$) across the inclusion-matrix interface at the poles

along the stress axis (where nucleation is observed to occur) is the sum

of the applied tensile stress ($\sigma_A$) and some plastically induced normal

stress ($\sigma_P$) due to the blocking of slip bands at the interface:

$$\sigma_I = \sigma_A + \sigma_P \ . \qquad\qquad \text{[VII-6]}$$

We can treat $\sigma_P$ as being proportional to the applied shear stress (the

average value of which we will assume is proportional to the flow stress

of the matrix for any given loading conditions) and the square root of the

inclusion radius. (In the following treatment, the radii used will be equi-

valent radii. Since the manganese sulfide inclusions are ellipsoids, we

shall use the radii of spheres of equivalent volume to approximate the inclu-

sion sizes.) We may then represent the stress across the inclusion-matrix

interface by:

$$\sigma_I = \sigma_A + k \, F \, (r)^{1/2} \qquad \qquad [\text{VII-7}]$$

where k is a constant; F the tensile flow stress; and r the equivalent radius

of the inclusion.

Figure 45 is a plot of the observed values of the applied stress at

which voids were nucleated at the average size inclusion (assumed to be

when 30% of inclusions have voids) against the appropriate products of the

observed flow stresses at which nucleation occurred and the equivalent

radii. The intercept of this line with the applied stress axis as determined

by least squares analysis gives the value of the fracture stress of the sulfide-

matrix interface as 340 ± 36 ksi. As a check on this treatment, it is de-

sirable to see if the cut-off sizes for void nucleation observed for the smooth

and notched tests of the high-purity alloy are predicted. If the appropriate

applied fracture stresses and flow stresses (twice the maximum shear

stresses) are used with the slope and intercept of the data in Figure 45,

it is predicted that particles of equivalent radii of 1.3 and 0.4 microns for

smooth and notched specimens, respectively, would just be nucleating voids

at the fracture stresses. These may be compared with the observed values

of 1 and 1/2 micron, respectively. This good agreement provides reason

for accepting the above model to explain the effect of manganese sulfide

size on nucleation of voids in AISI 4340.

One other point should also be addressed. Figure 43 indicates that

the void initiation process is independent of the flow stress since for a

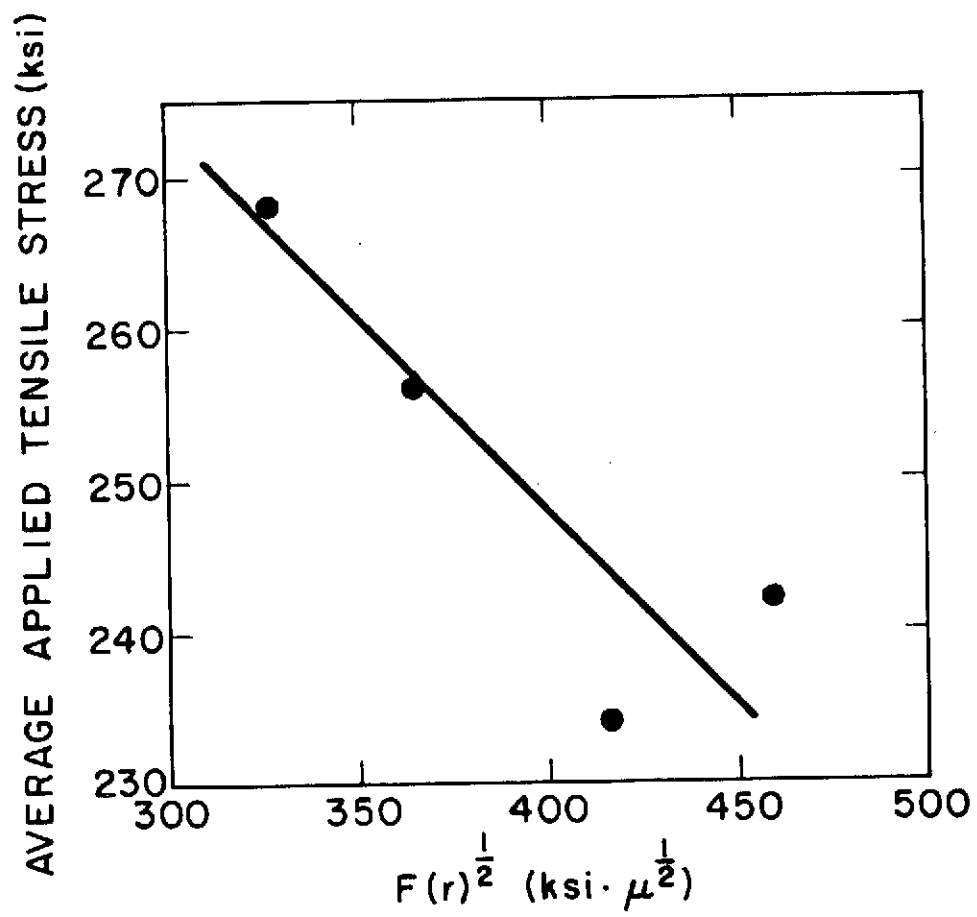given applied tensile stress the accompanying flow stress is substantially

Figure 45  Applied Tensile Stress for Void Nucleation at Sulfides
as a Function of the Product of the Flow Stress and
Square Root of Inclusion Size for AISI 4340 Steel.

different in the notched and smooth specimen types. The apparent disagree-
ment of this observation with the above model which predicts a definite de-
pendence on the flow stress (since it is a measure of the resolved shear
stress on a slip band) can be rationalized by reference to the value of the
fracture strength of the sulfide-matrix interface as determined above. The
value of 340 $\pm$ 36 ksi is not far above the levels of the applied tensile stress,
as seen in Figure 43. Thus, the greatest part of the stress required to
cause interface separation is provided by the applied stress and the slip
induced increment which depends on the flow stress is only a small fraction
of the total required. This small fraction is not large enough to be detected
in Figure 43 where the average stresses are plotted, but none-the-less is
important in causing the largest inclusions to nucleate voids first.

As was shown in Chapter V, the greatest portions of the fracture
surfaces of the AISI 4340 steels are covered by small dimples nucleated on
the cementite particles in the structure. As was seen in Figure 8 and re-
ported elsewhere, [83, 138] the cementite precipitates as needles at the
martensite lath boundaries. Although the evidence shown above indicates
that the carbide-nucleated voids are formed by fracture of the carbide-ma-
trix interface for the AISI 4340, it has generally been reported in the past
that the carbide matrix interface is quite strong and failure usually occurs
by fracturing of the carbide itself. [25, 26, 140-143] All of these past obser-
vations, though, have been made regarding carbide particles of substantially
larger size than those produced by the tempering treatments given the AISI
4340 alloys. There is evidence that the fracture strength of cementite

varies quite drastically with size. McMahon and Cohen[26] have shown

that cementite particles 3 to 10 microns in diameter in an iron matrix have

a fracture strength of approximately $4 \times 10^4$ psi. Webb and Forging[144]

determined the fracture strength of cementite crystals 1 to 2 microns in

diameter to be between 5.7 and $11.6 \times 10^5$ psi. It was determined by study-

ing transmission electron micrographs (as in Figure 8) that the average

size of carbide needle present at the martensite boundaries is approximately

300 Å in diameter and 2000 Å long. With the reduced size of these carbides,

it seems reasonable that their fracture strength could be above the value

reported by Webb and Forging and perhaps exceed the strength of the inter-

face between cementite and the matrix.

Several treatments of void formation due to the pile up of dislocations

at obstacles in the matrix are reported in the literature, including those of

Ashby[45, 46] and Stroh.[47-49] Ashby's treatment requires that the precipi-

tate be encircled by dislocation loops which does not seem applicable to the

cementite needles which lie in the martensitic boundaries because the

boundaries will not permit the movement of dislocations past the precipitate.

All Stroh's model requires is that the dislocations be blocked at some ob-

stacle which is consistant with the situation being considered in the AISI

4340. This treatment indicates that the normal stress developed by the

blocking of arrays of dislocations by an obstacle is proportional to the pro-

duct of the square root of the length of the pile ups, i.e., half the length of

the slip path, the applied shear stress, and to the number of planar pile ups

blocked. In the AISI 4340 alloys, the length of dislocation pile ups in the

matrix would be related to the martensitic grain size while the number of

arrays blocked by the carbide would be related to the length of the carbide.

We could then write an expression for the normal stress developed across

the cementite-matrix interface ($\sigma_I$) based upon the applied stress ($\sigma_A$) and

the stress developed by pile ups of dislocations blocked by the carbide as

due to Stroh:

$$\sigma_I = q\sigma_A + k \, L \, F \qquad\qquad \text{[VII-8]}$$

where q is the average stress concentration factor assumed to be approxi-

mately 2 since the cementite is rigid; k is a constant; L the length of the

carbide; and F the uniaxial flow stress of the alloy which is related to the

average resolved shear stress. It is assumed that the martensite grain

size remains a constant.

Although no exact data are available for the relationship of applied

stress to the onset of void nucleation àt the cementite particles, an approxi-

mation can be made. (Broek[30] has demonstrated the futility of attempting

to investigate void initiation quantitatively for nucleating particles of a size

requiring electron microscopy to view them.) As will be seen in Chapter

IX below, collections of the small carbide-nucleated voids can be seen

optically on the sectioned tensile halves. Using the stresses at which these

arrays become visible, an attempt was made to treat the void nucleation

process at carbide interfaces quantitatively. Figure 46 presents the data

as applied to Equation [VII-8]. The intercept of the line as determined by

least squares analysis represents the fracture strength of the cementite-

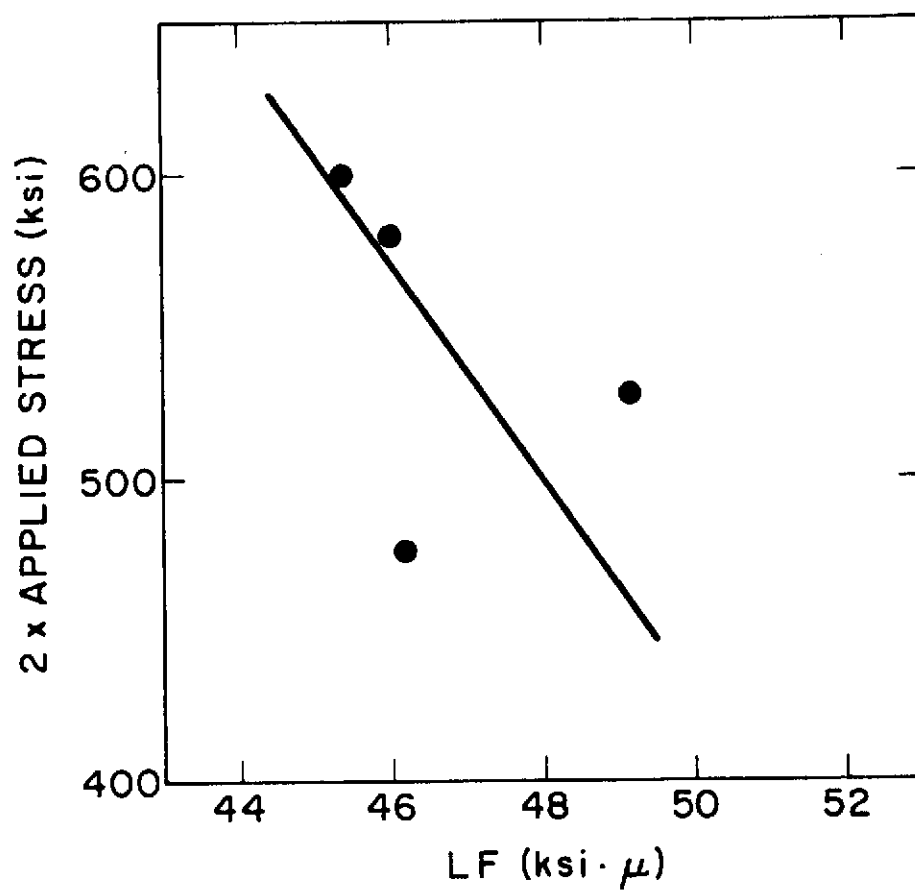matrix interface and was found to be $2.3 \times 10^6 \pm 1.7 \times 10^6$ psi. Although

Figure 46   Twice the Applied Stress for Void Nucleation at
Cementite Particles as a Function of the Product
of the Flow Stress and Carbide Dimension for
AISI 4340 Steel.

this value seems quite high, it should be remembered that it has generally been observed by other investigators that the carbides fracture before the interface. If the reported values for the variation of the strength of cementite crystals with size are extrapolated linearly to include the 300 $\overset{\circ}{A}$ diameter observed for the AISI 4340 steels used in this investigation the predicted strength of these cementite particles is $7.8 \times 10^6$ psi. Thus, the calculated value of the interface strength is, in fact, smaller than the estimated carbide strength, i.e., interface fracture would be expected as observed.

The major difference between the fracture surfaces of the AISI 4340 steels and the 18 Ni maraging steels was the presence of the small dimples on the AISI 4340 specimens. Roesch and Henry[37] have demonstrated that if the strengthening precipitate ($Ni_3Mo$) is coarsened by overaging, voids are nucleated by the precipitate in the maraging steels. Equation [VII-8] indicates that if the size of the carbides is reduced, the stress at the interface is reduced. It is of interest to estimate the size to which it would be necessary to reduce the carbides in the AISI 4340 in order to prevent nucleation of voids at them. The presence of this secondary void population probably accounts for the observed difference in the levels of toughness of the maraging and quenched and tempered steels.

It is assumed for this estimation that without the secondary nucleation of voids at the carbides, the commercial AISI 4340 will exhibit a fracture strain approximately that of the commercial 18 Ni maraging steel (since they have similar inclusion populations). Using a fracture strain of 0.70; the tensile flow curve for commercial AISI 4340 steel; and the intercept and slope

of Figure 46 as determined by least squares analysis, it is found that L

is approximately 1200 $\mathring{A}$. Thus, the model predicts that if the carbides

are reduced below 1200 $\mathring{A}$ in length, it should be possible to avoid nuclea-

tion of voids at them provided the martensitic grain size and flow charac-

teristics are not changed.

C.  Summary and Discussion of Void Initiation

The metallographic investigation of the void nucleation process in

these alloys has revealed a fundamental difference in void nucleation pro-

cesses between the AISI 4340 alloys and the 18 Ni 200 grade maraging

steels. Both populations of voids in the AISI 4340 alloys, i.e., both large

and small voids, are initiated by decohesion at the interface between second-

phase particles and the matrix. On the other hand, the voids in the maraging

steels are nucleated by cracking of titanium carbo-nitride inclusions. In

both alloy systems, the nucleation of voids at non-metallic inclusions occurs

only after the steels have been strained plastically. While no detailed study

has been made during straining of the progression of small void initiation

at carbides in the AISI 4340 alloys due to the difficulty of the observations,

it has been found that void initiation at non-metallic inclusions continues

throughout the strain history of each of the four steels. In all alloys, the

largest inclusions initiate voids at lower strains regardless of whether the

interface fails or the particle fractures. As straining proceeds, smaller

and smaller inclusions begin acting as sites for void initiation. The com-

parison of void initiation processes in both notched and smooth tensile speci-

mens revealed them to be the same regardless of specimen geometry.

Furthermore, the investigation has shown that there is no appreciable effect of triaxial stress level on void initiation processes in these alloys. Rather, the initiation of voids depends primarily upon the level of applied tensile stress.

The quantitative representations of void initiation presented in Figures 34, 36, 42, and 43 indicate a general similarity in the forms of the various curves. As suggested by Merchant,[145] the theoretical shape of these curves should be sigmoidal, as indicated in Figure 47a. This shape arises from the fact that void nucleation occurs first at the largest inclusions and proceeds to smaller and smaller inclusions as straining continues. Since the size distribution in particulate systems is log normal,[120] as shown in Figure 47b, only a few inclusions will nucleate voids at low levels of deformation. As the load is increased, smaller and smaller inclusions begin to nucleate voids such that there is a rapid increase in the percentage of inclusions nucleating voids since the greatest number of inclusions lie in the middle size range. At high stresses (or strains), the smallest inclusions begin to nucleate voids; but because the number of inclusions in the small size range is small, the rate of void initiation falls to a low level again.

Since all methods available today for determining particle-size distributions depend on the particles being spherical,[146] it is not possible to treat the distribution and nucleation curves quantitatively. However, it does appear that the above argument offers an explanation for the observed shape of the nucleation curves (Figures 34, 36, 42 and 43) which tend
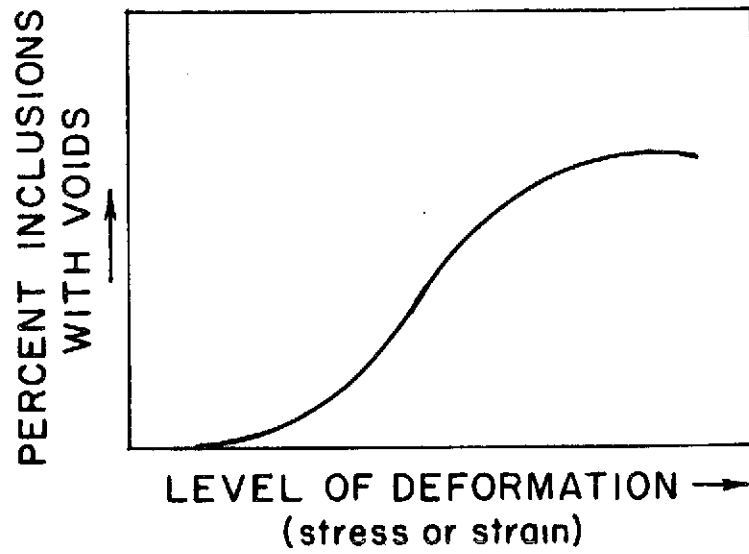
a) IDEAL NUCLEATION CURVE
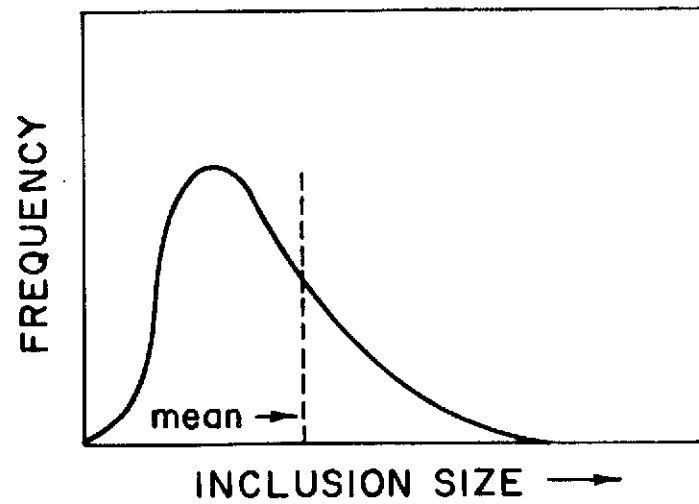
b) LOG NORMAL DISTRIBUTION

Figure 47   Ideal Nucleation and Inclusion Size Distribution
Curves.

toward sigmoidal shapes. This general treatment also suggests that by shifting the size level of the mean or peak of the inclusion size distribution (as has been done in the high-purity alloys), it should be possible to shift the sigmoidal nucleation curve to higher levels of deformation, i.e., improve the resistance of the alloy to void formation. The above predicted shift in the nucleation curve with refinement of the inclusion size is, in fact, observed in the figures.

CHAPTER VIII

VOID GROWTH

## A. Metallographic Observations

As the stresses are increased beyond the level at which void nu-
cleation first occurs in these alloys, the voids which have been initiated

at non-metallic inclusions grow by some mechanism involving plastic

flow of the matrix. The series of photomicrographs in Figures 48 and 49

illustrate the progressive increase in both the number and size of voids

in the necked regions of both smooth and notched specimens of commer-

cial AISI 4340 steel as the strain is increased. The increase in the num-

ber of voids as the strain increases is the result of continuing void initia-

tion at smaller and smaller inclusions, as noted in the previous chapter;

while the increasing size of voids is the result of progressive void growth.

These two simultaneously occuring processes result in a wide spread in

the sizes of voids present, as may be seen in the figures.

Examination of Figures 48 and 49 further reveals that the larger

voids appear to be found in the centers of the specimens, with the sizes

of voids generally decreasing as one moves away from the center line.

The general shapes of the voids also change from edge to center of the

midplane at high strains. In the centers of the smooth specimens and
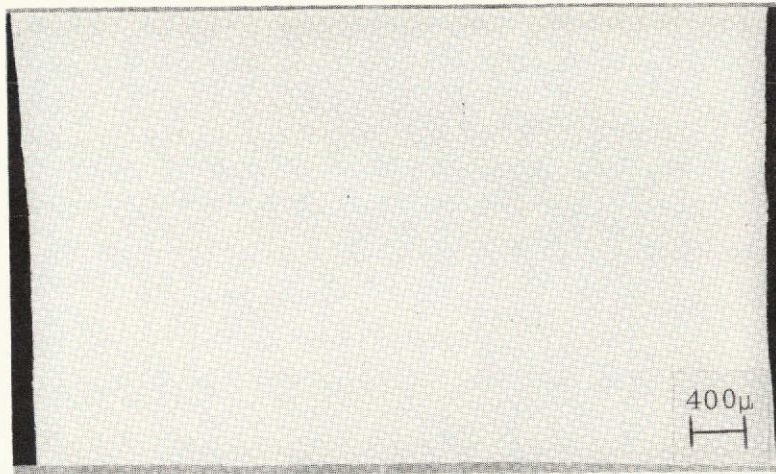
a) $\epsilon = 0.09$
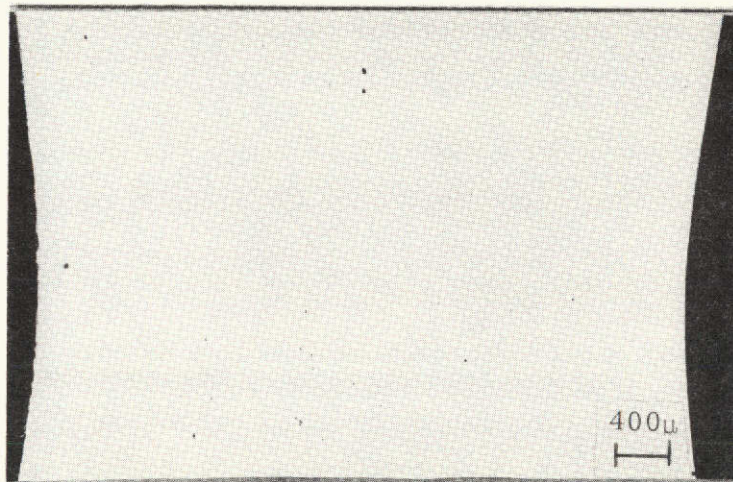
b) $\epsilon = 0.14$
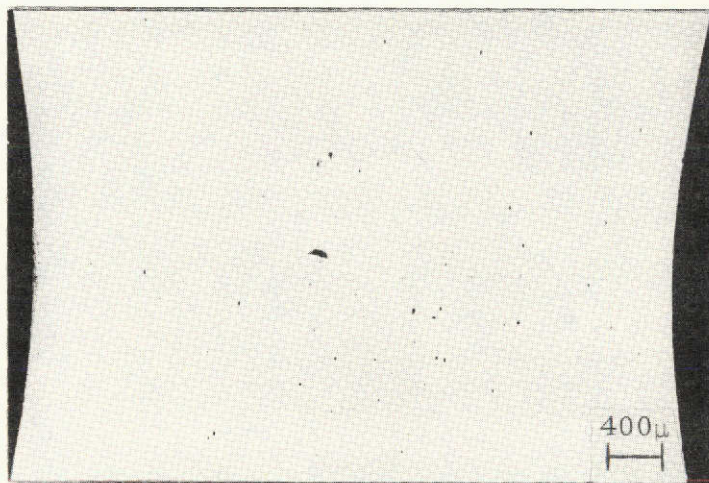
c) $\epsilon = 0.25$

Tensile
Axis

Figure 48 Midplanes of Necks of Smooth Tensile
Specimens of AISI 4340 Steel.
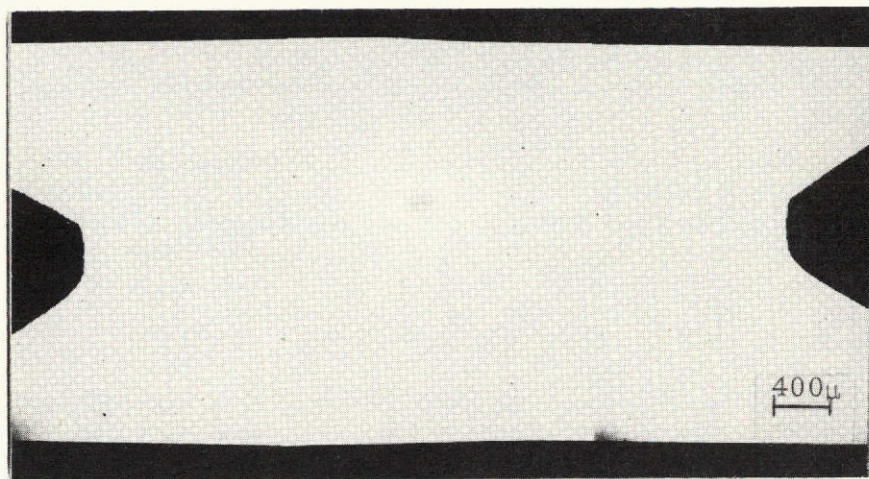
a) $\epsilon = 0.02$



Tensile Axis

b) $\epsilon = 0.03$



c) $\epsilon = 0.05$

Figure 49   Midplanes of Necks of Notched Tensile
Specimens of AISI 4340 Steel.

more generally in the notched specimens, the voids show a tendency to grow in both the direction of the tensile axis and in the radial direction (perpendicular to the tensile axis). Examples of voids in the central portion of smooth tensile specimens of commercial grade AISI 4340 which have grown during straining are presented in Figure 50. Although only examples from smooth specimens of the commercial alloy are shown, the observations are general and were observed in notched specimens and in the high-purity alloy.

It should be noted that at small strains (Figure 50a), the voids in the center of the specimen show little sideways growth, rather they tend to grow preferentially in the direction of the applied tensile stress. However, as the strain increases (Figure 50b and 50c), the voids in the central region of the neck grow both longitudinally and laterally. It has also been observed that the voids which are nucleated outside the necked region, i. e., removed from the minimum specimen diameter in the longitudinal direction, tend to show little lateral growth even at high strains. Likewise, voids towards the edges of the specimens also tend to lack evidence of appreciable growth in the radial direction even at high strains. These voids lying away from the center of the neck tend to be elongated in the direction of the tensile axis and are generally no wider than the nucleating sulfide. Examples of elongated voids near the edges of tensile specimens of commercial grade AISI 4340 strained plastically are presented in Figure 51. Apparently, the large degree of triaxial stress in the center of the neck which develops at high strains aids the lateral growth of the voids.
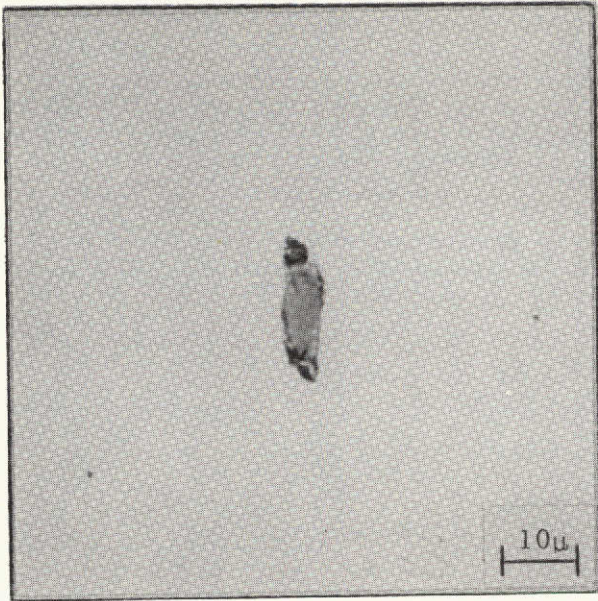
a) $\epsilon = 0.09$
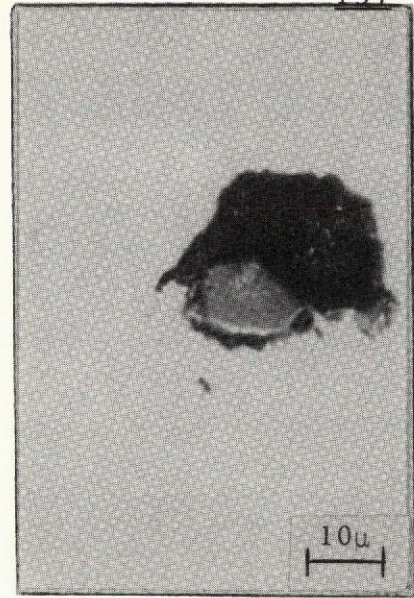
b) $\epsilon = 0.17$
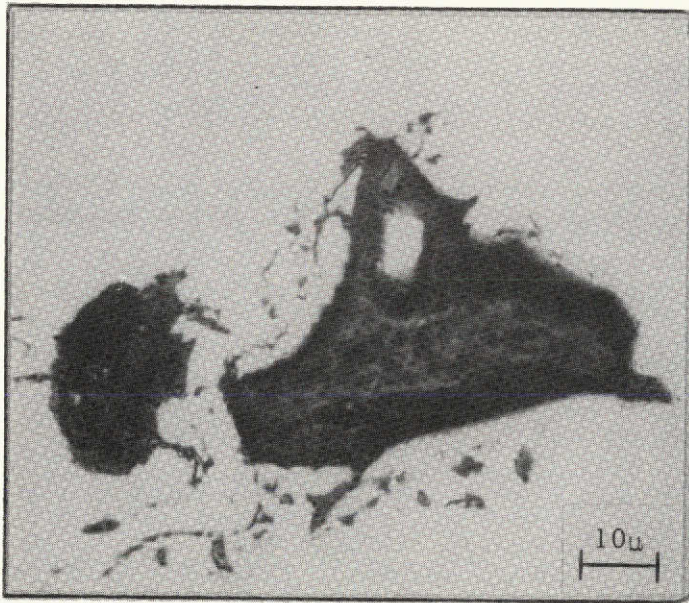
Tensile
Axis

Figure 50   Voids in the Centers of Smooth Tensile Specimens of AISI 4340 Steel Strained Plastically.

a)  $\epsilon = 0.17$
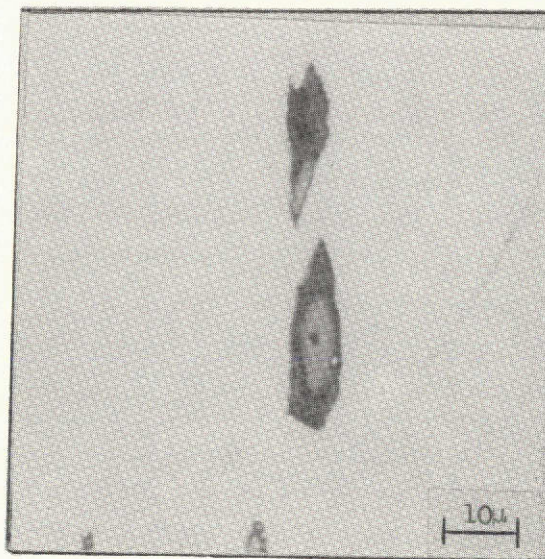


Tensile
Axis

b)  $\epsilon = 0.25$

Figure 51    Voids on Edges of Smooth Tensile
Specimens of AISI 4340 Steel
Strained Plastically

These general metallographic observations of the growth process in the AISI 4340 alloys are similar to those observed for the 18 Ni maraging steels. Both maraging alloys and both specimen geometries for these 18 Ni alloys exhibit the same characteristics although the illustrations below will be made using the results for the smooth specimens of the commercial alloy only.

The general increase in the size and number of voids on the midplane of the neck with increasing strain may be readily seen in Figures 52 and 53. From these photomicrographs, it is also possible to see that the voids in the central portions of the necks seem to be larger than those near the edges, especially at larger strains. Similar to the behavior found in the AISI 4340 alloys, voids in the central portion of the neck of the maraging specimens grow almost symmetrically at higher strains, while those near the edge or those lying outside the neck tend to be elongated in the direction of the applied tensile stress. Voids near the edge or away from the neck exhibit no appreciable sideways growth even at very high strains, while those in the center grow longitudinally at low strains but begin to exhibit lateral growth at high levels of plastic strain. Figures 54 and 55 illustrate these observations for the commercial grade maraging steel.

Thus, qualitatively, the void growth process appears to be very similar in all four alloys. At low strains, the void nuclei tend to grow in the direction of the applied tensile stress. As straining continues, a prominent neck is formed in the smooth specimens and with the pre-existing neck in the notched specimens, a substantial triaxial state of stress is
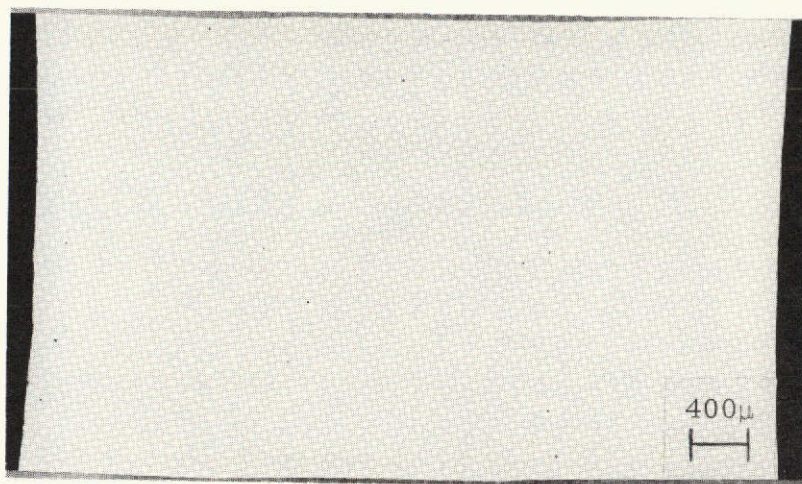
a)  $\epsilon = 0.18$
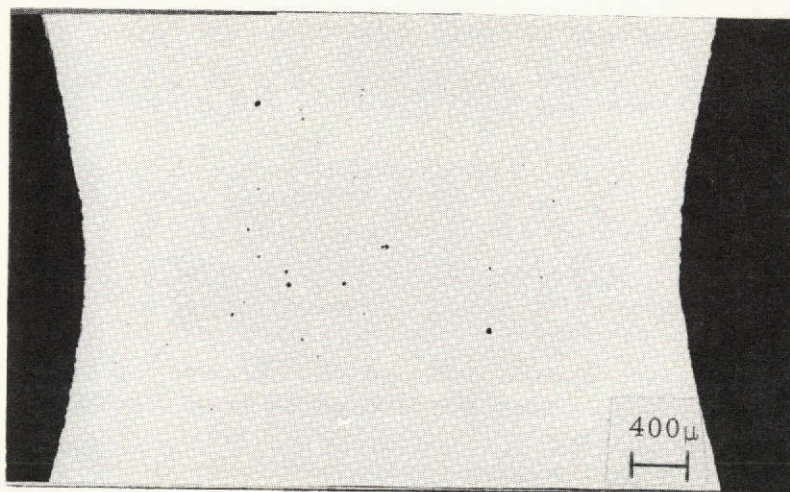
b)  $\epsilon = 0.58$
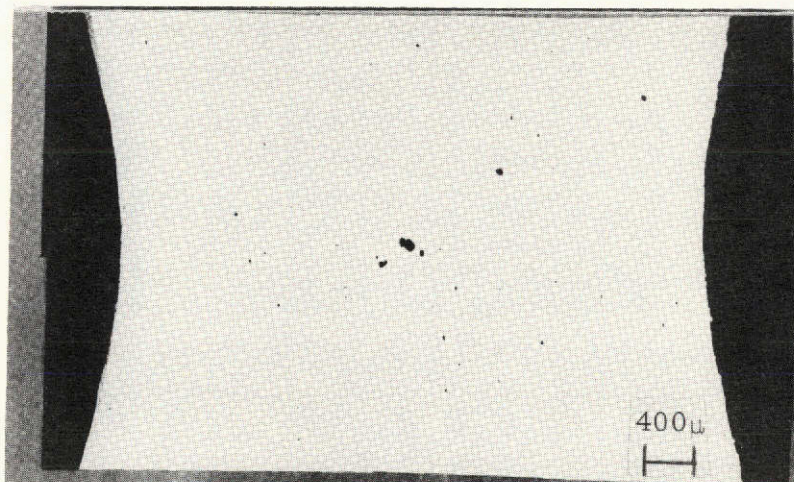
Tensile
Axis

c)  $\epsilon = 0.62$

Figure 52  Midplanes of Necks of Smooth Tensile
Specimens of 18 Ni Maraging Steel.

a) $\epsilon = 0.05$
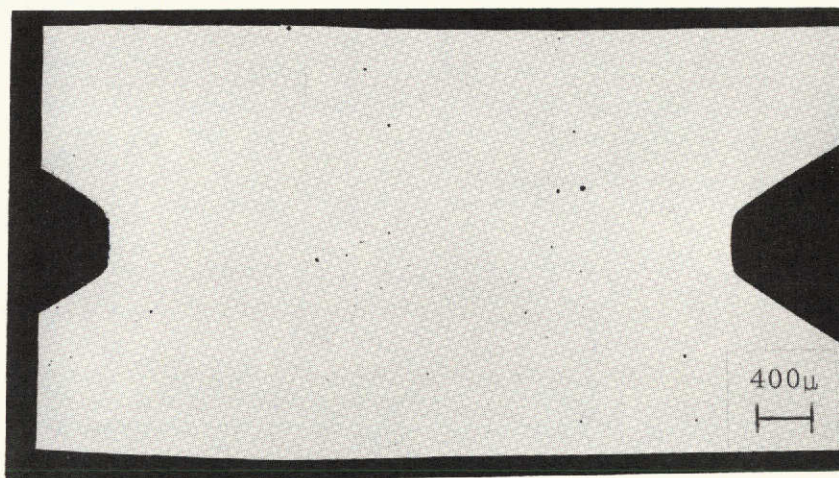


Tensile
Axis

b) $\epsilon = 0.08$



c) $\epsilon = 0.12$

Figure 53  Midplanes of Necks of Notched Tensile
Specimens of 18 Ni Maraging Steel.
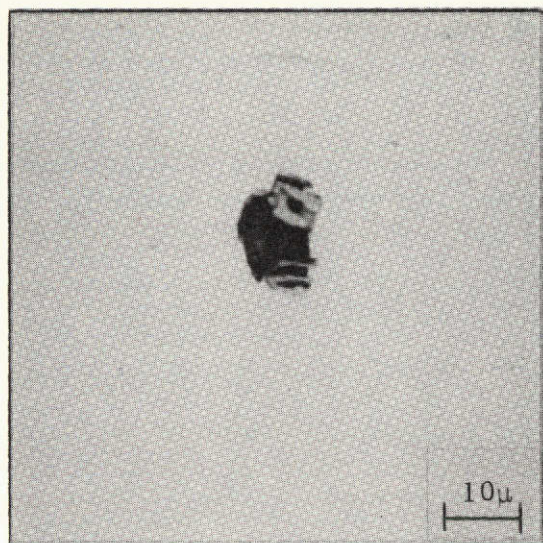
a)  $\epsilon = 0.18$
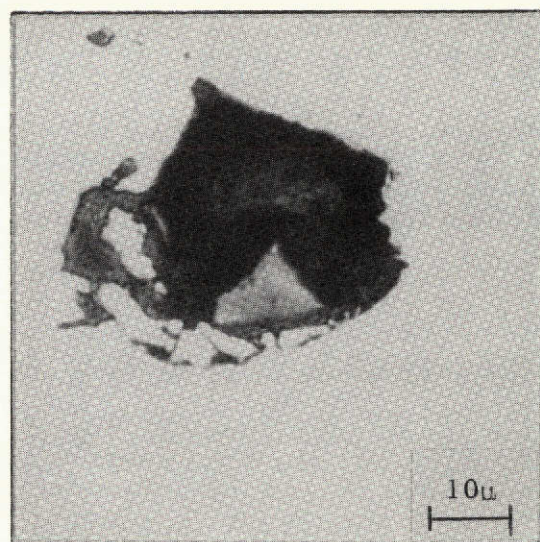
b)  $\epsilon = 0.58$
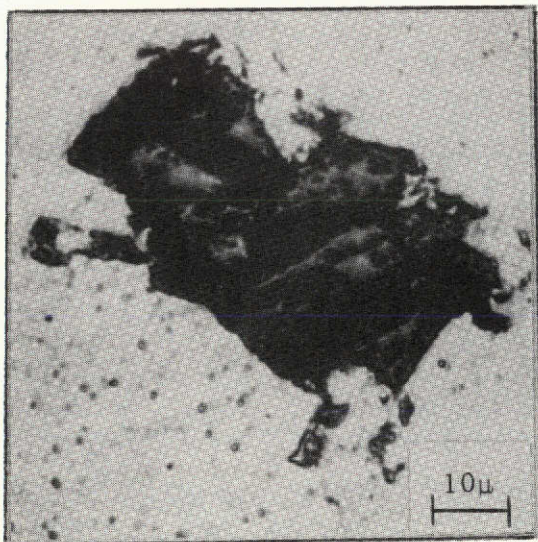
c)  $\epsilon = 0.66$

Tensile Axis

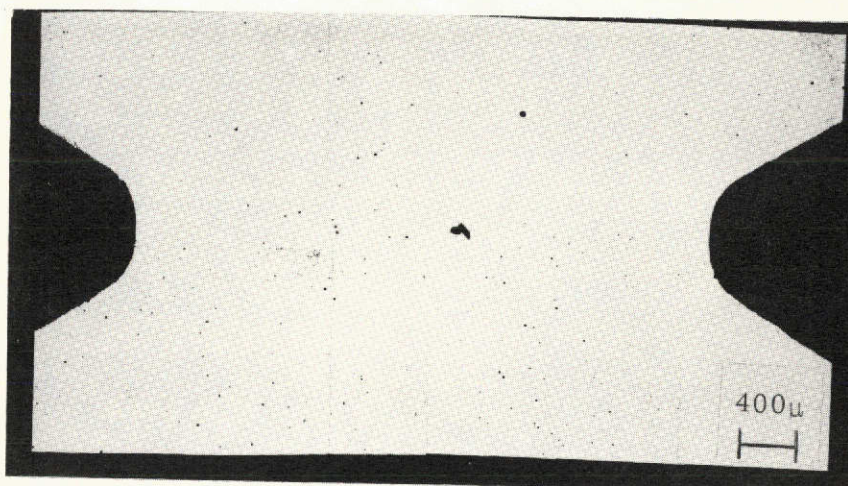Figure 54  Voids in the Centers of Smooth Tensile Specimens of 18 Ni Maraging Steel Strained Plastically.

a) ε = 0.18



b) ε = 0.58



c) ε = 0.66
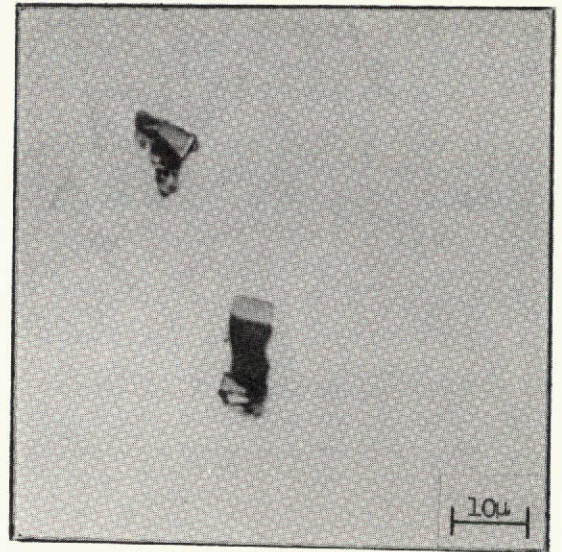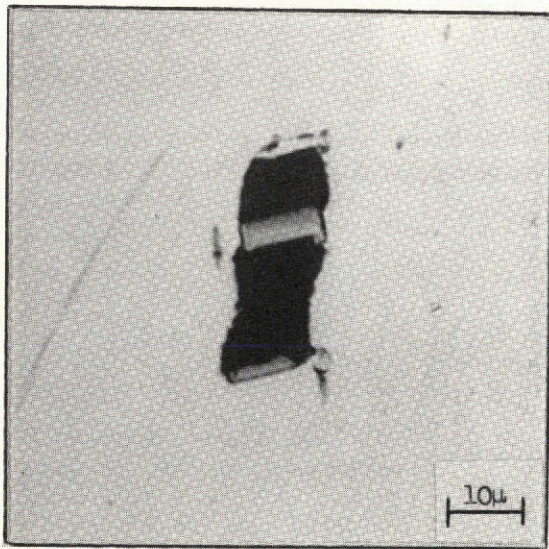
Tensile Axis

Figure 55    Voids on the Edge of Smooth Tensile Specimens of 18 Ni
Maraging Steel Strained Plastically

developed in the centers of the tensile specimens. Under the influence

of the triaxial state of stress, the voids in these alloys tend to grow more

uniformly, exhibiting lateral or radial growth as well as the earlier es-

tablished longitudinal growth. Those voids which lie outside the regions

of substantial triaxiality (those towards the specimen edge or lying out-

side the necked region) continue to grow preferentially in the direction of

the applied tensile load.

No effort has been made to correlate the exact stress states at par-

ticular points along the minimum diameter (known from the Bridgman

analysis) with the sizes of voids present. It was demonstrated in the pre-

vious chapter that void initiation depends on inclusion size and will be

shown below that void growth also depends on inclusion size. Thus, the

size of void present at a particular location is a function not only of the

stress state at the point but also is dependent on the size of inclusion that

happens to lie at that particular point. The spacial distribution of inclu-

sion sizes is assumed to be random in these alloys. Hence, considering

the probability of the existence of inclusions of one particular size, shape,

and orientation at specific locations, the problem of correlating void sizes

quantitatively with the exact stress states appears to be intractable.

B. Quantitative Measurements

As indicated in Chapter VI, the macroscopic critical regions of the

tensile necks were examined in their entirety at 1000X. After the data for

void nucleation were collected in each microscopic area, a transparent

sheet with a square point grid of 0.5 cm spacing was placed over the

screen and the number of intersections of the grid and the voids present

on the section was determined. Using the standard point counting tech-

nique referred to previously, [111] it was possible to determine the area

fraction of the test section covered by voids. Using this information to-

gether with the number of voids present on the test section permitted

calculation of the average cross-sectional area of void intersected by the

midplane. This particular measure of void size was chosen since it was

observed that the voids are generally quite irregular in shape such that

the measurement of some linear dimension of the voids, e. g., length or

width, has questionable utility. By recording the data for each micro-

scopic area examined, it was possible to determine the effects of loca-

tion in the necks on void growth.

The values of the average cross-sectional areas of voids inter-

sected by the midplanes as a function of strain are presented in Figure

56. Each of the curves in the figure shows a linear initial portion where

the average size of void increases continuously with strain. At the higher

levels of strain, the curve (especially those for the smooth specimens)

show a rapid increase in the size of voids present. This rapid jump cor-

responds with the onset of void coalescence and the formation of a large

central cavity in the tensile specimen. It should be noted that the rates

of void growth are generally higher for the commercial grade alloys and

noticeably higher for the notched specimens.

Actually, the average cross-sectional area of void represents the

combined effects of void nucleation, growth, and coalescence such that the
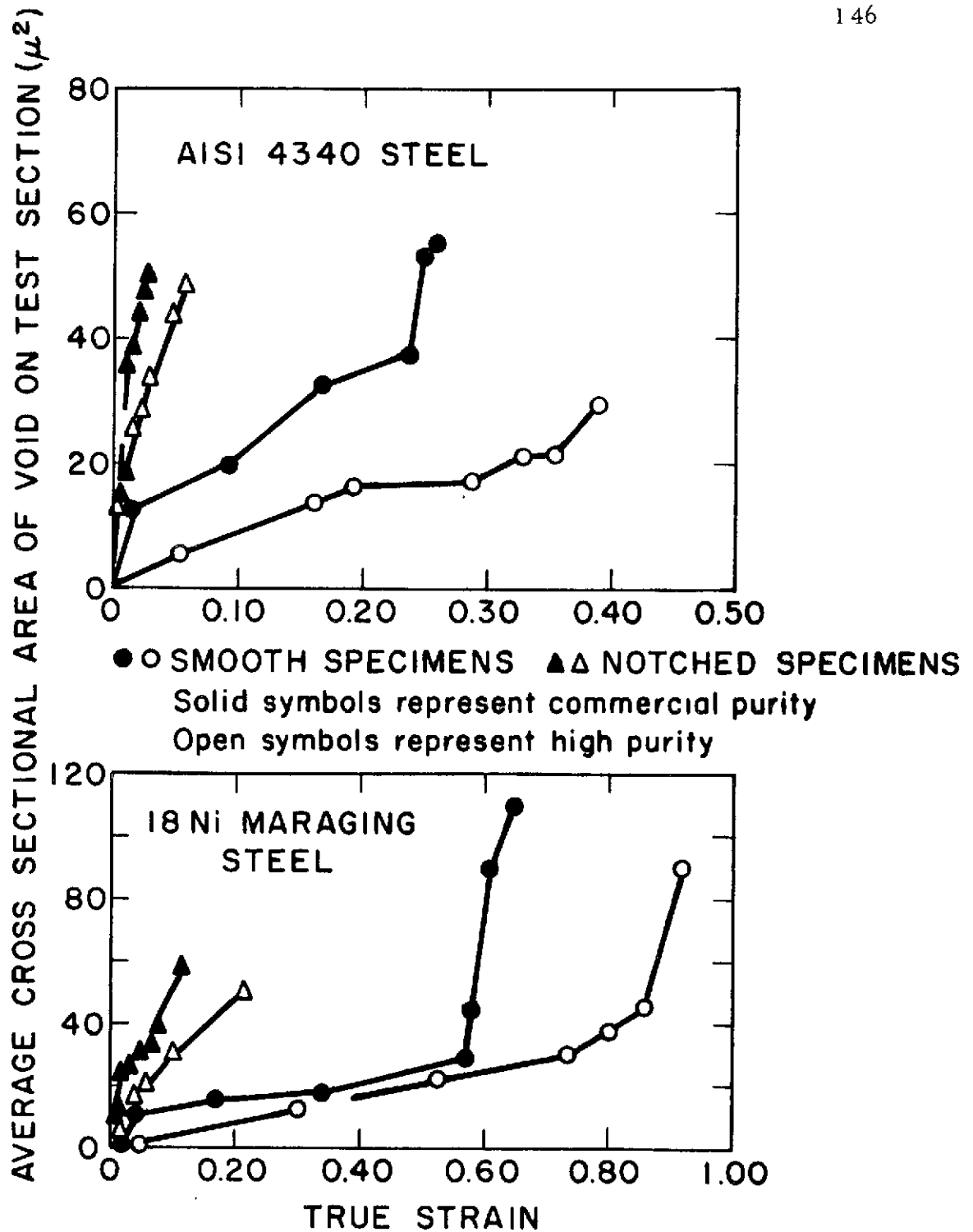
Figure 56  Average Cross Sectional Area of Void
as a Function of Strain.

plots in Figure 56 represent some measure of the progress of the total fracture process. These results do indicate that at any given strain the most detrimental situation is found in the notched commercial grade AISI 4340 steel while the least damaging situation is found in the smooth high-purity grade 18 Ni maraging steel. The general order of the curves follows the observed values of fracture strains, i. e., ductilities, to be found in these alloys.

In order to separate the effects of void nucleation and growth, the cross-sectional area of the largest void present on the midplane was determined. The reasoning behind this choice is that the largest void present would naturally be the one which had nucleated first (at the largest inclusion) and had grown continuously as the strain had increased, and thus represents the best available information regarding void growth. The results of the tabulation of the largest void sizes as a function of strain are presented in Figures 57 and 58.

These figures indicate that for any given alloy the rate of void growth is greater in the commercial purity material than in the high-purity material. This fact is probably due to the differences in inclusion size when going from commercial purity to high-purity alloys. While the volume fraction of inclusions is greater in the commercial purity alloys (see Table III), the center-to-center distances between inclusions are larger in the commercial alloys due to the smaller number of inclusions present. If the differences in the sizes of the inclusions between high-purity and commercial purity alloys are considered, it is seen that the boundary-to-boundary
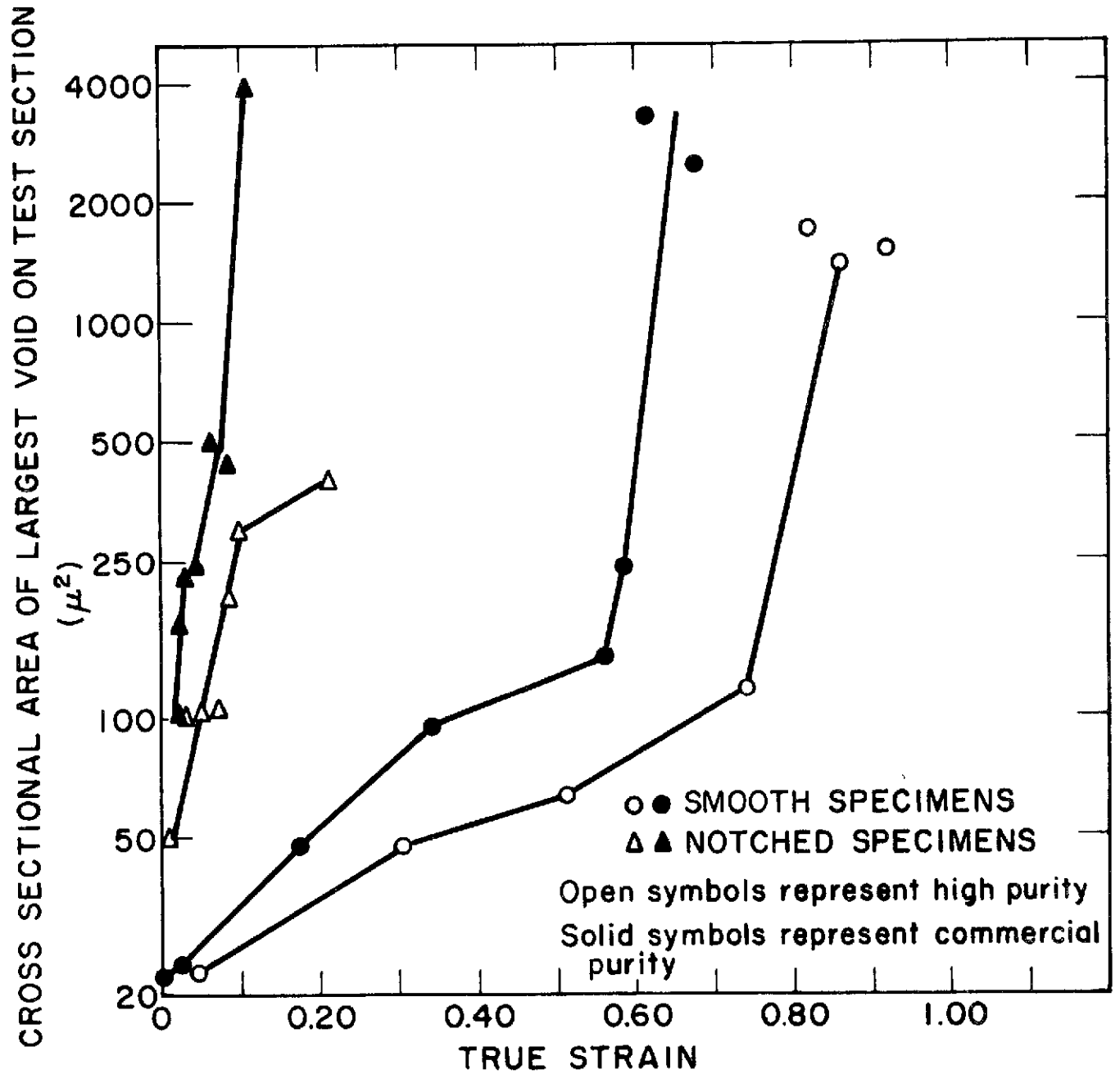
Figure 57   Cross Sectional Area of Largest Void
as a Function of Strain for 18 Ni Maraging
Steel.
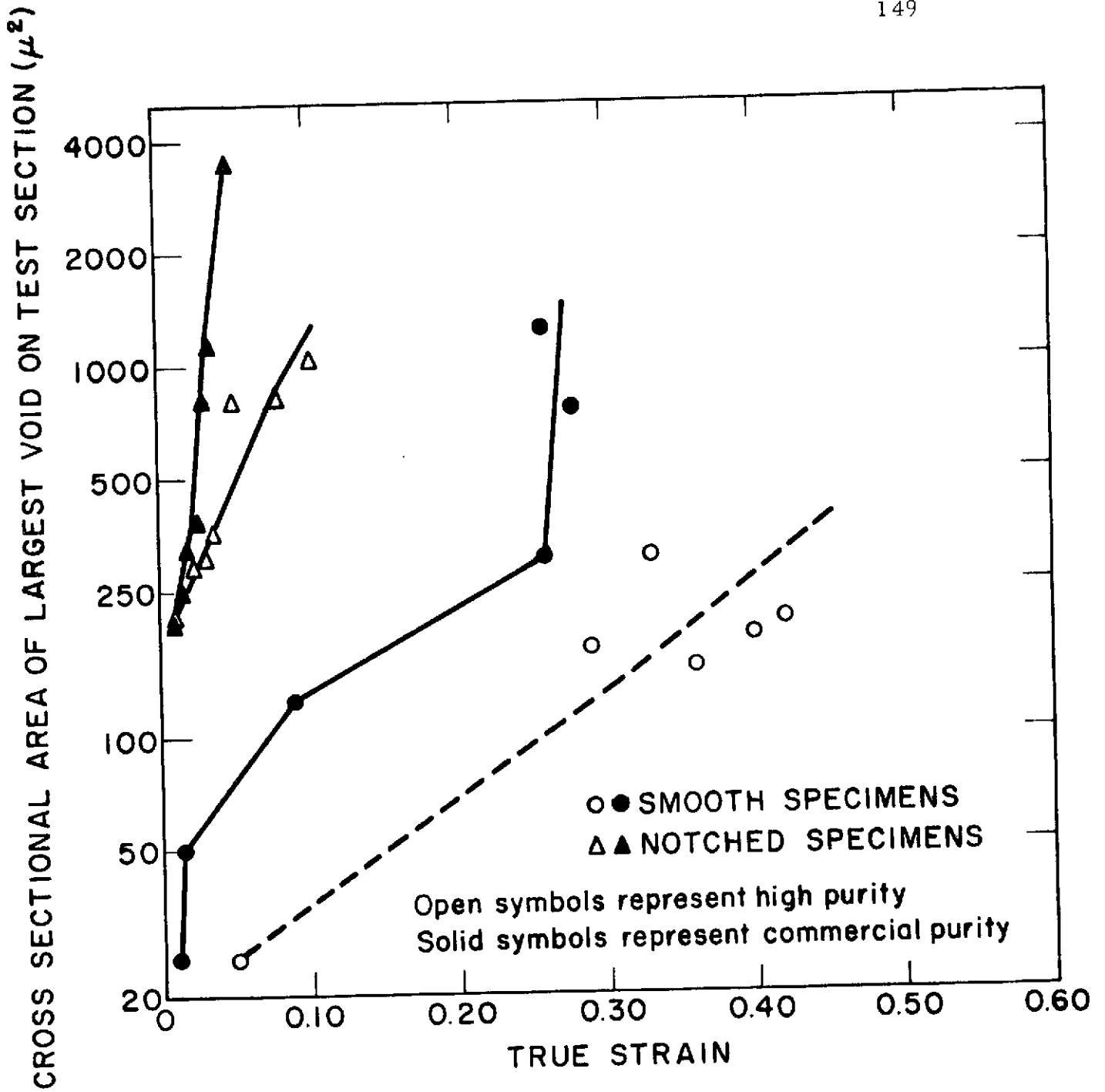
Figure 58 Cross Sectional Area of Largest Void
as a Function of Strain for AISI 4340
Steel.

distances between nearest neighbor inclusions are roughly the same for both purity levels in a given steel. Once voids nucleate at neighboring inclusions, they have approximately the same amount of growth in the matrix required before impingement in both commercial and high-purity alloys. Thus, the primary difference between the alloys regarding growth of voids stems from the fact that the voids nucleate earlier in the commercial steels since the inclusions are larger; and because the inclusions are larger, the resulting voids are born larger which produces increased levels of applied stress due to the reduced cross-sectional area. With the increased levels of stress in the commercial alloys, the voids grow more rapidly. The increased stress also results in the nucleation of more voids which further increases the stress, such that the process leads more rapidly to the point where the voids coalesce in the commercial alloys than it does in the high-purity alloys. These conclusions regarding the detrimental effects of inclusion size are supported by the recent work of Darlington[151] who studied fracture in electrolytic iron and spheroidized low carbon steel.

The results presented in Figures 57 and 58 also demonstrate that the increased level of triaxial stress introduced in the notched specimens greatly increases the rate of void growth. At a given level of strain, the flow stress (which is twice the maximum resolved shear stress) is approximately the same in both smooth and notched specimens as demonstrated in Chapter IV yet the sizes of the voids are much larger in the notched specimens and the rate of void growth is greater. This difference in void size

must then be the result of the level of triaxiality. While it was shown in the previous chapter that stress triaxiality has no effect on void nucleation in these alloys, it is apparent from the data in Figures 57 and 58 that the detrimental effects of triaxial stress states on the fracture resistance of these steels is due in some measure to the increased rates of void growth produced by triaxiality.

Increased levels of triaxiality will increase the required applied stresses to cause general plastic flow in the matrix. It seems plausible that restricted flow in the matrix would tend to concentrate the plastic deformation at the existing voids where the stresses are highest and constraints reduced. At the free surfaces of the voids, the triaxial stress state is relaxed since the stresses normal to the free surface go to zero. Thus the maximum shear stress increases near the surface resulting in increased plastic deformation. Furthermore, the presence of the void produces a stress concentration which further encourages plastic deformation. Hence as the level of triaxiality increases, the full effects of the increased applied stress can be realized by intense deformation around the voids resulting in enhanced growth.

There have been several attempts to describe the void growth process in the past. Many of the treatments involve expressions for predicting void size from the strain. However, for several of the cases, [41,55] it is difficult to compare the results of the current investigation with those predicted because the treatments contain various arbitrary constants which are used to make the data fit. On the other hand, the work of Rice and Tracey[59]

involves complex expressions of strain rate which are not readily inte-
grated for comparison with the current data. The analyses to which the
data here may be most readily compared are those of McClintock[57, 58]
which are based on continuum plasticity and involve no arbitrary constants.

McClintock considers an isolated hole with the shape of a right
prism of elliptical cross-section. The expression for the size of the void
is then given by:

$$\ln \frac{R}{R_o} = \frac{\bar{\epsilon}\sqrt{3}}{2(1-n)} \sinh \left\{ \frac{\sqrt{3}(1-n)}{2} \frac{(\sigma_a + \sigma_b)}{\bar{\sigma}} \right\} + \left\{ \frac{\epsilon_a + \epsilon_b}{2} \right\} \qquad [\text{VIII-1}]$$

where $R = \frac{L + W}{2}$ (L and W are the major and minor radii of the ellipse)
and $R_o$ is the initial value of $\frac{L + W}{2}$; $\bar{\epsilon}$ is the true strain; $\bar{\sigma}$ is the true stress;
n is the strain hardening exponent; $\sigma_a$, $\sigma_b$ and $\epsilon_a$ and $\epsilon_b$ refer to the stresses
and strains along the major and minor axes of the elliptical cross-section.

In order to compare the present data with the McClintock analysis,
it was necessary to designate some values for R. The areas of the largest
voids were used to calculate the radii of circles of equivalent areas and $R_o$
was taken as the equivalent radius of the average size inclusion. The rela-
tionships between the equivalent void radii and strain are presented in
Figure 59 using only the data collected before any coalescence was observed.
The values observed for the maraging steels agree reasonably well with
those observed by Floreen and Hayden for an 18 Ni 300 grade maraging
alloy.[50]

Using Equation [VIII-1] and the values of the various materials con-
stants for the commercial grade maraging steel, the values of R for various
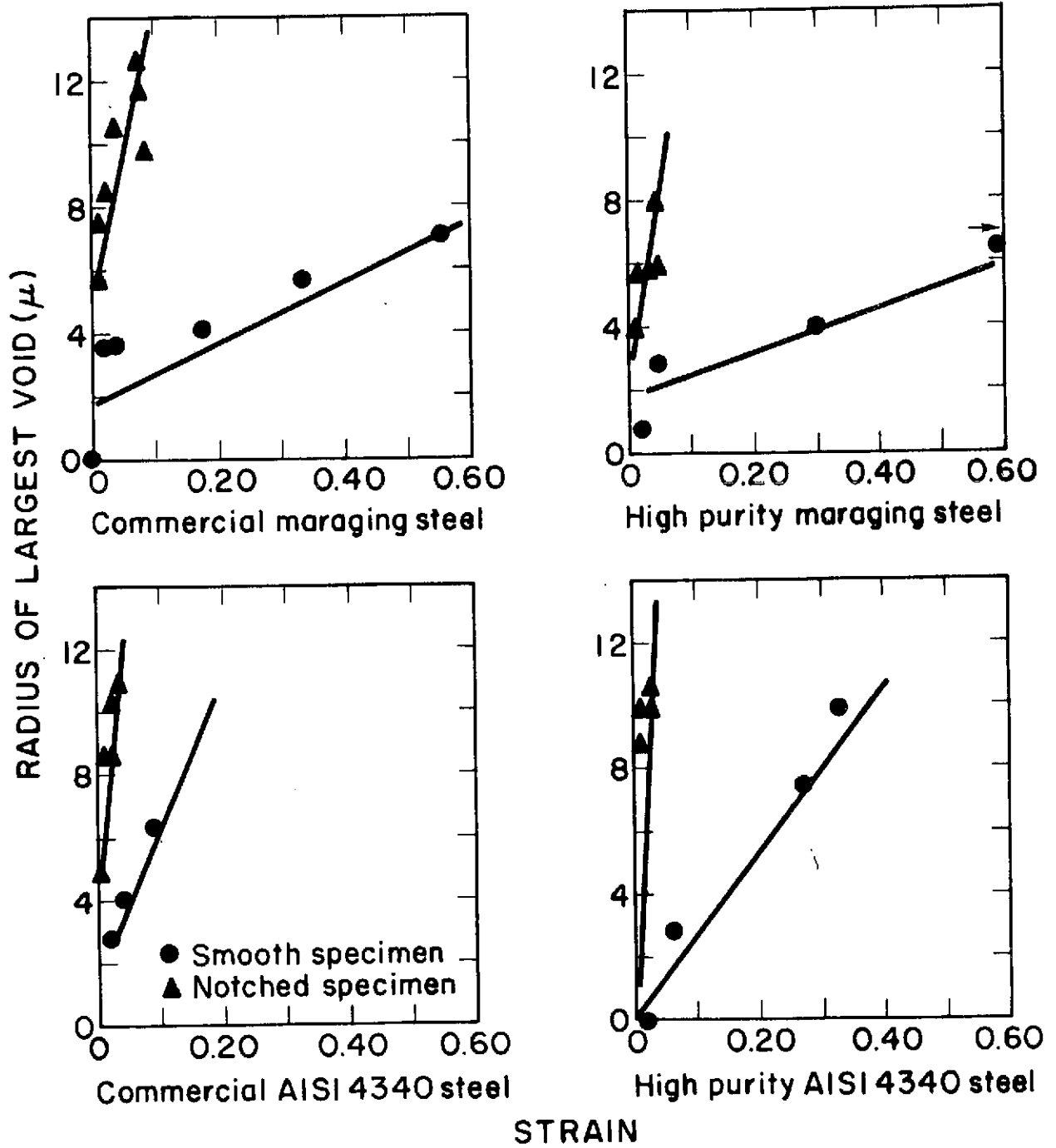
Figure 59   Radii of Largest Voids as a Function of
Strain.

strains were calculated. A comparison of the observed values of R with those predicted by the McClintock treatment are presented for the commercial maraging steel in Figure 60. The comparison shows that the analysis does not agree well with experiment. At low strains for the smooth specimens the predicted values are only half or a third of those observed, while at higher strains, the agreement is even worse. The poor agreement probably results because the McClintock analysis assumes no interaction between voids, i.e., it should be good only for the very early stages of void growth and for systems with much larger spacings between inclusions than those encountered in this study. The poor agreement between the notched data and that predicted by the model indicates that the analysis does not accurately predict the effects of increased hydrostatic tension for these alloys. This fact is again probably due to the large number and close spacing of inclusions (and thus voids) encountered in practical alloys. To illustrate this point consider the notched tensile specimens of the high purity AISI 4340 steel. At a strain of 0.023, over 50 percent of the inclusions had voids associated with them and the equivalent radius of the largest void intersected by the test plane was 9 microns. As was presented in Table III the average center-to-center distance between nearest neighbor inclusions in the high-purity AISI 4340 alloy is 29 $\pm$ 7 microns. We may then approximate the distance between the edges of neighboring voids in the center of the specimen as 11 microns by subtracting twice the void radius from the interinclusion spacing. Thus the distance between voids (edge to edge spacing) is approximately half the diameter of the voids in the center of the specimen.
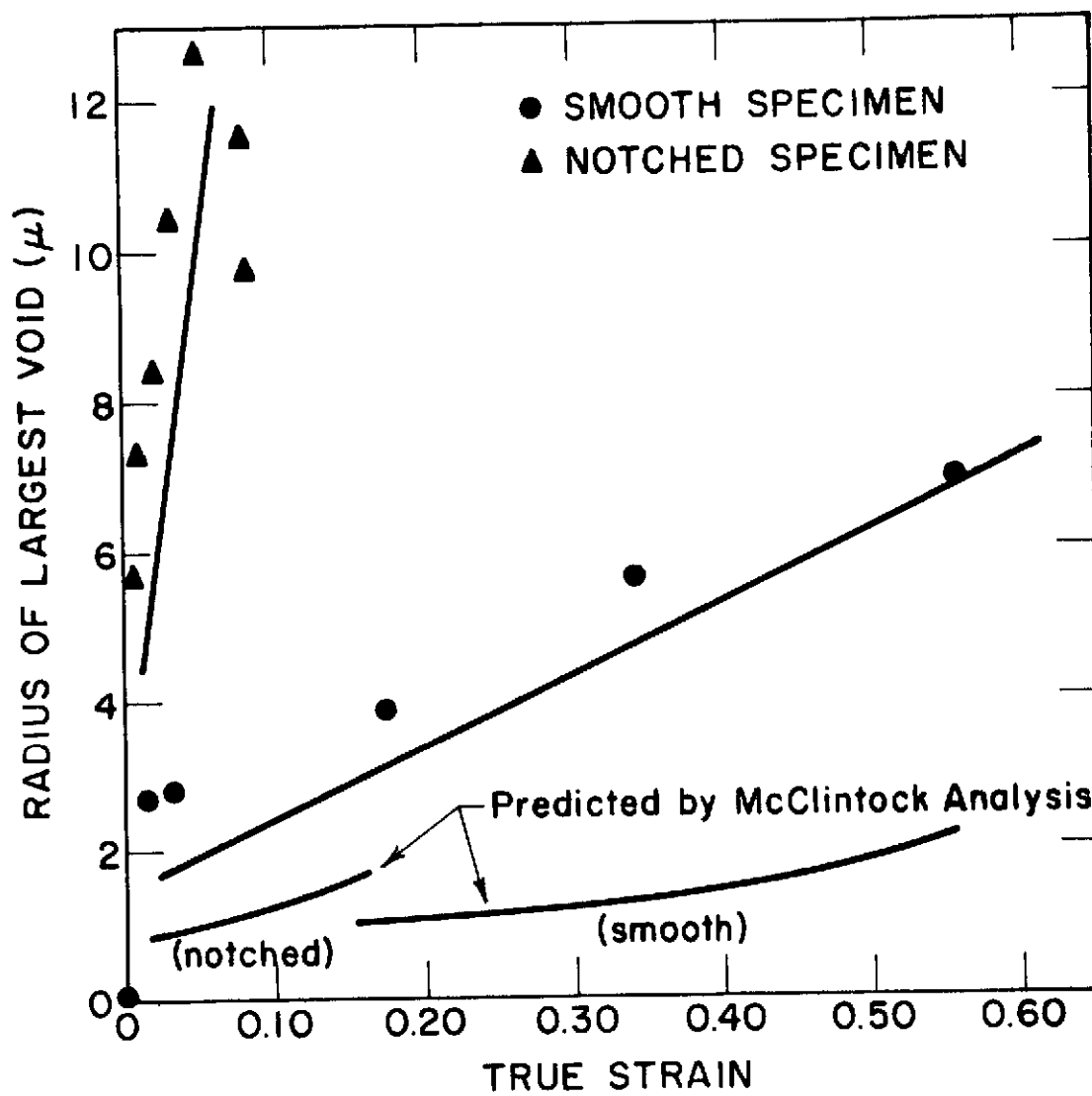
Figure 60  Void Growth Relationship for Commercial
18 Ni Maraging Steel.

Clearly there would be a strong interaction between voids in this case.

Using the data presented in Figure 59, a least squares analysis was used to determine the rates of void growth observed in these alloys. The results of these calculations are presented in Table VII. It may be seen in the table that the rates of void growth increase dramatically in the notched specimens due to the increased triaxiality of the stress system. The effects of inclusion size may be seen in the decrease in void growth rates when going from the commercial alloys to the high-purity. It should also be noted that the general level of growth rate is higher in the AISI 4340 alloys than in the maraging steels. This difference is probably due to the fact that at any given strain the percentage of inclusions with voids and hence the number of voids is greater in the AISI 4340 alloys than in the maraging. This fact results in increased levels of applied stress for a given strain in the AISI 4340 steels as compared with the maraging steels and hence larger voids.

If the growth rates for the maraging alloys are used to predict the diameters of the resulting dimples on the fracture surfaces by multiplying them by the values of strain at which void coalescence is first observed, the predicted dimple diameters are 12 and 28 microns for the smooth and notched commercial alloy and 13 and 26 microns for the high-purity maraging alloy. These values may be compared with those measured on the fracture surfaces and recorded in Table IV. Since the values taken from the fracture surfaces vary from 14 to 34 microns, the agreement seems reasonable considering the approximations made in determining the values of the radii from

TABLE VII

Rates of Void Growth

| Alloy | Growth Rate (Expressed as the rate of increase of the equivalent radius in microns per unit of strain) | |
| --- | --- | --- |
| | Smooth | Notched |
| Commercial 18 Ni Maraging | 10 ± 2 | 147 ± 32 |
| High-Purity 18 Ni Maraging | 7 ± 2 | 130 ± 20 |
| Commercial AISI 4340 | 64 ± 13 | 419 ± 37 |
| High-Purity AISI 4340 | 19 ± 4 | 380 ± 88 |

the tensile sections and the errors of the fracture surface measurements. Errors occur because the section does not generally cut the largest void exactly at its midplane. Also, the voids tend to become ellipsoidal in cross-section with the long diameter in the radial direction as the strains reach those where coalescence occurs. Thus, the equivalent radii would tend to be slightly less than those observed on the fracture surface. Also, as pointed out in Chapter V, the measurements made on the fracture surfaces are only approximations which result in some error.

# CHAPTER IX

## VOID COALESCENCE

### A. 18 Ni Maraging Steel

As is suggested by examination of the fracture surfaces of the 18 Ni maraging steels which are covered with large dimples centered on fractured carbo-nitride inclusions, the metallographic examination of strained and sectioned specimens of the maraging alloys demonstrates that the inclusion nucleated voids coalesce by growing until they impinge on one another. This behavior of literally growing into one another had been suggested early as a possible mechanism of void coalescence by Cottrell.[52] The first appearance of the coalescence of voids in both the high-purity and commercial maraging steels was observed to occur at strains of approximately 80 percent of the fracture strains for the smooth specimens and between 40 and 60 percent of the fracture strains for the pre-notched specimens. An example of voids coalescing in a smooth specimen of high-purity maraging steel is presented in Figure 61. As straining continues, the void coalescence process leads to the formation of a large central cavity, as illustrated for a smooth specimen of commercial maraging steel in Figure 62. Once a cavity as long as 5 to 10 percent of the minimum specimen diameter was formed, final fracture occurred

159
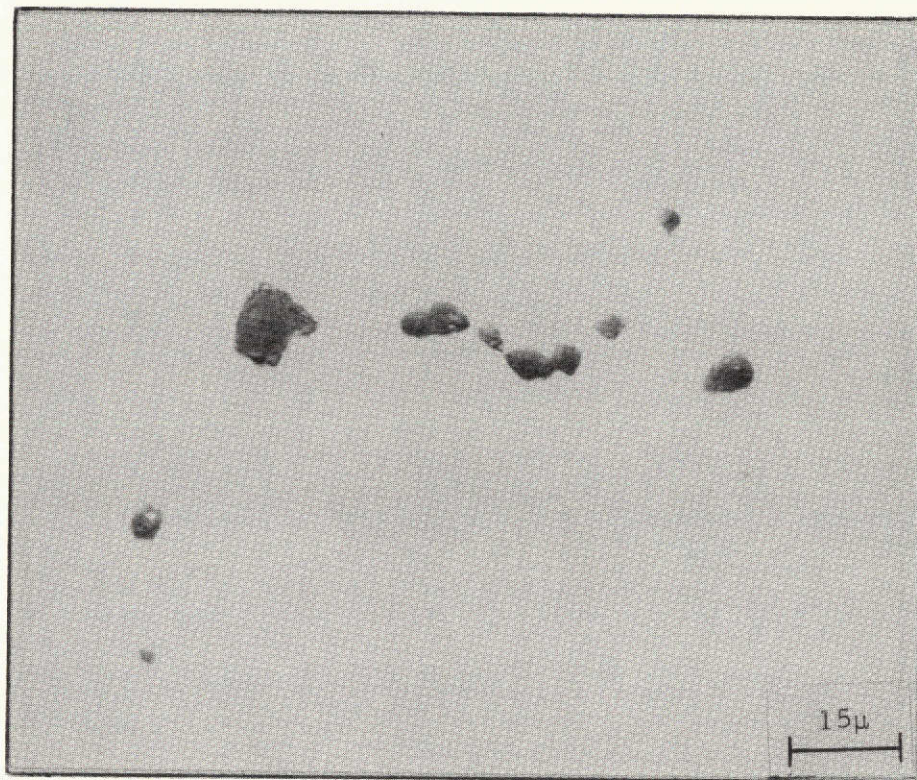
Tensile Axis

Figure 61    Void Coalescence in Smooth Specimen of
High-Purity 18 Ni Maraging Steel, $\epsilon = 0.81$.
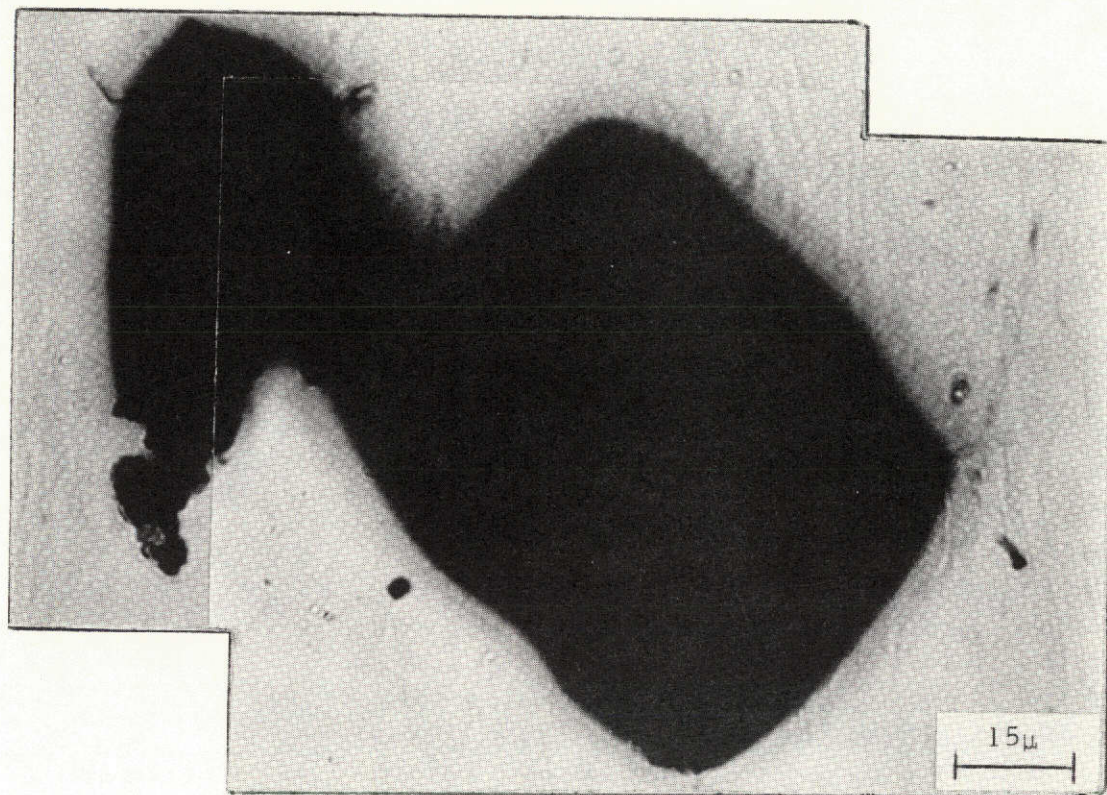
Tensile Axis

Figure 62   Central Cavity in Smooth Specimen of Commercial
Purity 18 Ni Maraging Steel, $\epsilon = 0.61$.

very rapidly.

This same process of void coalescence was observed in the notched specimens. It was generally observed that the strains at which the coalescence of voids was first detected were smaller in the notched specimens, approximately 20 percent of those observed in the smooth specimens. This early development of coalescence obviously follows from the higher void growth rates observed in the notched specimens. Furthermore, the duration of the coalescence process, i.e., the difference between the strain at which coalescence is first detected and the fracture strain, was found to be much shorter in the notched specimens, of the order of half the values noted for the smooth specimens. The foreshortened coalescence stage of the voids in the notched specimens must also be a direct result of more rapid growth under the influence of the higher triaxial stresses.

B.  AISI 4340 Steel

Thus far  it has been seen that at least qualitatively the processes of void initiation and growth from non-metallic inclusions in the two alloy steel families are not essentially different. However, the process of the coalescence of inclusion-nucleated voids in the AISI 4340 alloys differs dramatically from that in the maraging steels. One would expect as much after considering the fracture surfaces of the quenched and tempered steels which are covered by two distinct populations of dimples. Based on observations made from the strained and sectioned tensile specimens, it is found that the large voids nucleated at manganese sulfide inclusions coalesce by

the propagation of crack-like features which link adjacent large voids. The first appearance of this coalescence occurs at approximately 60 to 80 percent of the fracture strain for the smooth specimens and approximately 30 to 40 percent of the fracture strain for the notched specimens. A photomicrograph of the early stages of void coalescence in a smooth specimen of the commercial AISI 4340 alloy is presented in Figure 63. At strains within a few percent of the fracture strain, the coalescence of voids in the central region of the tensile specimen is extensive enough to form a rather large continuous cavity spanning as much as 5 or 10 percent of the specimen diameter. Final fracture occurs catastrophically after this point. An example of such a cavity is presented in the composite photomicrograph of Figure 64 taken from a smooth specimen of the commercial alloy.

The crack-like features which link the large inclusion-nucleated voids in the AISI 4340 alloys have the appearance, early in their existence, of a collection of small voids similar to the "void sheets" described by Rogers[12] as observed during the fracture of copper. This fact is readily seen in the example presented in Figure 65a. As the strain is increased, the small voids coalesce and the "void sheet" becomes an actual crack of substantial opening, running between the large voids, as demonstrated in Figure 65b. That the features are, in fact, sheets of voids, i.e., planar features composed of many small voids, was demonstrated by serial sectioning of several of the sheets. Examples of sections taken at various depths below the midplane of the feature presented in Figure 65a are displayed
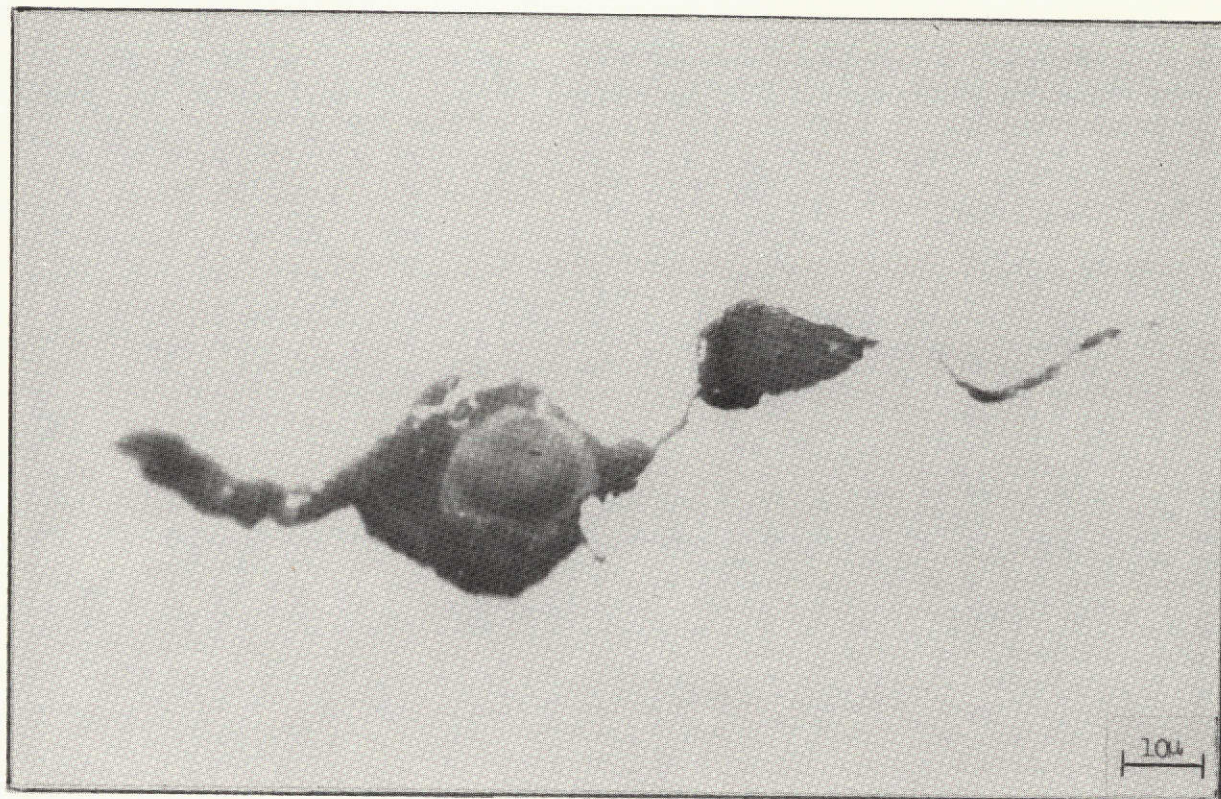
Tensile Axis

Figure 63    Void Coalescence in Smooth Specimen of Commercial
Purity AISI 4340 Steel, $\epsilon = 0.25$

Tensile Axis

Figure 64   Central Cavity in Smooth Specimen of Commercial
Purity AISI 4340 Steel, $\epsilon = 0.27$.
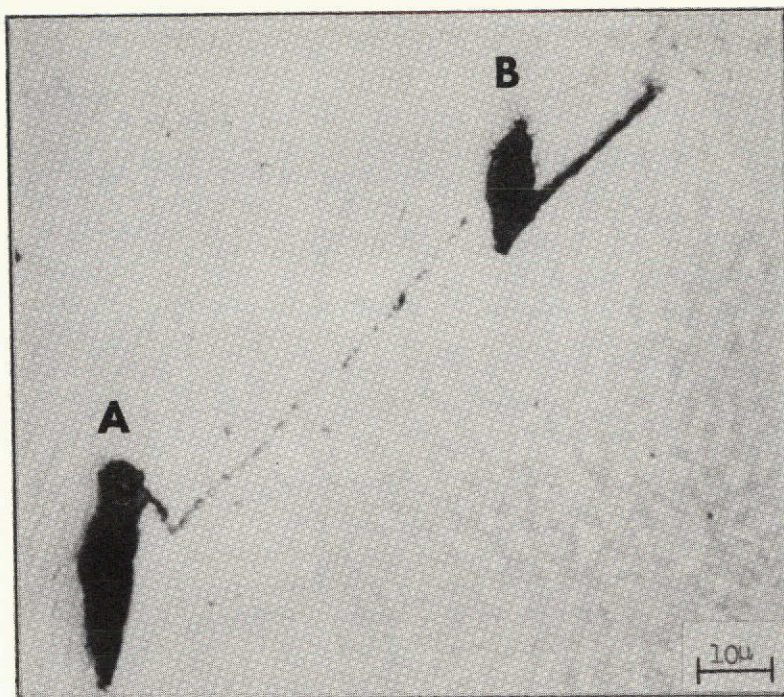
a) ε = 0.25 (Letters mark voids seen in
Figures 65-68)

Tensile Axis
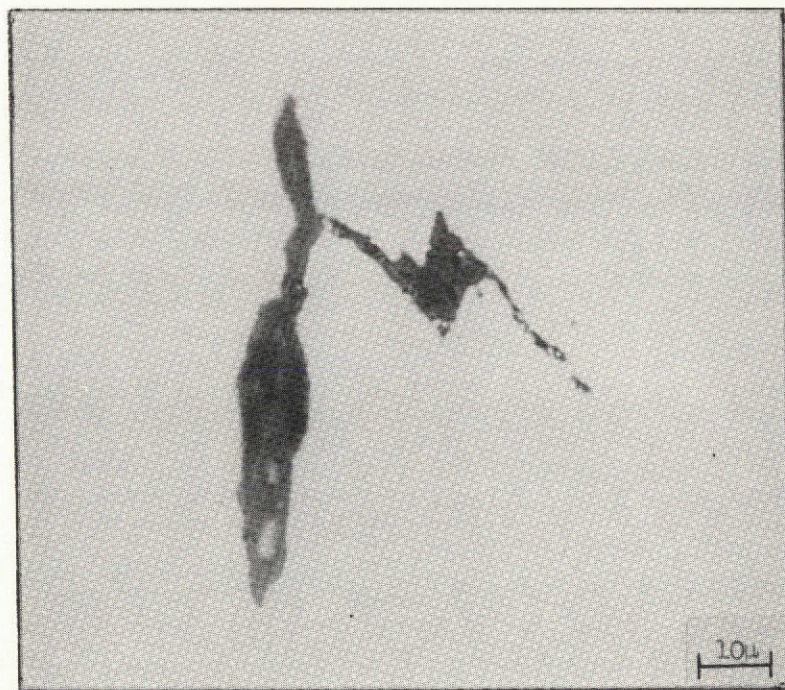


b) ε = 0.27

Figure 65    Coalescence of Voids by Void Sheet Formation in
Smooth Specimens of AISI 4340 Steel Strained
Plastically

in Figures 66-68. It is readily seen that the connecting feature is planar and maintains an orientation of approximately 45° with the tensile axis. The large, sulfide-nucleated voids are lettered to aid in correlating the figures.

The connecting feature is discontinuous between "A" and "B" in Figure 65a, but after polishing approximately 10 microns below the plane in Figure 65a, the sheet becomes nearly continuous between "A" and "B", as shown in Figure 66. Polishing down another 40 microns shows that the feature is planar and has become more continuous as illustrated in Figure 67. Note also in Figure 67 the emergence of void "D" along the 45° line between "B" and "C". After removing approximately another 40 microns, voids "B", "C", and "D" have all either disappeared or become quite small and the connecting sheet has once again become a planar collection of discontinuous voids, as shown in Figure 68. A schematic drawing of the progression of the coalescence of inclusion-nucleated voids in the AISI 4340 alloys is presented in Figure 69. As the strain increases, cementite-nucleated voids appear between the two inclusion-nucleated voids (Figure 69b) creating a planar sheet of voids. Once these secondary voids form, growth of the inclusion-nucleated voids is restricted due to the concentration of deformation in the regions between the voids. As the strain is increased the carbide-nucleated voids begin to coalesce (Figure 69c) and eventually form a continuous crack between the large voids (Figure 69d). As the fracture strain is approached the crack opens up and a large cavity results

Tensile
Axis
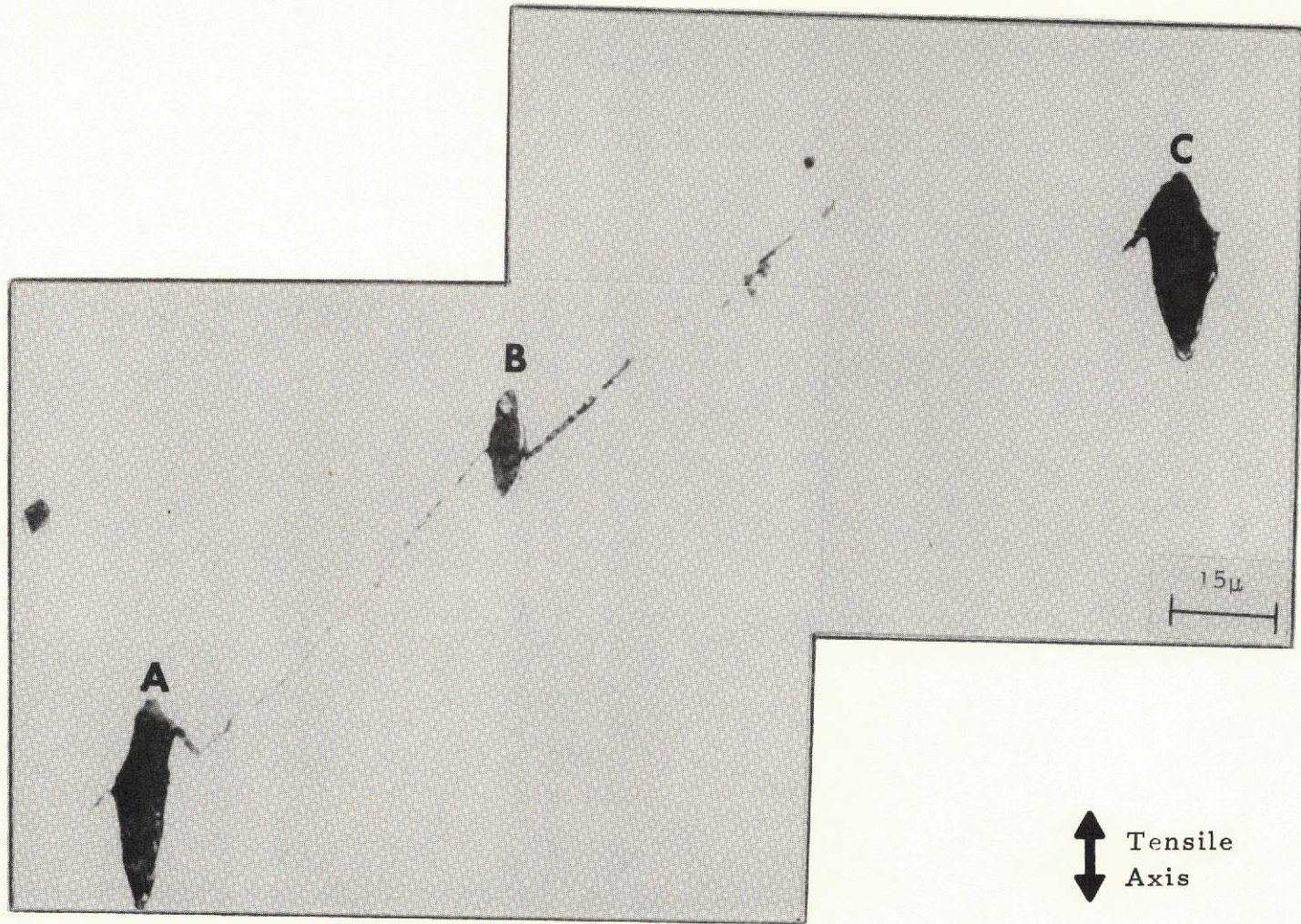
Figure 66   Void Sheet Approximately 10 Microns Below Midplane
(Letters mark voids seen in Figures 65-68).

15μ

Tensile
Axis
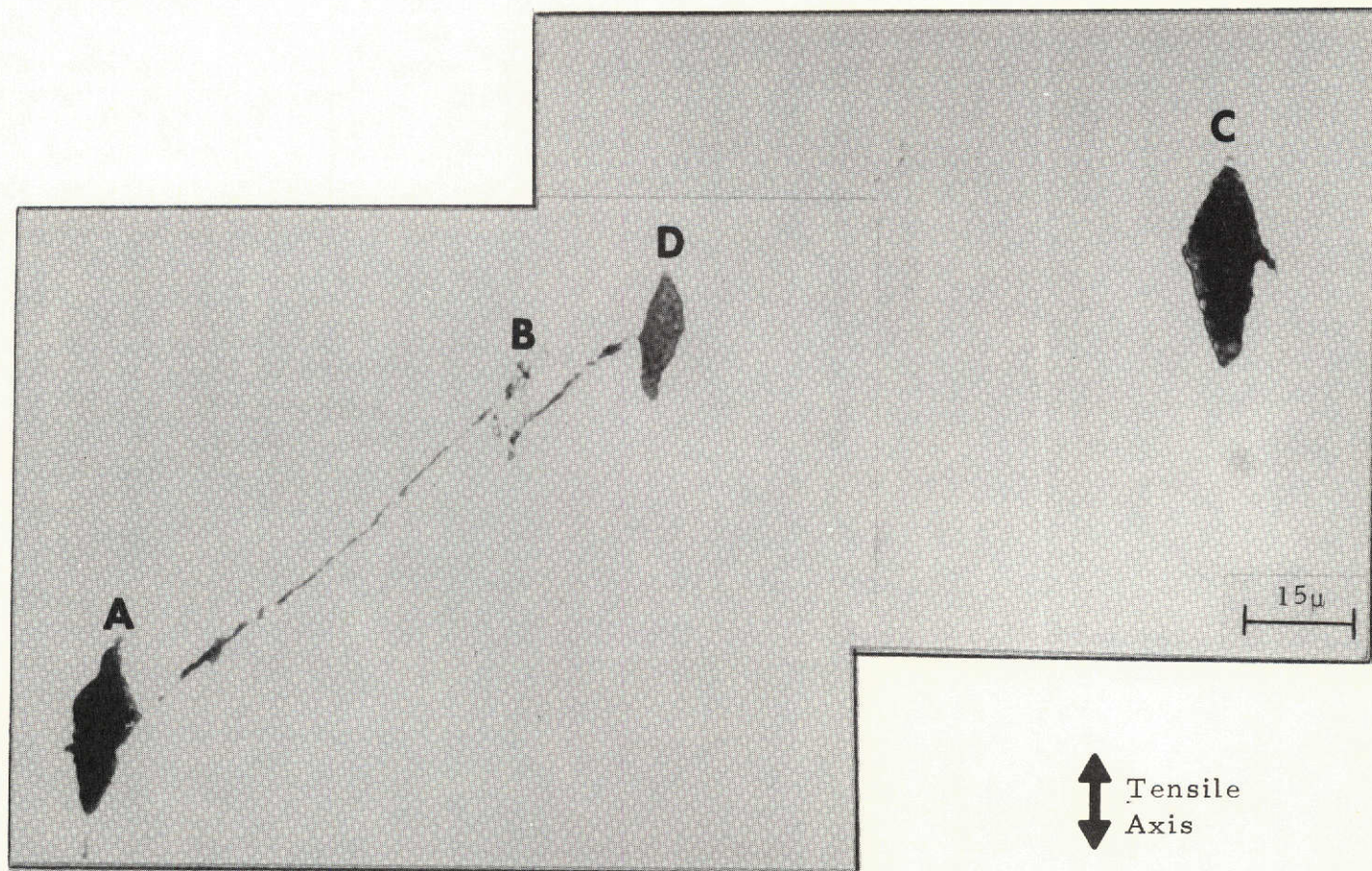
Figure 67  Void Sheet Approximately 50 Microns Below Midplane
(Letters mark voids seen in Figures 65-68).
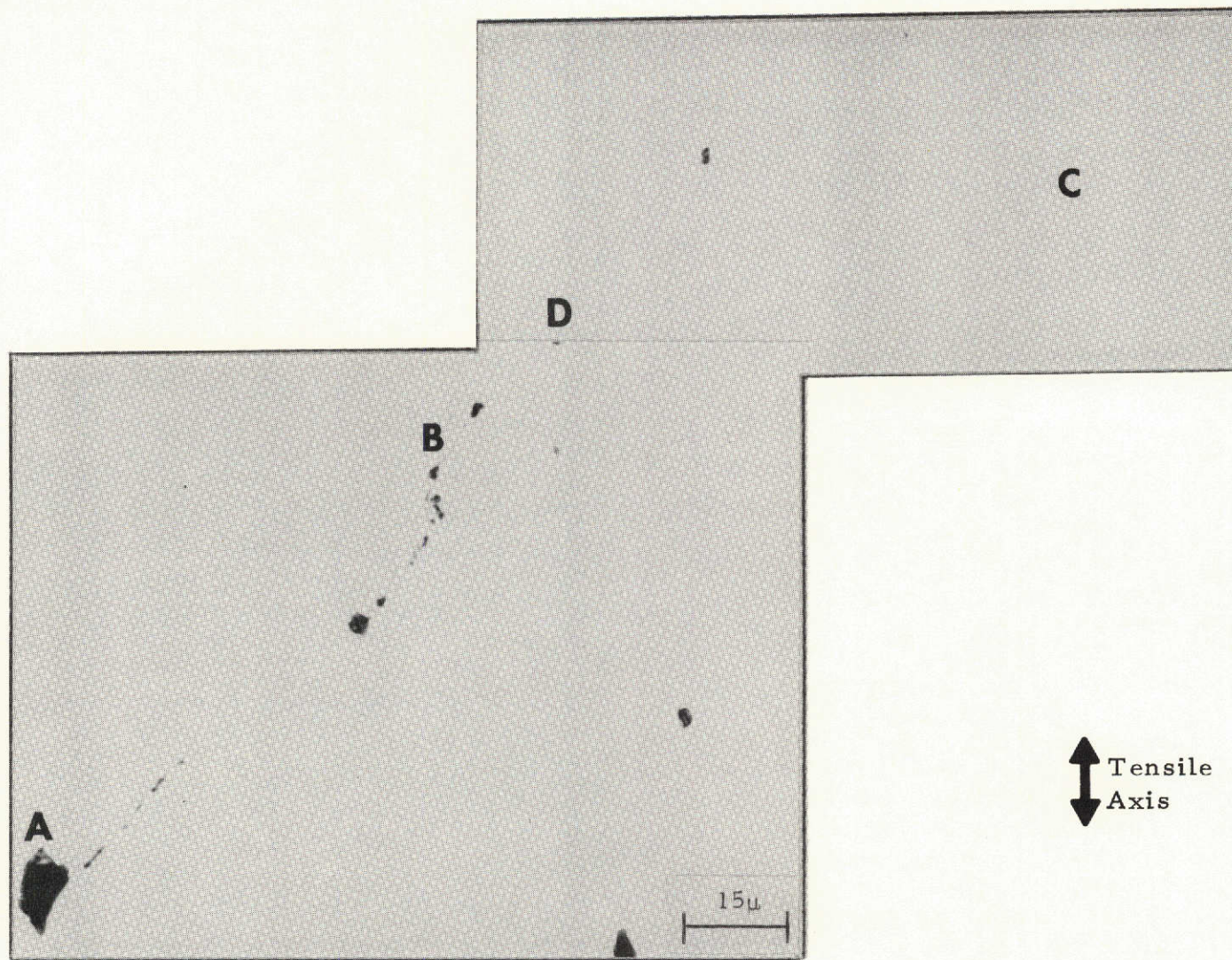
Figure 68   Void Sheet Approximately 90 Microns Below Midplane
(Letters mark voids seen in Figures 65-68).

a)

b)

c)

**Increasing strain**

d)

**Tensile axis**

**Thru thickness direction**

**Rolling direction**

e)
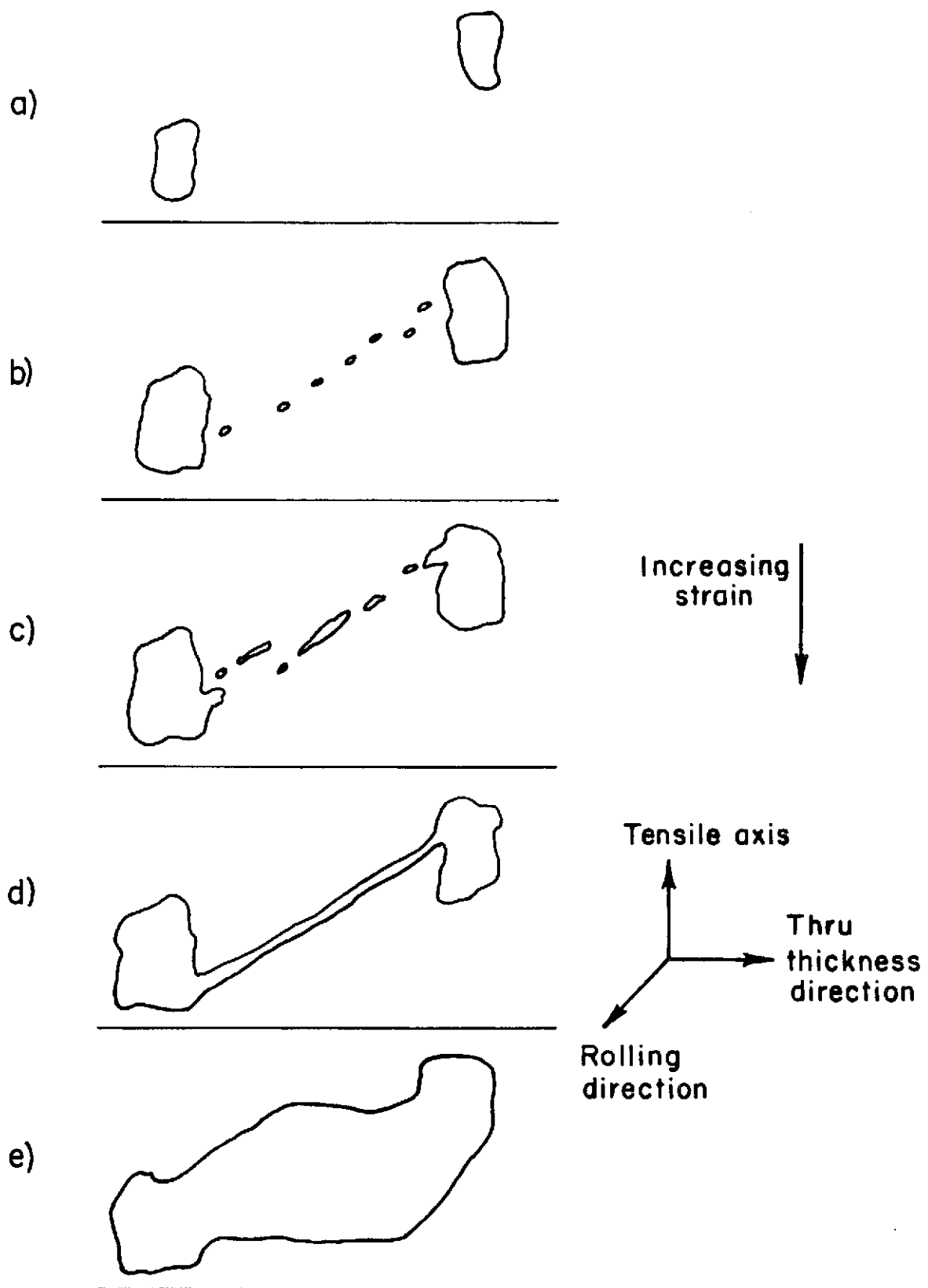
Figure 69  Schematic Drawing of Void Coalescence in
AISI 4340 Steel.

(Figure 69e)...

It is interesting to note that the void sheets tend to form along directions of the maximum resolved shear stress and that they tend to traverse the specimen neck in a zig-zag fashion to remain roughly in the region of the minimum cross-sectional area, i.e., the region of maximum stress. This fact may be seen at "C" in Figures 66 and 67 where the sheet changes orientation as it passes through the void. This same observation was made by Rogers in copper. The tendency of the macroscopic crack to remain in the region of maximum stress by a zig zag propagation is also hinted at in Figure 62 for the maraging steels. This behavior probably best explains the periodic linear features perpendicular to the direction of crack propagation observed by Yoder[147] on fracture surfaces of various high strength steels.

Before a distinct void sheet forms between two neighboring sulfide-nucleated voids, the region of matrix between the existing large voids shows signs of concentrated severe deformation. Figure 70 presents an electron transmission micrograph of a replica taken from the midplane of a strained and sectioned smooth tensile specimen of commercial purity AISI 4340 lightly etched. Note the "disturbed" appearance of the matrix between the two large voids (marked by "X") as compared with the matrix removed from the voids. There is evidence of both large, pronounced linear features of intense deformation exhibiting the same appearance, as reported by Clausing,[156] (indicated by "S") and small secondary void
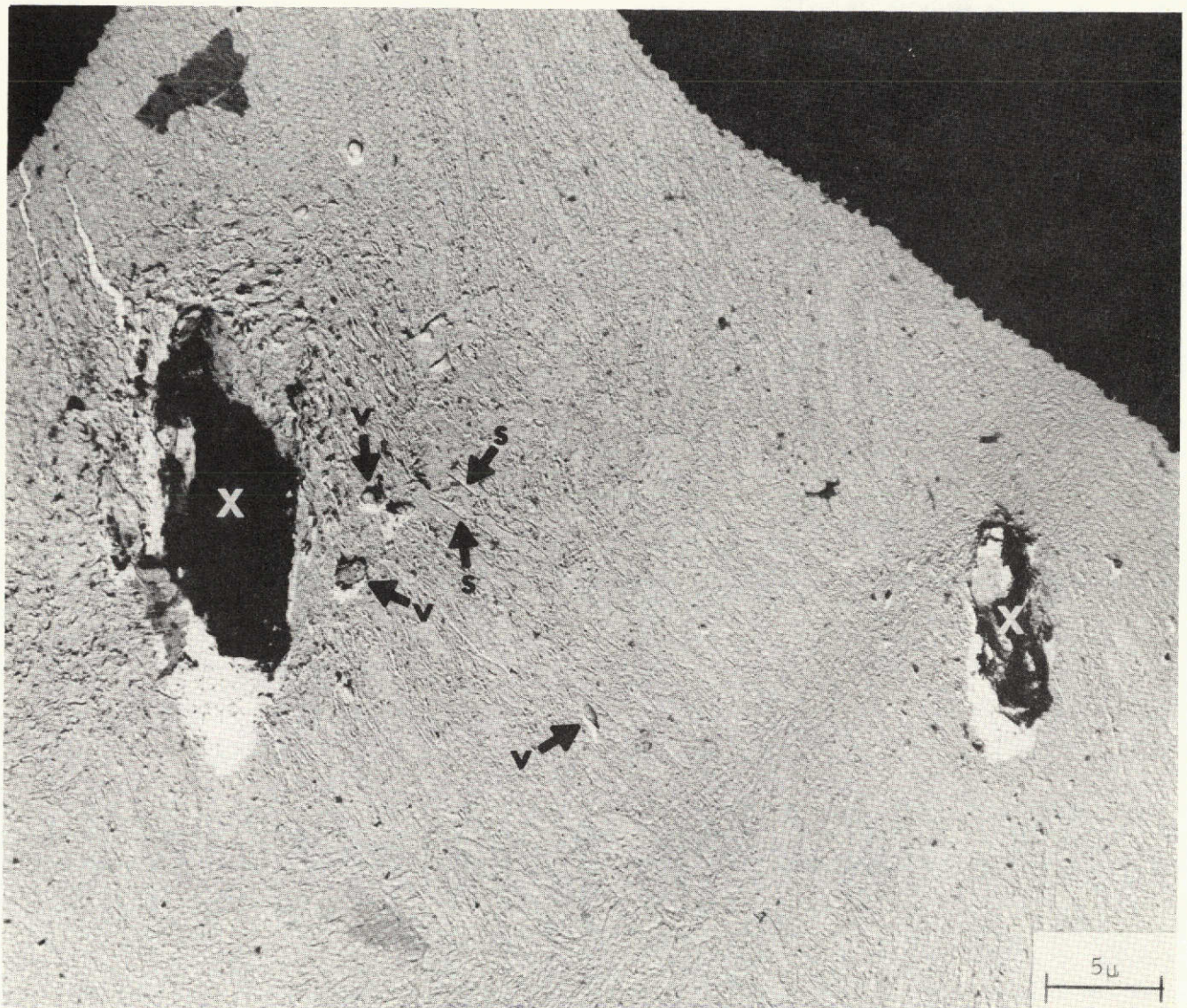
Tensile Axis

Figure 70  Concentration of Deformation Between Large Voids
in AISI 4340 ("S" indicates deformation markings and
"V" indicates small voids, large voids marked with
"X").

This page is reproduced at the
back of the report by a different
reproduction method to provide
better detail.

formation (indicated by "V") in the region between the large voids while the matrix removed from the large voids has a less deformed appearance. All of these observations were formulated using stereo pairs of the polished and etched structures.

These observations lead to the conclusion that the voids nucleated by the manganese sulfides grow to some critical size or until a critical spacing between them is reached. At this point, further deformation seems to be concentrated in the narrow bands between the neighboring large voids and the growth of the large voids is restricted. As straining continues, the bands of intense deformation between the voids become more distinct and the small voids formed at the carbide particles in these bands, begin to coalesce resulting in the formation of a void sheet and subsequent crack connecting neighboring large voids. This progression was illustrated in Figure 69.

A clear example of the early stages of void sheet formation is illustrated in Figure 71. The etch has delineated the narrow band of intense shear running out of the large void at an angle of approximately 45° with the tensile axis. Examples of small voids formed within the deformation bands are indicated by the arrows. (These features were designated as voids by using stereo pairs of the polished and etched section). Based on the previous investigation of the AISI 4340 fracture surfaces, it would be expected that these small voids within the void sheets are nucleated on the carbide particles. An example of the small voids in a deformation band,

Tensile
Axis

2μ
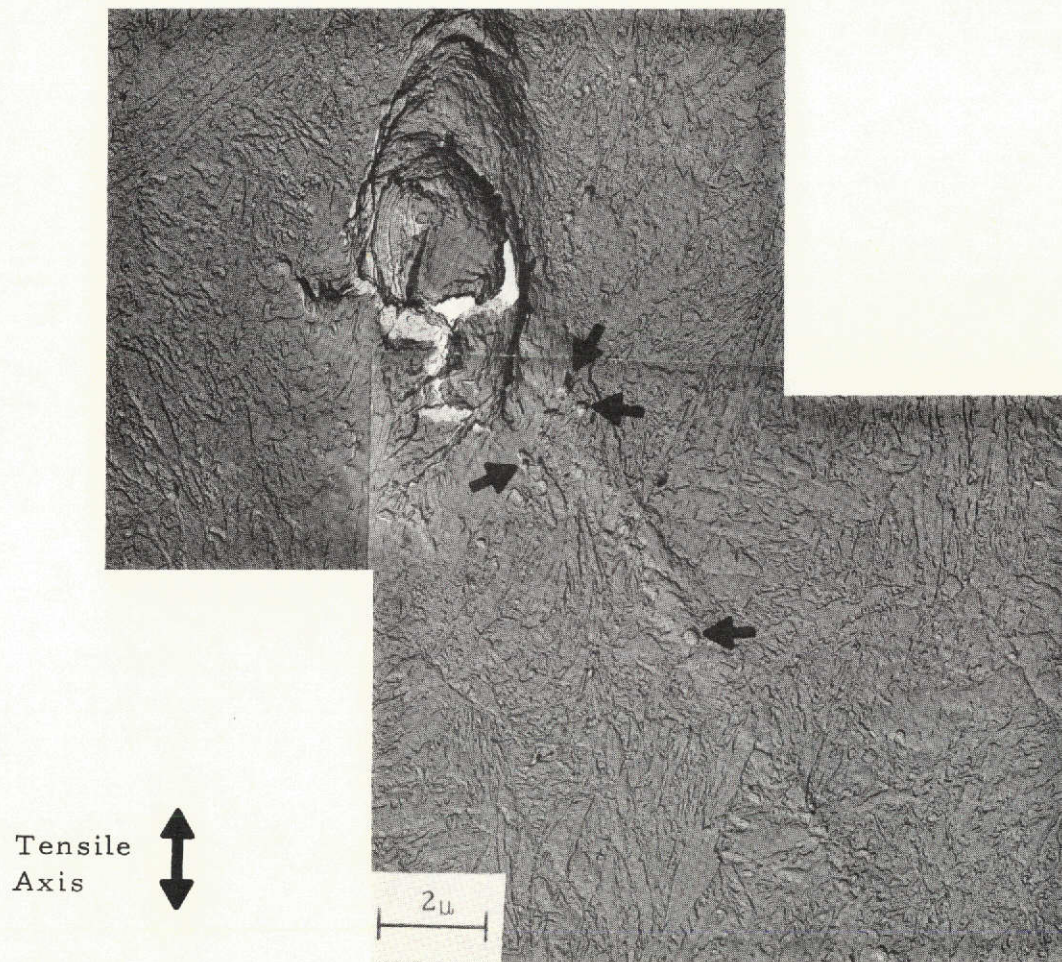
Figure 71   Early Stages of Void Sheet Formation in AISI 4340
Steel (Arrows indicate small voids).

preferentially developing along a martensitic lath boundary where the carbide particles precipitate, is presented in Figure 72 with the voids indicated by the arrows and the lath boundary outlined by the dashed line.

If the strains at which the void sheets are first seen optically in the AISI 4340 alloys are used as the limiting strain in conjunction with the rates of void growth presented in Table VII, the predicted sizes of the sulfide-nucleated dimples on the fracture surfaces are much larger than those observed in practice. Thus, the concentration of strain into the bands betwen the large voids must begin much earlier than the first optical observation of the void sheet. It would also seem reasonable that the nucleation of the small voids on the carbides would begin earlier than predicted from the optical observations. In order to determine the exact conditions for the start of the concentration of deformation between large voids and the initiation of voids at the carbide particles, would require an extensive study using electron transmission microscopy of thin sections of strained specimens. It has been demonstrated by Broeck[30] in aluminum alloys, that a study of this nature for investigating the fracture process is not feasible. Thus, it does not seem possible at this time to determine the exact sequence of events leading to void sheet formation. Does small void formation occur as a result of concentrated shear or is the deformation concentrated because of the presence of the small voids in the vicinity of the inclusion-nucleated voids?

Figure 72  Voids Nucleated at Martensite Boundaries in Region
of Severe Deformation Between Large Voids in AISI
4340 Steel (Arrows indicate voids and dashed lines
indicates martensite lath boundary).

If it is assumed that the concentration of strain between the large voids and the nucleation of small voids at the carbide precipitates could be avoided without affecting the rates of growth of the inclusion-nucleated voids, as determined in Chapter VIII, it is possible to ascertain whether or not improvement in the strains to fracture could be realized. Using half the average inter-inclusion spacing as the approximate radius of the large voids at fracture if void sheet formation were avoided and the growth rates in Table VII, the predicted fracture strains for the commercial purity AISI 4340 are approximately those observed in practice, but the fracture strains predicted for the high-purity alloy are considerably higher than those observed. For example, the observed fracture strain for smooth specimens of the high-purity alloy was 0.52 and the predicted fracture strain assuming no void sheet formation is 0.90.

Although this treatment is highly problematic since changing the carbide distribution to avoid the nucleation of small voids will undoubtedly change the flow characteristics of the matrix, it does indicate that improvement in the resistance to plastic fracture can follow from restricting the formation of the void sheets which result in the premature coalescence of the inclusion-nucleated voids.

C.  Summary and Discussion of Void Coalescence

It has been seen in the two previous chapters that qualitatively the processes of void initiation and growth in these two alloy families are quite similar. Yet, as demonstrated, the fracture toughness values vary quite

widely in these alloys with the maraging steels being substantially tougher than the AISI 4340 alloys. A plausible explanation for this difference lies in the fundamental differences observed in the void coalescence processes of these two alloy systems.

The growth of voids nucleated by the non-metallic inclusions in the AISI 4340 alloys is interrupted, before impingement, by the formation of cracks which connect the voids. These cracks have been shown to follow directly from sheets of fine voids nucleated by the cementite precipitates which have coalesced by impingement in narrow bands at 45° degrees to the tensile axis. In contrast, the strengthening particles in the maraging steels do not initiate a population of voids so that inclusion-nucleated voids grow until impingement. Thus, fracture in the maraging steels occurs at higher strains than in the AISI 4340 alloys.

The particles of intermetallic compound which strengthen the maraging steels are one to two orders of magnitude smaller than the carbides in the quenched and tempered steels. Roesch and Henry[37] have demonstrated that these strengthening precipitates do nucleate voids when they are coarsened with a concurrent drop in toughness. These observations suggest that it may be possible to alter the carbide dispersion in the quenched and tempered steels in order to prevent or delay nucleation of voids at the cementite particles. As a first attempt, it would be advantageous to reduce the size of the carbides and perhaps produce a more homogeneous dispersion since the carbides tend to precipitate at the martensite

lath boundaries. There is evidence that this approach may work in the fact that both strength and toughness can be improved in certain steels by various thermomechanical treatments which result in redistribution of the carbides off the lath boundaries and refinement in the size of the carbides.[148] Kula and Dhosi[149] demonstrated that the Charpy impact shelf energy of AISI 4340 steel was raised by working the steel in the austenite region and quenching directly to martensite followed by tempering. Although no transmission electron microscopy was performed, they speculated that the increased toughness was due to restricted boundary precipitation of cementite since the deformation and subsequent quench provided many nucleation sites for carbide precipitation during tempering resulting in a finer and more general precipitate dispersion. Recent work by Speich, Dabkowski, and Porter[150] indicates that very high levels of toughness can be realized in high-purity quenched and tempered steels containing substantial amounts of cobalt. The cobalt retards the recovery of the dislocation structure in the martensite providing more nucleation sites for carbide precipitation. It is observed that the coarse cementite precipitate generally found at the martensite boundaries is replaced by fine alloy carbides which precipitate on the dislocations resulting in substantial improvements in toughness.

# CHAPTER X

## SUMMARY OF RESULTS

The plastic fracture process in AISI 4340 and 18 Ni, 200 grade maraging steels has been extensively studied using smooth, round and mildly notched tensile specimens and compact tension fracture toughness specimens. Both commercially produced and low residual, high-purity melts of each alloy were investigated. The fracture toughness values of both the AISI 4340 and 18 Ni maraging steels at the 200 ksi yield strength level are substantially improved by reducing the levels of impurity elements in the alloys.

Extensive fractographic analysis was performed using tensile fracture surfaces and fracture surfaces from fracture toughness specimens. At the 200 ksi strength level, all fractures from the low constraint situation found in smooth, round tensile specimens to the highly constrained plane strain fracture toughness specimens were observed to be entirely by the plastic fracture process (dimpled rupture). It was demonstrated that the number and size of dimples on the fracture surface of any one alloy were essentially the same for all degrees of restraint encountered in the three specimen geometries and the dimples could be correlated with various second-phase particles in the structure.

181

Using strained and sectioned tensile specimens, the microstructural aspects of the fracture processes in these alloys were investigated. The fracture of the 18 Ni, 200 grade maraging steel occurs by void nucleation by fracture of the titanium carbo-nitride inclusions and subsequent growth of these voids until they coalesce by impingement. The plastic fracture process in the AISI 4340 steel differs substantially from this behavior and involves the nucleation and growth of two sets of voids, one associated with the manganese sulfide inclusions and one with the carbide dispersion produced during tempering. Large voids are nucleated by decohesion along the boundaries between the sulfides and the matrix and grow to some critical size. The coalescence of the large inclusion-nucleated voids occurs by the formation of void sheets linking the large voids along planes oriented at approximately 45° to the tensile axis. The small voids composing the void sheets are formed by the decohesion of the boundary between the cementite precipitates and the matrix and the growth of these voids until impingement with one another. It is felt that the interruption of the growth of the inclusion-nucleated voids in the quenched and tempered AISI 4340 steels by the formation of void sheets is the primary reason that the quenched and tempered steels are generally less tough than the maraging steels.

It is shown that the improvements in toughness experienced in the high-purity alloys are due to a refinement in the sizes of the non-metallic inclusions. It is observed that void nucleation occurs at lower strains at the larger inclusions and that void growth takes place more rapidly from

the larger inclusions, thus reducing the resistance of the alloy to fracture.
By comparing the metallographic results from smooth and notched tensile
specimens, it is demonstrated that void initiation is independent of the
level of stress triaxiality, but that void growth rates are increased sub-
stantially by increasing the level of hydrostatic tension. Increased growth
rates result in more rapid coalescence of voids and premature fracture,
explaining the mechanism by which notches and flaws in structural materials
lead to brittle fractures even when the microscopic fracture mode is
dimpled rupture (plastic fracture).

The investigation indicates that the most important microstructural
features governing the plastic fracture of these alloys are the void nucleating,
second phase particles. The toughness of these alloys may be most readily
improved by decreasing the number and size of non-metallic inclusions.
It is felt that this observation will hold generally for any of the high-strength
martensitic alloys which fail entirely by plastic fracture. Although re-
cently reported work by other investigators[152-154] indicates that at high-
strength levels (250-320 ksi) fracture toughness is insensitive to steel
cleanliness, the fracture mode exhibited at these high-strength levels in
severely notched $K_{Ic}$ specimens is mixed, consisting of plastic fracture and
cleavage[152] and thus the results reported herein are not applicable.

The concluded reason for the difference in toughness levels between
maraging steels and quenched and tempered steels is believed to be general
concerning all quenched and tempered steels which exhibit fairly coarse
carbide precipitates capable of nucleating voids during plastic deformation.

To improve the toughness of the quenched and tempered steels vis-a-vis the maraging alloys would require refinement of the carbides and most probably a redistribution off the martensite boundaries to give a more uniform dispersion.

The reported details of the mechanisms of plastic fracture in these alloys as determined by the examination of sectioned smooth and notched round tensile specimens are believed to be general and should apply in all cases where fracture occurs by dimpled rupture and the stress state is tensile in nature. This belief is supported by the fact that no qualitative differences in the fracture processes were observed between the smooth and notched specimens, i.e., as a result of increasing the level of tri-axiality of the tensile stress state. Furthermore, the fracture surfaces of the tensile specimens and the plane strain fracture toughness specimens were equivalent for any particular alloy. Thus the conclusions drawn from the current study should be directly applicable to the processes which occur at a crack tip as in a plane strain fracture toughness specimen or at a flaw in a material in service. The mechanisms which have been de-scribed herein should be the same as those which occur at crack tips and lead to instability and total fracture, provided the failure occurs entirely by plastic fracture.

CHAPTER XI

SUGGESTIONS FOR FUTURE WORK

This investigation and many others indicate that the resistance of

the high-strength steels to plastic fracture is very dependent upon the non-

metallic inclusions present in the alloys. Thus far, the approach practically

taken to improve the fracture toughness of these steels has been to use

special melting practices to reduce the levels of impurity elements. The

practices employed to produce the higher purity levels are generally quite

expensive and add substantially to the cost of the final product. The cur-

rent investigation suggests that inclusion size is an important factor in the

fracture process and that if the average size of inclusion were reduced at

any given level of cleanliness, improvements in toughness could be realized.

As shown for the manganese sulfide particles, inclusions many times nu-

cleate on deoxidation products present in the melt. This observation sug-

gests that it might be possible to suitably seed or otherwise increase the

frequency of nucleation of inclusions for a given impurity level of a melt

in order to produce a finer dispersion of non-metallic inclusions in the

final product. Thus, it might be possible to live with higher impurity levels

provided the sizes of inclusions were reduced. It is felt that an investi-

gation of the fracture behavior of several alloys of a given impurity level

185

but with different inclusion sizes together with studies designed to determine methods of controlling the sizes of inclusions would be of great significance.

As the quenched and tempered steels are generally of lower alloy content than the maraging steels and hence more economically produced, it would be beneficial to investigate means of improving their toughness in relation to the maraging steels. As pointed out in the current investigation, the major difference in the fracture behavior of these two families is the observed void sheet process of coalescence of the largest inclusion-nucleated voids in the AISI 4340 alloys. The voids of these sheets are nucleated by the coarse ($\sim$ 2000 $\overset{o}{A}$) cementite particles which precipitate at the martensite boundaries. It is felt that by refining the size of the carbides and dispersing them more generally throughout the matrix, void initiation at the carbides could be delayed or avoided with a resultant improvement in toughness. Both thermomechanical treatments[148] and repetitive austenitizing treatments[155] have the ability to refine the carbide distribution conceivably by providing more sites for carbide nucleation during tempering. In addition, the recent work of Speich, et al.[150] has demonstrated that the addition of cobalt to a quenched and tempered steel containing 10 percent nickel results in a very fine carbide dispersion due to retarded recovery of the transformation dislocation structure and high levels of fracture toughness.

Unfortunately, most reported investigations concerning thermomechanical treatments have not included any fractographic observations

and very little metallographic information so that it is not known exactly

how the refined carbides affect the fracture process. In order to establish

whether or not refinement of the carbides leads to delay in the formation

of void sheets or even in the absence of void sheets and consequently im-

proved toughness, it would be useful to undertake a metallographic and

fractographic investigation of AISI 4340 either thermomechanically or

thermally treated to produce a refined carbide dispersion. One possible

means of refining the carbides would be by ausforming the steel in the

temperature range of 400 to 550°C as done by Kula and Dhosi.[149] After

a subsequent quench and temper, these authors observed improved tough-

ness, although they did not demonstrate the mechanism by which the im-

provement was realized.

Another possible thermomechanical treatment which as-quenched

AISI 4340 steel could be given to refine the carbides would be to mechanically

work the material during tempering (dynamically strain age). The reported

studies of this technique [157, 158] unfortunately have used deformation at

temperatures between 150° and 300°C with resulting decreases in fracture

toughness, undoubtedly due to the formation of epsilon carbide. Use of

higher deformation temperatures in the range normally used for tempering

conceiveably could result in a finer dispersion of cementite in the AISI 4340

steel due to increased dislocation densities as reported by Speich, et al.[150].

It might be possible to refine the carbide distribution by a suitable

thermal treatment without deformation. The work of Baker, et. al.[83] in-

dicates that as the tempering temperature of AISI 4340 is increased above

600°F the cementite dispersion precipitated in the structure becomes more and more general in nature. This observation suggests that it may be possible to produce a fine dispersion of carbide by giving AISI 4340 steel a duplex tempering treatment beginning with a short time at a high temperature (around 1000°F) to produce a large number of well dispersed carbide nuclei, followed by dropping the temperature directly to a more frequently used tempering temperature to achieve reasonable strength (around 800°F). The effects of a thermal treatment of this sort would have to be demonstrated, but, if it could accomplish carbide refinement and improved toughness, seemingly it would be more attractive than thermomechanical processing from a practical point of view.

A detailed study of the effects of the above treatments on the structure and fracture behavior of AISI 4340 steel would undoubtedly demonstrate whether or not it is feasible to improve the level of toughness of the quenched and tempered steels without changing composition or melting practice.

REFERENCES

1. R. F. Mehl, A Brief History of the Science of Metals, AIME, New York, 1 (1948).

2. E. R. Parker, Brittle Behavior of Engineering Structures, John Wiley & Sons, London, 7 (1957).

3. M. E. Shank, Weld. Res. Council Bull. No. 17, (1954).

4. D. B. Armstrong, Highway Research Abstract, 21, 24 (1951).

5. F. L. Plummer, Weld. Jnl., 1081 (Nov. 1946).

6. W. A. Saylor, Iron Age, 167, 97 (1951).

7. J. Plateau, G. Henry, and C. Crusard, Revue Me'tall, 54, 200, (1957).

8. J. R. Low, Jr., Prog. Mat. Sci., 12 (1), 4 (1963).

9. J. R. Low, Jr., Engr. Frac. Mech., 1, 47 (1968).

10. J. R. Low, Jr., "A Review of the Microstructural Aspects of Cleavage Fracture," in Fracture, eds. B. L. Averback, D. K. Felbeck, G. T. Hahn, and D. A. Thomas, Technology Press, MIT and John Wiley & Sons, New York, 68 (1959).

11. C. P. Sullivan, Weld. Res. Council. Bull. No. 122 (1967).

12. H. C. Roger, Trans. AIME, 218, 498 (1960).

13. F. D. Rosi and M. S. Abrahams, Acta Met., 8, 807 (1960).

14. C. J. Beevers and R. W. K. Honeycombe, "Ductile Fracture of Single Crystals," in Fracture, eds. B. L. Averback, D. K. Feldbeck, G. T. Hahn, and D. A. Thomas, Technology Press, MIT and John Wiley & Sons, New York, 474 (1959).

15. I. G. Palmer, G. C. Smith, and R. D. Warda, Inst. Phys. and Phys. Soc. Conf. Ser., No. 1, 53 (1966).

16. C. F. Tipper, Metallurgica, 39, 133 (1948).

17. K. E. Puttick, Phil. Mag., 4, 964 (1959).

18. B. I. Edelson and W. M. Baldwin, Jr., Trans. ASM, 55, 230 (1962).

19. D. P. Clausing, Trans. ASM, 60, 504 (1967).

20. J. C. Danko and R. D. Stont, Weld. Jnl. Res. Suppl., 35, 77s (1956).

21. K. W. Burns and F. B. Pickering, JISI, 202, 899 (1964).

22. J. C. Danko, J. H. Gross, and R. D. Stont, Weld. Jnl. Res. Suppl., 35, 604s (1956).

23. J. A. Rinebolt and W. J. Harris, Jr., Trans. ASM, 44, 225 (1952).

24. A. G. Franklin and W. J. McG. Tegart, JISI, 202, 588 (1964).

25. C. T. Liu and J. Gurland, Trans. ASM, 61, 156 (1968).

26. C. J. McMahon and M. Cohen, Acta Met., 13, 591 (1965).

27. R. J. Olsen and G. S. Ansell, Trans. ASM, 62, 711 (1969).

28. E. Ruedl, Jnl. Mat. Sci., 4, 814 (1969).

29. J. P. Tanaka, C. A. Pampillo, and J. R. Low, Jr., ASTM STP 463, 191 (1970).

30. D. Broek, "A Study on Ductile Fracture," Ph.D. Thesis, Delft Technological University (1970).

31. M. A. Greenfield and H. Margolin, Met. Trans., 3, 2649 (1972).

32. J. H. Bucher, G. W. Powell, and J. W. Spretnak, Trans. AIME, 233, 884 (1965).

33. A. J. Birkle, R. P. Wei, and G. E. Pellissier, Trans. ASM, 59, 981 (1966).

34. B. J. Brendley, Acta Met., 16, 587 (1968).

35. P. S. Trozzo and G. E. Pellissier, AIME Met. Soc. Conf., 31, 323 (1966).

36. A. J. Birkle, D. S. Dabkouski, J. P. Paulina, and L. F. Porter, Trans. ASM, 58, 285 (1965).

37. L. Roesch and G. Henry, ASTM STP 453, 3 (1969).

38. J. N. Goodier, Jnl. Appl. Mech., Trans. ASME, 55, 39 (1933).

39. R. H. Edwards, Jnl. Appl. Mech., 18, 19 (1951).

40. E. Sternberg, Appl. Mech. Rev., 11, 1 (1958).

41. J. Gurland and J. Plateau, Trans. ASM, 56, 442 (1963).

42. C. Nishimatsu and J. Gurland, Trans. ASM, 52, 469 (1960).

43. J. Gurland, Trans. AIME, 227, 1146 (1963).

44. W. A. Backofen, "Metallurgical Aspects of Ductile Fracture," in Fracture of Engineering Materials, ASM, Metals Park, 107 (1964).

45. M. F. Ashby, AIME Met. Soc. Conf., 47, 143 (1968).

46. M. F. Ashby, Phil. Mag., 14, 1157 (1966).

47. A. N. Stroh, Proc. Roy. Soc., A223, 404 (1954).

48. A. N. Stroh, Proc. Roy. Soc., A232, 548 (1955).

49. A. N. Stroh, Adv. in Phys., 6, 418 (1957).

50. S. Floreen and H. W. Hayden, Scripta Met., 4, 87 (1970).

51. B. Y. Pines, Zh. Eksperim. i Theor. Fiz., 16, 744 (1946).

52. A. H. Cottrell, "Theoretical Aspects of Fracture." in Fracture eds. B. L. Averback, D. K. Feldbeck, G. T. Hahn, and D. A. Thomas, Technology Press, MIT and John Wiley & Sons, New York, 20 (1959).

53. P. F. Thomason, Jnl. Inst. Met., 96, 360 (1968).

54. D. McLean, Mechanical Properties of Metals, John Wiley & Sons, New York, 224 (1962).

55. P. Feltham and A. S. Beyron, Phil. Mag., 13, 311 (1966).

56. F. A. McClintock, S. M. Kaplan, and C. A. Berg, Int. Jnl. Frac. Mech., 2, 614 (1966).

57. F. A. McClintock, "On the Mechanics of Fracture from Inclusions," in Ductility, ASM, Metals Park, 255 (1968).

58. F. A. McClintock, Jnl. Appl. Mech., 35, 363 (1968).

59. J. R. Rice and D. M. Tracey, Jnl. Mech. Phys. Solids, 17, 201 (1969).

60. A. R. Rosenfield, Met. Rev., 13, 29 (1968).

61. J. I. Bluhm and R J. Morrissey, Proc. 1st Inter. Conf. on Frac., Vol. III, 1739 (1966).

62. M. J. Druyresteyn, F. T. Klostermann, J. Roos, P. M. van Dijk, P. Los, and S. Radelaav, Jnl. Mech. Phys. Solids, 12, 219 (1964).

63. A. R. Rosenfield and G. T. Hahn, Trans. ASM, 59, 962 (1966).

64. C. Crussard, R. Borione, J. Plateau, Y. Morillon, and F. Maratray, JISI, 183, 146 (1956).

65. J. Plateau, G. Henry, and C. Crussard, Rev. Univ. Mines., 12, 543 (1956).

66. J. Plateau, G. Henry, and C. Crussard, Rev. Met., 54, 200 (1957).

67. C. Crussard, J. Plateau, R. Tamhankar, G. Henry, and D. Lajeunesse, "A Comparison of Ductile and Fatigue Fractures," in Fracture, eds. B. L. Averback, D. K. Feldbeck, G. T. Hahn, and D. A. Thomas, Technology Press, MIT, and John Wiley & Sons, New York, 524 (1959).

68. C. D. Beachem, Trans. ASM, 56, 318 (1963).

69. S. Floreen, Trans. ASM, 57, 38 (1964).

70. S. Floreen, Met. Rev., 13, 115 (1968).

71. S. J. Matas, M. Hill, and H. P. Munger, Met. Engr. Quart., 3(3), 7 (1963).

72. D. W. Berland, Jnl. Austrl. Inst. Met., 14, 17 (1969).

73. G. Delisle and A. Galibois, JISI, 207, 1628 (1969).

74. A. J. Baker, P. M. Kelly, and J. Nutting, "Structures Resulting from Phase Transformations in Steels," in Electron Microscopy and Strength of Crystals, eds. G. Thomas and J. Washburn, Interscience, New York, 899 (1962)

75. G. E. Pellissier, Engr. Frac. Mech., 1, 55 (1968).

76. R. F. Decker, C. J. Novak, and T. W. Landig, Jnl. Met., 19, 60 (1967).

77. S. Floreen and G. R. Speich, Trans. ASM, 57, 714 (1964).

78. D. T. Peters and C. R. Cupp, Trans. AIME, 236, 1420 (1966).

79. D. T. Peters, Trans. AIME, 239, 1981 (1967).

80. M. J. Fleetwood, G. M. Higginsen, and G. P. Miller, Brit. Jnl. Appl. Phys., 16, 645 (1965).

81. T. Boniszewski and E. Boniszewski, JISI, 204, 360 (1966).

82. B. G. Reisdorf, Trans. ASM, 56, 783 (1963).

83. A. J. Baker, F. J. Lauta, and R. P. Wei, ASTM STP 370, 3 (1965).

84. W. S. Pellini, ASTM STP 158, 222 (1954).

85. P. W. Bridgman, Large Plastic Flow and Fracture, McGraw-Hill, New York, 38 (1952).

86. L. F. Coffin and H. C. Rogers, Trans. ASM, 60, 672 (1967).

87. E. R. Marshall and M. C. Shaw, Trans. ASM, 44, 705 (1952).

88. A. K. Mukherjee, G. T. Hahn, and A. R. Rosenfield, Air Force Report AFML-TR-66-266, (1966).

89. M. A. Greenfield and H. Margolin, Air Force Report AFML-TR-70-43, (1970).

90. C. W. Chin, Acta Met., 9, 68 (1961).

91. Annual Book of ASTM Standards, 30, 127 (1964).

92. D. M. Fisher and A. J. Repko, Jnl. Mat., 7, 167 (1972).

93. Annual Book of ASTM Standards, 919 (1971).

94. A. W. Dana, E. L. Aul, and G. Sachs, NACA Tech. Note 1830 (1949).

95. G. Sachs, J. D. Lubahn, and L. J. Ebert, Trans. ASM, 34, 517 (1945).

96. G. Sachs and J. D. Lubahn, Trans. ASM, 31, 125 (1943).

97. G. Sachs and J. D. Lubahn, Trans. ASME, 67, A241 (1945).

98. G. Sachs and J. D. Lubahn, and L. J. Ebert, Trans. ASM, 33, 340 (1944).

99. P. W. Bridgman, Large Plastic Flow and Fracture, McGraw-Hill, New York, 9 (1952).

100. E. R. Parker, H. E. Davis, and A. E. Flanigan, Proc. ASTM, 46, 1159 (1946).

101. F. A. McClintock and A. S. Argon, Mechanical Behavior of Materials, Addison-Wesley, Reading, Mass., 325 (1966).

102. J. D. Lubahn, "Notch Tensile Testing" in Fracturing of Metals, ASM, 90 (1948).

103. D. P. Clausing, Jnl. Mat., 4, 566 (1966).

104. J. M. Chilton and C. J. Barton, Trans. ASM, 60, 528 (1967).

105. R. Kiessling and N. Lange, Non-Metallic Inclusions in Steel, Part II, Iron and Steel Inst., London, 97 (1966).

106. R. T. DeHoff and F. N. Rhones, Trans. AIME, 221, 975 (1961).

107. R. T. DeHoff, "Measurement of Number and Average Size in Volume," in Quantitative Microscopy, eds. R. T. DeHoff and F. N. Rhines, McGraw-Hill, New York, 128 (1968).

108. F. C. Hull and W. J. Houk, Trans. AIME, 197, 565 (1953).

109. E. J. Meyers, Proc. First. Ins. Cong. Stereology, Vienna, 151 (1963).

110. P. Hertz, Math Ann., 67, 387 (1909).

111. E. E. Underwood, Quantitative Stereology, Addison-Wesley, Reading, Mass., 29 (1970).

112. J. E. Hilliard, "Measurement of Volume in Volume," in Quantitative Microscopy, eds. R. T. DeHoff and F. N. Rhines, McGraw-Hill, New York, 45 (1968).

113. I. Miller and J. E. Freund, Probability and Statistics for Engineers, Prentice-Hall, Englewood Cliffs, New Jersey, 165 (1965).

114. D. Broek, Eng. Frac. Mech., 1, 4 (1969).

115. D. Broek, Philips Bull. 79, 177/EM, 39 (1969).

116. E. Tekin and P. M. Kelly, AIME Met. Soc. Conf., 28, 173 (1965).

117. K. H. Jack, JISI, 169, 26 (1951).

118. W. C. Leslie, R. M. Fisher, and N. Sen, Acta Met., 7, 632 (1959).

119. A. M. Turkalo, _Trans. AIME,_ 218, 24 (1960).

120. E. E. Underwood, _Quantitative Stereology,_ Addison-Wesley, Reading, Mass., 140 (1970).

121. W. Weibull, "A Statistical Theory of the Strength of Materials," _I.V.A. Proc. No. 151_ (1939).

122. N. Davidenkov, E. Shevandin, and F. Whittmann, _Trans. ASME,_ 69, A63 (1947).

123. G. R. Irwin, "Fracture" in _Encyclopedia of Physics,_ Vol. VI, ed. S. Flugge, Springer-Verlag, Berlin, 551 (1958).

124. A. M. Freudenthal, "Statistical Approach to Brittle Fracture" in _Fracture,_ Vol. II, ed. H. Liebowitz, Academic Press, New York, 592 (1968).

125. D. Brooksbank and K. W. Andrews, _JISI,_ 210, 246 (1972).

126. S. K. Rhee, _Jnl. Am. Cer. Soc.,_ 53, 639 (1970).

127. D. T. Livey and P. Murray, _Jnl. Am. Cer. Soc.,_ 39, 363 (1956)

128. C. E. Aguirre, Private Communication, Carnegie-Mellon University (1973).

129. H. C. Chao, L. H. Van Vlack, F. Oberin, and L. Thomassen, _Trans. ASM,_ 57, 885 (1964).

130. L. E. Wood and L. H. Van Vlack, _Trans. ASM,_ 56, 770 (1963).

131. H. C. Chao, L. Thomassen, and L. H. Van Vlack, _Trans. ASM,_ 57, 386 (1964).

132. H. Unckel, _Jnl. Inst. Met.,_ 61, 171 (1937).

133. R. W. K. Honeycombe and W. Boas, _Aust. Jnl. Sci. Res.,_ 1, 70 (1948).

134. H. C. Chao and L. H. Van Vlack, _Trans. AIME,_ 233, 1227 (1965).

135. H. C. Chao and L. H. Van Vlack, <u>Mat. Res. Stan.</u>, <u>5</u>, 611 (1965).

136. C. Zener, <u>Elasticity and Anelasticity</u>, Univ. Chic. Press, Chicago, 133 (1948).

137. C. E. Inglis, <u>Trans. Inst. Nav. Arch.</u>, <u>55</u>, 219 (1913).

138. G. R. Speich and W. C. Leslie, <u>Met. Trans.</u>, <u>3</u>, 1043 (1972).

139. S. Floreen and H. W. Hayden, <u>Met. Sci. Jnl.</u>, <u>4</u>, 77 (1970).

140. J. T. Barnby, <u>Acta Met.</u>, <u>15</u>, 903 (1967).

141. W. H. Bruckner, <u>Weld. Jnl. Res. Suppl.</u>, <u>29</u>, 467s (1950).

142. N. P. Allen, W. P. Reis, B. E. Hopkins, and H. R. Tipler, <u>JISI</u>, <u>174</u>, 108 (1953)

143. I. L. Magford and D. Hull, <u>JISI</u>, <u>206</u>, 79 (1968).

144. W. W. Webb and W. D. Forgeng, <u>Acta Met.</u>, <u>6</u>, 462 (1958).

145. R. H. Merchant, "The Plastic Fracture," unpublished manuscript, Carnegie-Mellon University (1972).

146. E. E. Underwood, "Particle Size Distribution," in <u>Quantitative Microscopy</u>, ed. R. T. DeHoff and F. N. Rhines, McGraw-Hill, New York, 149 (1968).

147. G. R. Yoder, <u>Met. Trans.</u>, <u>3</u>, 1851 (1972).

148. M. J. May and D. J. Latham, "Thermomechanical Treatment of Steels" in <u>Toward Improved Ductility and Toughness</u>, Climax Molybdenum Development Company (Japan), 157 (1971).

149. E. B. Kula and J. M. Dhosi, <u>Trans. ASM</u>, <u>52</u>, 321 (1960).

150. G. R. Speich, D. S. Dabkowski and L. F. Porter, <u>Met. Trans</u>, <u>4</u>, 303 (1973).

151. H. Darlington, "Ductile Fracture Under Axisymmetric Stresses in Electrolytic Iron and Spheroidized Low-Carbon Steel, " Ph. D. Thesis, Lehigh University (1971).

152. J. J. Hauser and M. G. H. Wells, "Inclusions in High-Strength and Bearing Steels - Their Dependence on Processing Variables and their Effect on Engineering Properties, " Air Force Materials Laboratory Technical Report AFML-TR-69-339 (1970).

153. J. J. Hauser, M. G. H. Wells and I. Perlmutter, Jnl. Vac. Sci. Tech., 9, 1339 (1972).

154. L. F. Porter, Jnl. Vac. Sci. Tech., 9, 1340 (1972).

155. R. A. Grange, Trans. ASM, 59, 26 (1966).

156. D. P. Clausing, "Comparison of Plane Strain and Axisymmetric Flow and Fracture, " U. S. S. Report 35.066-001(2), (1972).

157. N. N. Breyer and N. H. Polakowski, Trans. ASM, 55, 667 (1962).

158. V. F. Zackey, W. W. Gerberich, R. Bush and E. R. Parker, "The Strength and Toughness of Dynamically Strain Aged Alloy Steels, " Proc. 1st Inter Conf. on Frac., Vol. II, 813 (1966).

159. C. S. Smith, Trans. AIME, 218, 58 (1960).